This is to certify that the

dissertation entitled

CVD DIAMOND PIEZORESISTIVE

MICROSENSORS

presented by

Izzat Ibrahim Taher

has been accepted towards fulfillment
of the requirements for

Ph.D. degree in Electrical Engineering

Major professor

Date 11/3/94

CVD DIAMOND PIEZORESISTIVE MICROSENSORS

By

Izzat Ibrahim Taher

A DISSERTATION

Submitted to
Michigan State University
in partial fulfillment of the requirements
for the degree of

DOCTOR OF PHILOSOPHY

Department of Electrical Engineering

1994

Dia

suited

piezore

posited

hot fila

in the

diamon

decreas

A n

mum fe

chip em

cantilev

150 μm

The

ABSTRACT

CVD DIAMOND PIEZORESISTIVE MICROSENSORS

By

Izzat Ibrahim Taher

Diamond piezoresistive pressure, acceleration, and strain sensors can be uniquely suited to chemically harsh, high radiation and high-temperature environments. The piezoresistive effect in both polycrystalline and homoepitaxial chemical vapor deposited (CVD) diamond films was studied. The diamond films were produced by hot filament CVD system. The piezoresistive gauge factors, measured at 300 °K are in the ranges of 200 - 550 and 6 - 25 for homoepitaxial and polycrystalline p-type diamond films, respectively. The gauge factor for polycrystalline films decreases with decreasing resistivity but increases with increasing temperature.

A multisensor microchip, with a number of diamond test structures and a minimum feature size of 5 μm, was designed and fabricated using a six mask process. The chip employs diamond both as an electronic and a mechanical material. An array of cantilever beams of various sizes ranging from 100 to 1500 μm in length, from 20 to 150 μm in width and 3 to 5 μm in thickness were fabricated.

The residual total stress of the diamond films was investigated as a function of

methane fraction in hydrogen with or without addition of carbon monoxide. It was observed that the magnitude of the total stress for films deposited in the absence of CO was very high in comparison with the samples deposited in the presence of CO. This result indicates that by using CO in the gas mixture, it is possible to control the type and magnitude of the total stress in the diamond films.

To

my parents, my wife, my brothers and sisters

and

to the memory of my grandparents and my father-in-law.

ACKNOWLEDGEMENTS

In The Name Of Allah

Most Gracious, Most Merciful.

All praises be to Allah (soobhanaho wa taalah), the creator and sustainer of this universe for providing me the strength and the patience to complete this work.

I owe my greatest thanks to my parents. They have always allowed me to make my own decisions. They have worked hard and sacrificed much so I can be where I am today. A very special thanks goes to my wife Saida Benromdhane, who helped keep me going especially when it seemed like this dissertation would never get finished. My deepest appreciation for her understanding and patience when I had to spend long nights in the lab. Also I am grateful for the support of my brothers Raafat, Ali, Mouhammad and Houssein, my sisters Jomana, Silvana and Amal, my brother-in-law and best friend Mahmoud Awada, my sister-in-law Souad Benromdhane and all of my other relatives. I would like also to thank all my high school, undergraduate and all friends back home in Lebanon for their encouragement.

I would like to express my deep gratitude to my advisor, Dr. Mohammad Aslam for his guidance and encouragement throughout my doctoral program. In addition to Dr. Aslam, I also had the fortune of having a second excellent adivisor: Dr. Allen H. Meitzler, from Ford Motor Company. Allen's inspiration and enthusiasm have been contagious.

I would also like to thank the members of my orals committee, Dr. Michael Shanblatt, Dr. Timothy Grotjohn and Dr. Jeffrey Ledford for their time and their comments. A very special thanks goes to Dr. Michael A. Tamor, Dr. Shaun McCarthy and Dr. Margherita Zanini for their valuable discussions. I would also like to thank the members of my research group at Michigan State University for their helpful discussions in particular, Nayef Abu-Ageel, Sondes Sahli, Dongsung Hong, Syed Shahzaman and Saeid Khatami.

Many thanks also go to the group at Ford for the technical assistance. In particular I wish to thank: Mr. George Saloka, Mr. Timothy Potter, Mr. Amer Samman, Mr. Mark Sulek, Mr. Bill Vassell, Dr. Bruce Artz, Mr. Larry Cathey, Mr. Michael Parsons, Edith Behringer and Mr. Ron Gilland. I also wish to thank Dr. Chuck Eagen, Mr. Carlton Avant and Mr. Paul Ohtonen for mask fabrication, Georgianna Purnell for low temperature oxide deposition, and Ronald Elder for SEM micrographs.

TABLE OF CONTENTS

LIST OF TABLES

LIST OF FIGURES

CHAPTER 1

Research Motivation and Goal

1.1 Introduction

Today, many sensors are based on silicon device technology. Many of these sensors are piezoresistive. In contrast to an integrated circuit (IC), a sensor must be exposed to its environment in order to function. The use of the piezoresistive silicon sensors has been limited to dry, uncontaminated environments. In general, silicon devices are not suitable for use in chemically harsh, high radiation and high temperature environments. Material technologies superior to silicon are needed for pressure, acceleration and strain sensors to operate in such environments. A promising material for these applications is diamond.

The high thermal conductivity, wide energy gap, chemical resistance, high dielectric strength, radiation hardness, and moderately good carrier mobilities of diamond make it an excellent material for use in sensors. However, natural semiconducting diamond is generally p-type (type II-b) and is too expensive. Therefore, for the last three decades a considerable amount of research has focussed on the development of diamond synthesis methods. The major breakthrough occurred in the early 1980s, when Spitsyn et al. [1] deposited thin diamond films on diamond and non-diamond substrates using a chemical vapor deposition (CVD) technique. This has attracted the

interest of many researchers and has led to the fabrication of low cost, diamond-based semiconductor devices.

Most present devices are fabricated with p-type diamond formed by introducing boron either during deposition of the film or by ion implantation after the film is deposited. However, none of the currently available techniques are suitable for the introduction of donor impurities with reasonable activation energies to create n-type semiconducting diamond. Given the tremendous difficulties in developing a completely new electronic technology, it is not surprising that no crystalline diamond-based semiconductor devices yet demonstrated even approach the performance of their conventional silicon equivalents. However, diamond passive devices do not require crystalline diamond or n-type doping. CVD polycrystalline diamond films can be used for such devices.

1.2 Objective of this Work

The focus of this work is to study piezoresistive properties of CVD diamond films. In view of a huge application potential of diamond sensors, design, fabrication and testing of a multisensor diamond microchip is undertaken. The chip contains a pressure sensor, an accelerometer, a Hall structure, and a variety of other structures.

To overcome the limitation of silicon piezoresistive sensors, there is a definite need for new sensors based on materials with properties that are superior to silicon. The attractive and unique properties of diamond make it a viable candidate for sensors for harsh environment applications. In order to realize the true potential of diamond as piezoresistive material for strain gauges and micro sensor applications, high quality doped and undoped diamond films are needed. The development of a technology compatible with conventional Si fabrication technology, is also important. Therefore, this work had the following objectives:

(1) Grow device quality poly-diamond films.

(2) Characterize the piezoresistive properties of p-type diamond films.

(3) Design and fabricate a diamond multisensor testchip.

1.3 Organization of Dissertation

A review of silicon-based and diamond-based sensors technologies is presented in Chapter 2. After an overview of diamond film deposition methods, nucleation, patterning and doping of diamond films are also presented. Mathematical derivation of the piezoresistive coefficients and gauge factor is also described in this chapter. Chapter 3 describes the deposition system, sample preparation and characterization. Nucleation, patterning and doping methods used in this research and their results are presented in this chapter. The next chapter describes the design and fabrication of a multisensor diamond microchip. Fabrication of micromechanical structures are also described in this chapter. Chapter 5 describes the measurement techniques used in this research. The dependence of gauge factor on doping and temperature dependence is presented in Chapter 6. Finally, Chapter 7 summarizes the results of this study.

CHAPTER 2

Background

2.1 Introduction

In this chapter, an overview of the silicon and diamond-based sensors is presented. Mathematical derivation of the piezoresistive coefficients and gauge factor is described. Physical explanation of the piezoresistive effect in n-type and p-type silicon is also discussed. Chemical vapor deposition methods of diamond film are described in this chapter. Nucleation, patterning and doping of the CVD diamond films are also presented.

2.2 Sensor Background

A sensor is a device that detects a change in a physical parameter such as temperature, pressure, acceleration and light intensity and converts it into a signal which can be measured, usually electrical (see Table 2.1) [2]. The most important effects for sensors in silicon are shown in Table 2.2.

Solid-state sensors have seen rapid developments in the past two decades. The key technology for this growth, is silicon micro-machining. Basically, silicon micro-machining is used to fabricate precise three- dimensional silicon based microstructures

Table 2.1. Signal domains with examples of measurable parameters.

Signal Domains	Examples
Radiant signals	light intensity, wavelength, polarization phase etc.
Thermal signals	temperature, temperature gradient, heat, entropy etc.
Mechanical signals	force, pressure, acceleration, flow, vacuum, thickness, displacement etc.
Electrical signals	voltage, current, electric field, resistance, capacitance etc.
Magnetic signals	field intensity, flux density, permeability etc.
Chemical signals	concentration, toxicity, pH, reduction potential etc.

of great diversity, including thin diaphragms, microbridges and cantilever beams [3]. These micromachined microstructures combined with electronic circuits, have been successfully employed to realize a large variety of solid-state sensors for measuring most of the parameters listed in Table 2.1. The most popular mechanical structure

Table 2.2. Physical effects for sensors in semiconductor material.

Physical Signals	Effect
Radiant signals	photovoltaic effect, photoelectric effect, photoconductivity,
Mechanical signals	piezoresistive effect, capacitive effect, piezojunction effect, piezoelectric effect lateral photoelectric and lateral photovoltaic effect
Thermal signals	Seebeck effect , temperature dependence of conductivity and junctions, Nernst effect
Magnetic signals	Hall effect, magneto-resistance
Chemical signals	ion-sensitive field effect

has been the thin diaphragm. The diaphragm is preferred for most applications.

In the present development of various solid-state sensors, pressure sensors are the most successful and account for a major portion of commercial market. There are basically two types of monolithic silicon pressure sensors, capacitive and piezoresistive. The typical structures of a capacitive and a piezoresistive silicon pressure sensors are schematically illustrated in Fig. 2.1 and Fig. 2.2, respectively. Both types of sensing

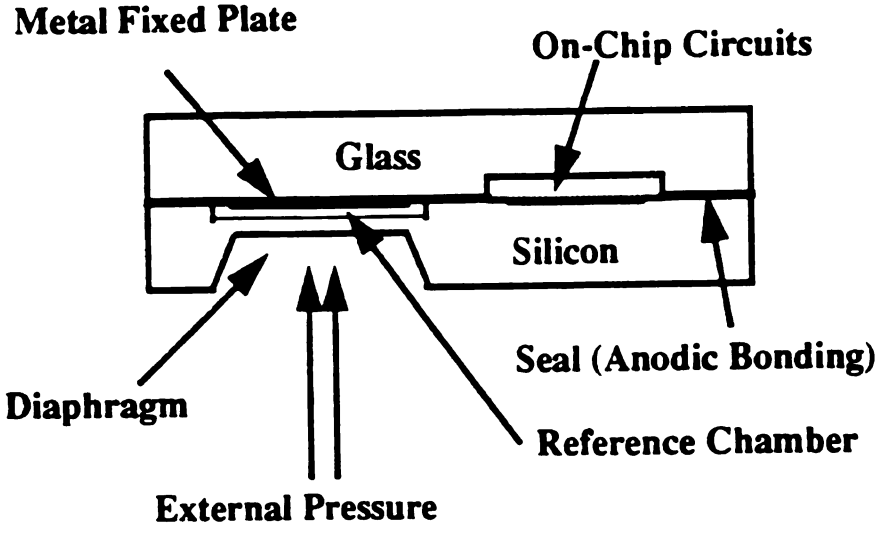

Figure 2.1. Typical structure of a capacitive silicon pressure sensor.

structures embody a thin silicon diaphragm formed by wet etching of the silicon wafer. The silicon wafer is bonded to a glass substrate, normally a 7740 Pyrex glass wafer.

In the capacitive sensors [4], the front surface of the silicon wafer is anodically bonded to the glass substrate. The thin silicon diaphragm and the metalization layer on the glass substrate create a parallel plate capacitor. An applied pressure on the diaphragm deflects it and causes a change in the diaphragm capacitance, which is then detected by a capacitance readout circuitry and can be converted to a voltage or frequency output.

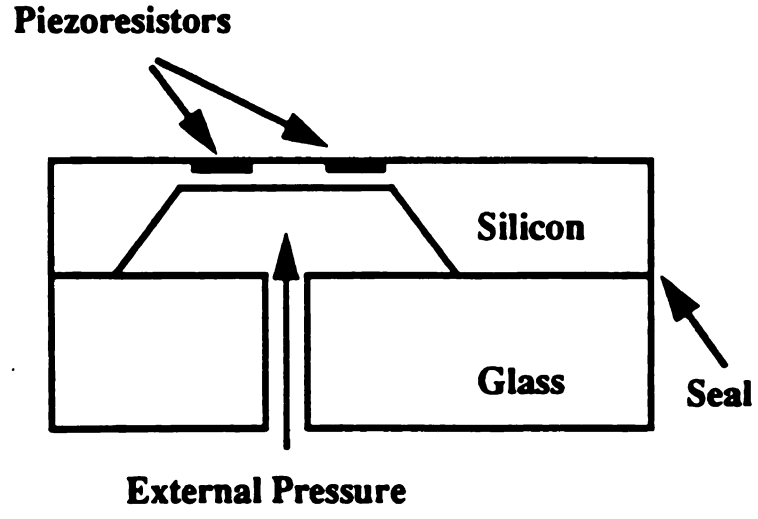

Figure 2.2. Typical structure of a piezoresistive silicon pressure sensor.

In the piezoresistive sensors, the sensing elements are p-type diffused or implanted resistors in the n-type diaphragm material. As the diaphragm is deflected by an applied pressure, the stresses induced in these resistors cause a change in their electrical resistance (the piezoresistive effect), which is detected and is usually converted to a voltage change by Wheatstone bridge circuit [5]. The bridge output voltage is usually amplified and possibly temperature compensated by circuitry usually fabricated on-chip with the sensor. The layout of piezoresistors on the membrane and the Wheatstone bridge circuit are shown in Figure 2.3(a) and Figure 2.3(b), respectively.

The capacitive sensors are more sensitive, less vulnerable to temperature changes, consume less power, but are inherently nonlinear in their pressure response and are scaled poorly [4]. On the other hand, the piezoresistive sensors are easier to manufacture, can be easily scaled down, have a more linear response and, as a result, require less signal conditioning and cost less.

a)

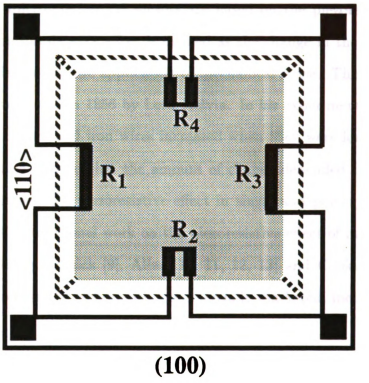

b)

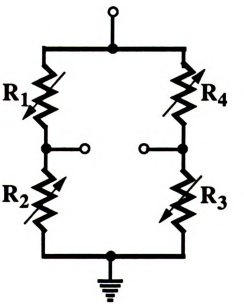

Figure 2.3. Layout of piezoresistors on the membrane (a) and Wheatstone bridge circuit (b) for a typical piezoresistive pressure sensor.

2.3

Current
silicon
tance of
effect wa
the resist
furthermo
Bridgman
in the 19
done in t
effects ar
strain ga

The p
mid 195
silicon,
higher t
in the i
organom
effect to

A us
as the f
piezores
ious ma

The
they are
the use

2.3 Piezoresistive Sensors

Currently, many micro-mechanical sensors are based on the piezoresistive effect in silicon [6]. The piezoresistance effect is defined as the change in the electrical resistance of a material due to the application of mechanical stress. The piezoresistance effect was first discovered in 1856 by Lord Kelvin. In his experiment, he found that the resistance of copper and iron wires increased when they were loaded in tension; furthermore, he also noticed that the amount of change depended on the material. Bridgman also studied the piezoresistive effect in single and polycrystalline metals in the 1920's [7, 8]. Additional work on the piezoresistive effect of many metals was done in the 1930's by Rolnick [9], Allen [10, 11, 12, 13] and Cookson [14]. These effects are now used in the well-known, commercially marketed, metal wire and foil strain gauges [15, 16].

The piezoresistive effect in semiconductors was first studied by C. S. Smith in the mid 1950's [17]. Smith measured the piezoresistance coefficients of germanium and silicon, he found that the semiconductors exhibit piezoresistance coefficients much higher than those of metals. Smith's observations stimulated an increased interest in the investigation of the effects of stress on other semiconductors [18, 19, 20, 21], organometallic crystals and other materials [22, 23], and in the application of this effect to micromechanical sensors [24, 25, 26, 27, 28, 29, 30].

A useful measure of piezoresistance is the gauge factor (GF), which is defined as the fractional change in resistance $\frac{\Delta R}{R}$ per unit strain ϵ. The magnitude of the piezoresistive effect varies between different materials. Typical gauge factors for various materials in the longitudinal direction are shown in Table 2.3.

The magnitude of the gauge factor in some organometallic materials is large but, they are not stable enough to be used in micromechanical sensors [22]. Consequently, the use of these materials has not been as revolutionary as the use of silicon. How-

Table 2.3. gauge factors for various materials in the longitudinal direction.

Material	descriptions	Gauge Factor (GF)
metals [16]	Composition, percent	
Advance	45 Ni, 55 Cu	2.0 to 2.1
Platinum, Tungsten	92 Pt, 8 W	4.0
Nickel	100 Ni	-12.1
Platinum	100 Pt	6.1
Silver	100 Ag	2.9
Copper	100 Cu	2.6
Semiconductors	Types	
Single Crystal Silicon [17, 24, 31]	p-type	+100 to +175
	n-type	-133
Poly- Silicon [18, 19, 32, 33, 34]	p-type	15 to 30
	n-type	-30
Germanium [17, 24]	p-type	+48.7 to +101.5
	n-type	-147 to -157
Poly- Germanium [34, 35]	p-type	+30
	n-type	-30 to -40
Indium-antimonide [24]		-60.5
Silicon Carbide	n-type* α-SiC (6H)[36]	-55 to - 994
	n-type β -SiC [37]	- 26.6 to -31.8
	n-type Poly-SiC [38]	+5 to +10
Organometallic Crystals [22]	Strain ($\mu\epsilon$)	
Magnus'Salt	500	500
$Ir(CO)_2acac$	500	100
Thick Film Resistors [39, 40]	Inks	+8.2 to +12.3

ever, silicon strain gauges are not suitable for chemically harsh, high radiation [41] and high temperature environments [5, 42]. Figure 2.3 shows the effect of the temperature on p-type silicon strain gauges [42]. The gauge factor decreases with increasing temperature for low doping level. The operating temperature of diffused or implanted piezoresistive silicon sensors is often limited to 100 or 125 °C. Since the diffused gauges and the diaphragm have different types of doping impurities, they create p-n diodes. These diodes must be reversed biased in order to channel the current into the gauges. In the case of a dramatic increase in reverse current, its flow in the diaphragm may induce stray voltage that are not easily controlled and may modify the bridge output voltage. Therefore, silicon-based piezoresistive sensors in addition to the chemical and radiation environment problems, can not operate over 125 °C due to the p-n junction effect.

The piezoresistive effect of polycrystalline silicon films was also investigated by many workers [18, 19, 33]. The gauge factor of the polysilicon films was found to range from less than 10 to about 25 depending on the resistivity [19]. The polysilicon piezoresistor offers the advantage of a potentially higher operating temperature limit than diffused single crystal Si piezoresistor, because p-n junction piezoresistor isolation is not required. Use of polycrystalline film resistors increases the operating temperature range of the sensor to 200 °C. This is because the polysilicon piezoresistors can be deposited on insulator layer, this is known as silicon on insulator (SOI). However, the sensitivity of polycrystalline silicon piezoresistors is lower than that of single crystal silicon resistors (see Table 2.3).

2.3.1 Piezoresistive Coefficients

The piezoresistive effect is defined as the change in the electrical resistance of a material due to the application of mechanical stress or strain.

From a mathematical point of view, the effect of homogeneous mechanical stress

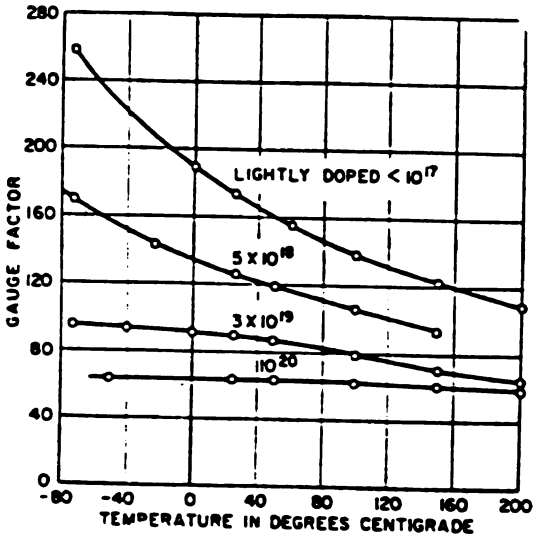

Figure 2.4. Effect of the temperature on p-type silicon strain gauges.

on the electrical resistance of a conducting crystal can be described generally in terms of a set of constants. These constants are known as the piezoresistance coefficients. However, in most practical cases the piezoresistive effect is characterized by the gauge factor. The expressions for the piezoresistive coefficient and the gauge factor are briefly derived next. More detailed derivations are given in appendix A and appendix B for piezoresistive coefficients and gauge factor, respectively.

In a material subjected to stress X_{kl}, the electric field E_i is a function of the current density J_j and stress X_{kl} which can be written as [24, 30, 42].

$$E_i = \rho_{ij} J_j + \pi_{ijkl} J_j X_{kl} \qquad i,j,k,l = 1,2,3 \tag{2.1}$$

where ρ_{ij} is the resistivity, and π_{ijkl} is the piezoresistive tensor. Equation (2.1) is

deriv

In th

by [2

π_{ijkl}

where

sistive

For lo

same

where

For

In Eq. (

[010] dir

In ar

derived in appendix A Eq. (A.9). The stress can be written as

$$X_{kl} = \begin{cases} X_l & \text{for longitudinal stress} \\ X_t & \text{for transverse stress} \\ X_s & \text{for shear stress} \end{cases} \tag{2.2}$$

In the case of crystals with cubic symmetry, such as diamond and silicon, π_{ijkl} is given by [24]

$$\pi_{ijkl} = \begin{cases} \rho_0\, \pi_{11} & \text{if both J and } X \text{ are in one of the } \{100\} \text{ directions} \\ \rho_0\, \pi_{12} & \text{if J and } X \text{ are in one of the } \{100\} \text{ directions but are perpendicular to each other} \\ \rho_0\, \frac{\pi_{44}}{2} & \text{for shear stress} \end{cases} \tag{2.3}$$

where π_{11}, π_{12}, and π_{44} are the fundamental longitudinal, transverse and shear piezoresistive coefficients, respectively [17]. ρ_0 is the resistivity under zero stress.

For longitudinal case (the current density and the mechanical stress are all in the same direction, e.g. [100]), the piezoresistive coefficient is given by

$$\pi_{11} = \frac{\rho - \rho_0}{\rho_0} \frac{1}{X_1} \tag{2.4}$$

where the subscript 1 denotes [100] direction, $X_1 = X_l$.

For transverse case, the piezoresistive coefficient is given by

$$\pi_{12} = \frac{\rho - \rho_0}{\rho_0} \frac{1}{X_2} \tag{2.5}$$

In Eq. (2.5), the current density is assumed in [100] direction whereas the stress is in [010] direction.

In arbitrary directions, following similar derivation as (2.4) and (2.5) the piezore-

sistive

for arbit

for arbitr

In arb

of the fu

For t

30].

and for

where

For ra

can b

given

where

ple co

and t

sistive coefficients can be written as

$$\pi_l = \frac{\rho_1' - \rho_0}{\rho_0} \frac{1}{X_1'} \tag{2.6}$$

for arbitrary longitudinal direction and

$$\pi_t = \frac{\rho_1' - \rho_0}{\rho_0} \frac{1}{X_2'} \tag{2.7}$$

for arbitrary transverse direction. The primed quantities refer to arbitrary direction.

In arbitrary direction, the piezoresistance coefficient can also be expressed in terms of the fundamental piezoresistance coefficients and the direction cosines.

For the longitudinal case, the piezoresistance coefficient can be written as [24, 42, 30].

$$\pi_l = \pi_{11} - 2(\pi_{11} - \pi_{12} - \pi_{44})(l_1^2 m_1^2 + m_1^2 n_1^2 + n_1^2 l_1^2) \tag{2.8}$$

and for transverse case, the piezoresistive coefficient can be written as

$$\pi_t = \pi_{12} + (\pi_{11} - \pi_{12} - \pi_{44})(l_1^2 l_2^2 + m_1^2 m_2^2 + n_1^2 n_2^2) \tag{2.9}$$

where l_i, m_i, and n_i (i = 1,2,3) are the direction cosines of the transformation.
For randomly oriented polycrystalline films the longitudinal piezoresistive coefficient can be estimated by averaging of π_l in Eq.(A.27) over all possible directions and is given by [43]

$$< \pi_d > = \frac{\int_{\theta=0}^{\theta=\frac{\pi}{2}} \int_{\phi=0}^{\phi=\frac{\pi}{4}} \pi_l \, d\theta d\phi}{\int_{\theta=0}^{\theta=\frac{\pi}{2}} \int_{\phi=0}^{\phi=\frac{\pi}{4}} d\theta d\phi} \tag{2.10}$$

where θ and ϕ are the angles between the arbitrary coordinate system and the principle coordinate system aligned with the crystal axes. d denotes l and t for longitudinal and transverse directions, respectively.

2.3.2

The m

sistive g

which f

for lon

for th

ϵ_i an

$\Delta\rho$ =

respe

F

the c

by [4

Fo

(mon

(polyc

2.3.2 Gauge Factor Expressions

The most suitable and practical quantity in microsensor applications is the piezoresistive gauge factor (GF), which is normally measured, and is defined by

$$GF = \frac{\Delta R}{R}\frac{1}{\epsilon} \tag{2.11}$$

which for isotropic materials can be written as [24]

$$GF_{il} = \frac{\Delta\rho}{\rho_0}\frac{1}{\epsilon_l} + (1 + 2\nu) \tag{2.12}$$

for longitudinal direction (see appendix B equation (B.4)), and

$$GF_{it} = \frac{\Delta\rho}{\rho_0}\frac{1}{\epsilon_l} - 1 \tag{2.13}$$

for the transverse direction (see appendix B equation (B.6)). In above equations ν, ϵ_l and ρ are the Poisson's ratio, longitudinal strain and resistivity, respectively, and $\Delta\rho = \rho$ - ρ_0. The subscripts i, l, and t refer to isotropic, longitudinal and transverse, respectively. ρ_0 is the unstrained resistivity.

For an anisotropic homogeneous material, the gauge factor is given in terms of the compliance coefficients S_{11}, S_{12} and the longitudinal piezoresistive coefficients π_l by [44, 45]

$$\mathrm{GF_{al}} = 1 - 2\frac{S_{12}}{S_{11}} + \frac{\pi_l}{S_{11}} \tag{2.14}$$

For diamond S_{11} = 0.09493 x10^{-12} cm^2/dyne, S_{12} = 0.00978 x10^{-12} cm^2/dyne (monocrystal diamond), $\nu \approx$ 0.07 and *Young's modulus* Y = 11.43 x 10^{12} dynes/cm^2 (polycrystalline diamond) [46, 47, 48] and the equations (2.12),(2.13) and (2.14) can

be written as

$$GF_{il} = \frac{\Delta\rho}{\rho_0}\frac{1}{\epsilon_l} \tag{2.15}$$

$$GF_{it} = \frac{\Delta\rho}{\rho_0}\frac{1}{\epsilon_l} - 1 \tag{2.16}$$

$$GF_{al} = \frac{\pi_l}{S_{11}} \tag{2.17}$$

the anisotropic transverse gauge factor can be written as

$$GF_{at} = \frac{\pi_t}{S_{11}} \tag{2.18}$$

Now for randomly oriented polycrystalline diamond films the longitudinal piezoresistive coefficient can be determined using Hook's law and equations (2.6), (2.10) and (2.15):

$$< \pi_l > = GF_{il}\,\frac{1}{Y} \tag{2.19}$$

$< \pi_t >$ can be determined using Hook's law and equations (2.7), (2.10) and (2.16):

$$< \pi_t > = GF_{it}\,\frac{1}{Y} \tag{2.20}$$

In the case of monocrystalline diamond films π_l and π_t are given by [44, 45]:

$$\pi_l = S_{11}\,GF_{al} \tag{2.21}$$

$$\pi_t = S_{11}\, GF_{at} \tag{2.22}$$

2.3.3 Explanation of the Piezoresistive Effect

The piezoresistive effect in n-type semiconductor materials was explained by the many-valley model developed by Herring [49]. In silicon the constant energy surfaces are ellipsoidal in form. A total of six equivalent energy minima exist along the <100> directions in n-type silicon (<100> valley model). Because the surfaces are ellipsoidal the effective mass of an electron in each valley is anisotropic. Hence, the mobility associated with each valley is anisotropic although the overall mobility is not.

For a qualitative explanation of the piezoresistive effect in n-type silicon, let us for simplicity, call the [100], [010] and [001] valleys as $k_x valley$, $k_y valley$ and $k_z valley$, respectively. In the absence of strain all the valleys are equally populated with electrons due to crystal symmetry. The energy minima are all located at the same energy level. When a uniaxial tensile stress is applied, for example, in [100] direction, the lattice spacing increases in [100] and $[\bar{1}00]$ directions, whereas in the directions perpendicular to this direction ([010], $[0\bar{1}0]$, [001] and $[00\bar{1}]$) the lattice spacing decreases. As a result, the two energy minima along the considered direction of the stress are raised with respect to the other four energy minima. The result is to cause more carriers to be scattered into the $k_y valley$ and $k_z valley$, than are scattered into the $k_x valley$. The ellipses in Figure 2.5 represent cross-sections of constant energy centered about E_c. For simplicity two valleys are only shown in Fig. 2.5. These are $k_x valley$ and $k_y valley$. In the absence of strain, the two ellipsoids are equal in size. Within each ellipsoid, there are two groups of electrons with different effective mass. These two groups of electrons have different mobilities, that is, the mobility of electron μ_{xy} in a direction perpendicular to the major axis of the valley is larger than the mobility of

electron μ_{xx} in a parallel direction.

The effect of the uniaxial tensile stress applied along the [100] direction, is shown schematically in Fig. 2.5, by the decrease in the valley size along the [100] direction and an increase in the [010] valley size. The effect of stress on the valley energies is indicated by the dotted ellipsoids. An increase in the size of an ellipsoid corresponds to a lowering of the band edge. Now, if an electric field is applied along the direction of the mechanical stress (longitudinal direction), the resistivity will decrease. This is because, the application of the stress has resulted more electrons of high mobility (small effective mass) and fewer electrons of low mobility (large effective mass) in the field direction. This has been observed experimentally by the negative piezoresistive coefficient of n-type silicon [17]

The piezoresistive effect in p-type silicon is still not clear. The constant energy surfaces in the valence band are much more complicated than the conduction band due to the degeneracy. A simplified and roughly drawn energy band diagram of p-type silicon is shown in Fig. 2.6(a) [50, 51, 52]. Because of the degeneracy at $k = (000)$ the constant energy surfaces of the valence band cannot be described as ellipsoids or spheres, but they are warped in such a way to retain their cubic symmetry.

The application of uniaxial stresses to the crystal lifts the cubic symmetry and removes the degeneracy at $k = 0$ of the valence band which is responsible for the warping of the surfaces. This causes the subbands to be shifted relative to each other [50, 51, 52]. This results in transfer of carriers between heavy holes and light holes. Under uniaxial tensile stress, the heavy hole subband moves up and the light hole subband moves down (Fig. 2.6(b)), as a result more carriers with low mobility and less carriers with high mobility. The resistance increases with tensile stress, which has been observed experimentally by the positive value of the piezoresistive coefficient or gauge factor [17].

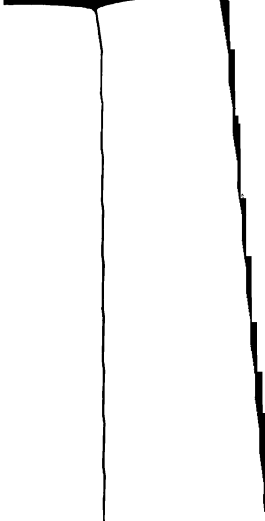

Figur

2.4

Since
synthe
succes
(GE)

Di
is tetr
hybrid
visuali
so that
octahe
respect

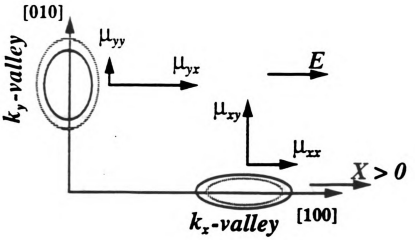

Figure 2.5. Cross-section of constant energy for n-type silicon centered about E_c.

2.4 Diamond Properties

Since the discovery that diamond is a crystalline form of carbon many attempts to synthesize diamond have been made, but these attempts have met with only limited success. It was not until the 1955 [53, 54, 55], when scientists at General Electric (GE) succeeded in producing synthetic diamonds.

Diamond is the densest form of carbon. In the diamond lattice each carbon atom is tetrahedrally coordinated, making strong , covalent bonds to its neighbors, using hybrid sp^3 atomic orbitals that give it hardness and strength. The lattice can also be visualized as planes stacked in an ABC ABC ABC sequence along < 111 > directions so that every third layer is identical. Natural diamonds are most commonly found in octahedral and dodecahedral shapes with faces parallel to {111} and {110} planes, respectively. Simple cubic diamonds with faces parallel to {100} faces also exist, but

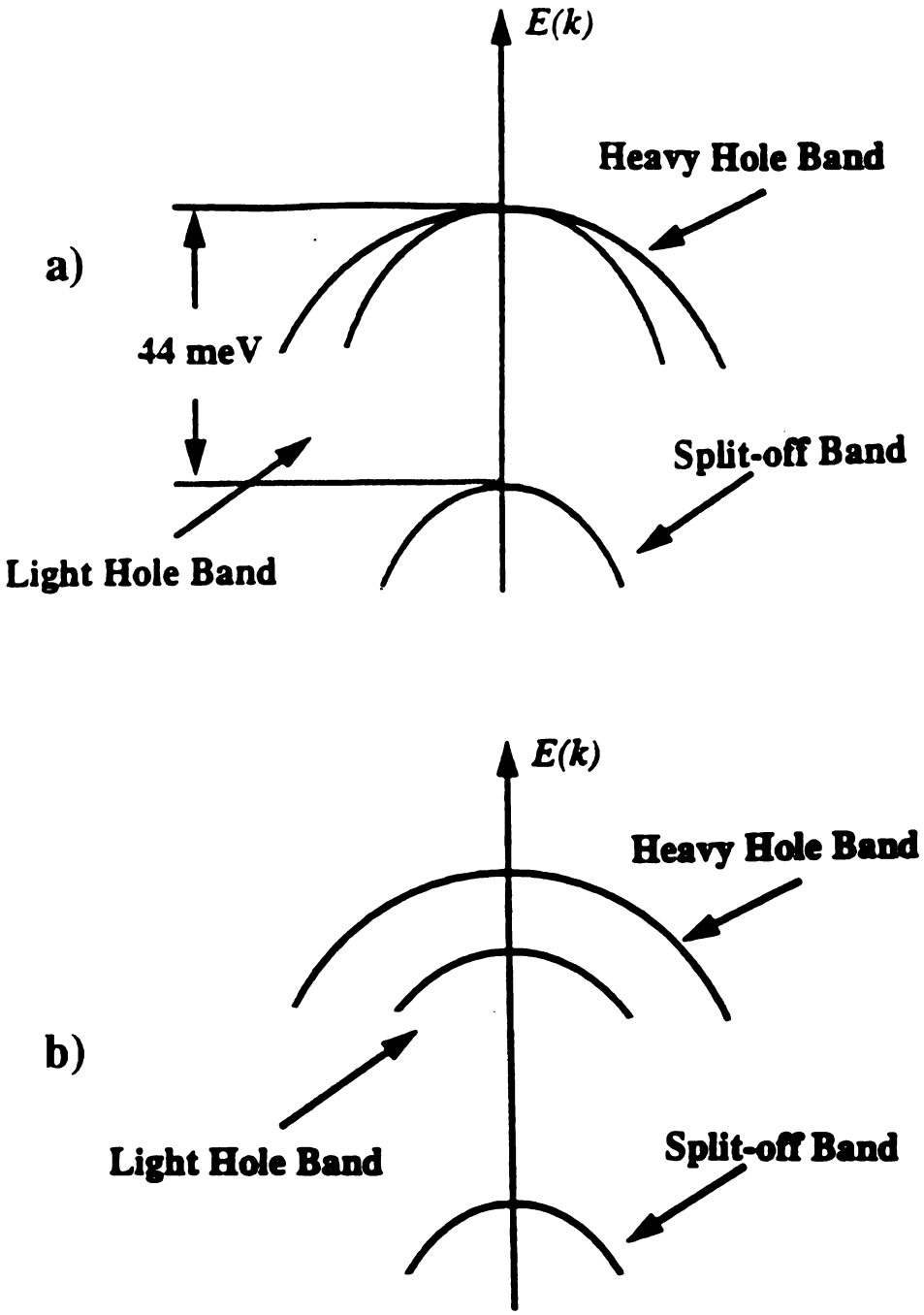

Figure 2.6. A simplified and roughly drawn energy band diagram of p-type silicon (a) zero stress and (b) with uniaxial stress.

these are less common [55].

Diamond has long been known to be the strongest and the hardest of all materials. Its knoop hardness is $\approx$ 100 GPa [56]. Diamond has the highest Young's modulus of any materials. Its Young's modulus is 10.5×10^{12} dynes/cm^2 which is five times that of the silicon [46, 47, 48]. A potential application of these properties is in micromechanical transducers which may be made very thin and yet remain rigid [57, 58, 59, 60, 61, 62]. It also exhibits low friction coefficient of 0.05 in the $< 110 >$ type I natural diamond, which is similar to that of Teflon [56, 63]. This low coefficient is believed to result from a hydrogen termination of the surface. The low coefficient of friction is particularly relevant in extending the tool life of diamond cutting tools by reducing heat generations.

The thermal conductivity of diamond at room temperature is higher than that of any other material [64, 65]. It is 5 times greater than that of copper, 13 times that of silicon, and 43 times that of gallium arsenide. This conductivity derives from phonon propagation. It is exceptionally efficient when used as a heat spreader.

The thermal expansion coefficient of diamond at room temperature is 0.8×10^{-6} °C^{-1}, lower than that of Invar. This is caused by the very strong binding force of diamond. The thermal expansion coefficients of diamond and silicon as a function of temperature is shown in Fig. 2.7. [66, 67, 68].

Diamond is virtually immune to chemical attack by all substances unless they are energetic (e.g., ion beams)[69] and those which act as oxidizing agents at high temperature. It has been known that if a diamond is heated to a temperature of about 600- 700 °C or higher (depending on the initial quality of the diamond) in pure oxygen or even in air, it will wholly or partially oxidized to CO and CO_2. If diamond is heated in the absence of oxygen, preferably in vacuum, to a temperature of about 1400- 1500 °C or higher (again depending on the quality of the diamond), it will be wholly or partially converted to graphite [70, 71]. Molten potassium and sodium

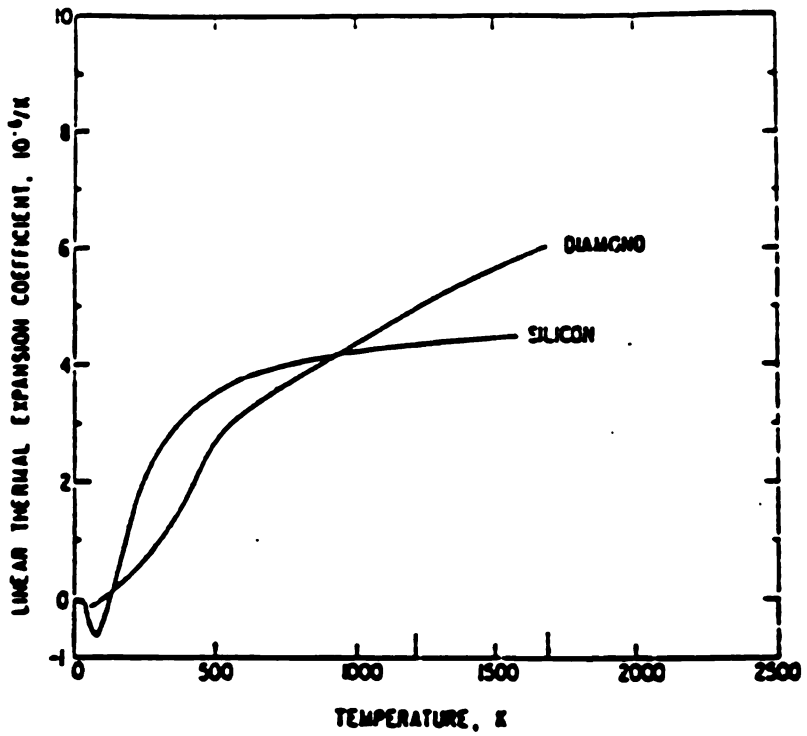

Figure 2.7. Thermal expansion coefficients of diamond and silicon as a function of temperature.

Table 2.4. Comparison of diamond properties and some commonly used semiconductor materials.

Properties	Materials				
	Si	GaAs	SiC	Diamond	
				Natural	CVD
Band Gap (eV)	1.12	1.42	3.0	5.45	5.45
Carrier mobility					
Electron (cm^2/ V.s)	1450	8500	400	1800 -2000	
Hole (cm^2/ V.s)	500	400	50	1600 - 2100	(10-1000)[74, 75, 76]
Dielectric constant	11.7	10.9	10	5.7	6.5[77]
Breakdown					
(V/cm) x 10^6	0.37 - 0.5	0.6	2 - 3	(4-20)[78]	
Resistivity (Ohm-cm)					
Intrinsic	$1x10^3$	1 x 10^8		1 x 10^{16}	(10^6-10^{14})[79]
Thermal conductivity					
(W/cm.°K)	1.5	0.5	5	10-20	(10-20)[80, 81]
Thermal					
expansion x 10^{-6}/°C	2.6	5.9	4.7	1.1	2.6[80]
Lattice constant ($\AA$)	5.431	5.653	4.36	3.57	3.57
Melting point (°C)	1412	1240	2540	3827	
Density (g/cm^3)	2.329	5.317	3.216	3.52	3.52
Hardness (GPa)	8.5		24.8	100	70 - 100
Young's					
modulus (GPa)	130 - 180	85	700	1050 - 1200	(800-1180)[47, 82]
Poisson's ratio	0.22 - 0.24	0.31 - 0.32		0.1-0.21	(0.071-0.148)[47, 82]

nitrides are most commonly known to attack the diamond surface at a temperature in the range 427-827 °C [55, 72, 73].

Electrically, pure diamond is an excellent insulator. The band gap associated with the indirect transition between the valence and the conduction bands is as large as 5.48 eV. Table 4 [3, 57, 68, 80, 81, 83, 84, 85] provides a comparison of some of the most important material parameters between most commonly used semiconductors and diamond. The electrical properties of diamond exceed those of other semiconductors. Diamond should be a good candidate for high temperature (due to large band gap) high speed (due to carrier mobility) and high power (due to high thermal conductivity

and breakdown voltage) electronic devices.

According to impurity content, optical, and electrical properties, diamond is grouped into four distinct types: I-a, I-b, II-a, and II-b [55].

(i) Type I-a: These diamonds are often nearly colorless, but they may also be yellow, brown or gray; they are optically transparent and are believed to be less perfectly crystalline. Their electrical resistivity is greater than $10^{16}\Omega - cm$.

(ii) Type I-b: These diamonds contain up to 0.2% paramagnetic nitrogen which is present on isolated substitutional lattice sites. Most of the synthetic diamonds produced under high pressure are typically type Ib.

(iii) Type II-a: These type of diamonds are very rare in nature, and are generally believed to be the most perfectly crystalline, practically free of nitrogen, near-colorless and are transparent in the ranges 220 nm to 2.5 μm and $> 6\mu$m. and are absorbed to IR in the range 2.5 μm to 6 μm. Thermal conductivity at room temperature ranges up to 26 W/cm-K. Electrical resistivity is in general similar to type Ia diamonds.

(iv) Type II-b: Extremely rare in nature, these diamonds contain boron in small quantities and are usually blue or gray in color. They are p-type semiconductors with electrical resistivity of only 10 to 1000 Ω-cm.

2.5 Diamond Technology

In 1954 researchers at General Electric succeeded in converting graphite to diamond under high pressure and high temperature (HPHT) conditions [53]. Typically synthetic diamond is fabricated at temperatures around 4237 K and a pressures near 200 kbar [53]. By the use of a metallic catalyst such as nickel and iron, the conversion rates from graphite to diamond can be increased, and temperature and pressure can be reduced to around 1500 °C and 50 Kbar respectively [86, 87, 88, 89]. However, synthetic diamond made by HPHT process has a variety of disadvantages, such

high pressure conversions are costly and require a small growth chamber, so that the method is only suitable for production of diamond in the form of small pieces, grit, and powder, but it is not suitable for large area coverage. Using a metal catalyst creates metal inclusions and small voids in the diamond films. These metal inclusions have a different thermal expansion coefficient than that of the diamond and cause internal stresses to develop and weaken the diamond, that make them unsuitable for use in semiconductor devices.

In the late 1960s, two separate groups, one from the Soviet Union led by Boris Deryaguin and the other from the United States headed by John Angus, independently showed that diamonds could be deposited on diamond seed crystals at low pressure from a vapor of hydrocarbons and hydrocarbon-hydrogen mixtures [87, 90]. Angus and co-workers were the first to report on the preferential etching of graphite compared to diamond by atomic hydrogen. By the mid 1970s diamond growth at low pressures had been achieved by several groups [1, 91, 92]. The beneficial role of hydrogen was known and understood to some extent and growth rates of <0.1 μm /hour had been achieved. However, the use of diamond as a substrate and the low growth rates attained were the major reasons for the process being judged to be impractical. Nevertheless, the critical role of atomic hydrogen in achieving metastable diamond growth as a preferential etchant for removing graphite against diamond was established, and these results provided the experimental foundation for much of the work that followed. Moreover, this process produces diamond that is free of inclusions. An important breakthrough by Soviet scientists in early 1970's indicated the conditions under which gas activation techniques can greatly increase the growth rate of diamond and suppress the graphite deposition. Soviet scientists also announced that they had grown crystalline diamond on non-diamond substrates but they released no details about their method. Finally, in the early 1980s a Japanese group at the National Institute for Research in Inorganic Materials, under the direction of

Nobuo Setaka and Seiichiro Matsumoto [93], deposited diamond with high growth rates by chemical vapor deposition on diamond and non-diamond substrates using different techniques. These latter disclosures led to worldwide interest.

The most successful growth method has been in the deposition of diamond from hydrocarbon-hydrogen gas mixtures. Methane (CH_4) and acetylene (C_2H_2) are the most common carbon-containing gas species which have been used for diamond deposition . The percentage of the hydrocarbon gas is generally 0.1- 5.0% depending on the growth technique and the desired film quality versus growth rate. Similar substrates temperatures are used in most of the low-pressure experiments (~600° to 1000 °C).

Other hydrocarbon gases such as ethane, ethylene and acetylene can also be used to deposit diamond in the microwave plasma CVD method. For hot filament deposition, Hirose and his co-workers [94], have shown that various organic compounds including acetone ($CH_3 - CO - CH_3$), ethanol ($CH_3 - CH_2 - OH$), methanol (CH_3OH) and diethyle ether ($C_2H_5OC_2H_5$) can also be used to deposit diamond films. Growth rate of 8 μm/h were also reported [94] by using these organic compounds in the hot filament method, approximately 20 times greater than those obtained when methane is used in a similar system. Oxygen can be added, either directly or as an integral part of the carbon carrier, and can have a marked influence on the deposition process. The variation in growth rate is possibly due to varying efficiency of each compound in supplying C_2H_2, CH_3, and other radicals thought to be mainly responsible for diamond growth[95]. Deposits may vary from nanocrystalline to single crystal diamond with no or little non-diamond C, depending upon proportions of C, H, or O in the supply of gases, but without reference to type of gas phases activation used.

With a correct set of other important deposition parameters, such as pressure, substrate temperature or power density in the activation zone, the C-H-O diagram give a clear picture on where to search for diamond. The vast majority of diamond

CVD experiments started from less than 5% methane in hydrogen [96]. Depending on the quality criteria and diamond detection methods applied, the upper concentration limit for diamond formation from CH_4-H_2 mixtures is somewhere between 3% and 4% [96]. For methane concentrations around 3%-5% small additional amounts of oxygen would shift data points off the C-H sideline into the diamond domain.

Atomic hydrogen serves several critical roles in the temperature range of CVD diamond growth. First, stabilization of diamond surface, that is to prevent the diamond surface from reconstruction into a graphitic like surface containing a mixture of sp^2 and sp bonds and to satisfy the dangling bond of the surface by preserving the sp^3 like bond (diamond). Second, reaction with surface hydrogen to form H_2 and leave a vacant surface site in which a reactive carbon species may attach. Finally, etchant for graphite which forms simultaneously with diamond.

Oxygen also play an important role in the growth mechanism of CVD diamond. Various studies [97, 98] have shown that addition of oxygen in HFCVD growth environment leads to increase of atomic hydrogen concentration at the surface of diamond which in turns contribute to the purification of diamond films even at low temperature. Direct oxidation of non-diamond carbon is also enhanced by the presence of the O_2. Oxygen also improves the formation of additional radicals in the gas phase which is necessary for diamond growth. Oxygen also causes increase in atomic carbon density by the destruction of gas phase pyrocarbon-forming species. Forming OH gas phase which attack the non-diamond carbon. The range of total pressure at which diamond could be obtained was extended by the addition of oxygen. Optimum results were obtained for gas mixtures of O_2:CH_4:H_2 =0.2:0.8:50 SCCM [98].

The precise effect in the growth mechanism of CVD diamond from the hydrogen and the oxygen is still debated.

2.5.1

So far
of dia
freque
and m
[108].
carrie
by th
these
linear
per h

H
temp
close
°C. T
hour
given

M
used
micr
wave
carbo
at a p
conce
μm p
were r

2.5.1 Chemical Vapor Deposition Methods

So far, several techniques have been developed for chemical vapor deposition (CVD) of diamond [87, 93, 99, 100, 101], such as hot filament (HFCVD) [93, 94], radio frequency (rf) plasma [102, 103], d.c. plasma [104, 105], microwave discharge [99, 106] and microwave plasma disk reactor [107]. Other deposition method was also reported [108]. All of these methods have in common that diamond is deposited from a carbon carrier gas that is decomposed and the formation of non-diamond carbon is prevented by the presence of a selective etchant such as atomic hydrogen or oxygen. Some of these diamond CVD methods are capable of producing the desired carbon phase at linear growth rates of 0.1 to 1 μm per hour while for other methods up to 180 μm per hour were reported [102].

Hot filament HFCVD system consists of tungsten filament which is heated to a temperature range of $\approx$ 2000-2400 °C and a substrate holder which is usually mounted close to the filament and independently heated to temperatures between 800- 1000 °C. The growth rates in HFCVD reactor is usually in the order of 0.5 to 10 μm per hour depending on the gases employed. More details on the HFCVD system will be given in the next section.

Microwave plasma in the high frequency range (2.45 GHz) has been extensively used for the deposition of diamond films [99, 109]. The reaction chamber in a typical microwave plasma is composed of a quartz tube which is placed inside a microwave waveguide and a substrate holder which is positioned inside the tube. Plasma of carbon carrier gas and hydrogen mixtures are formed and diamond were deposited at a pressure of 10- 100 torr, a substrate temperature of 800- 1000 °C, and methane concentrations of 0.2 - 5.0 % in hydrogen. Generally, linear growth rates of 0.5 - 5 μm per hour were achieved. Rates up to 30 μm/hour under atmospheric pressure were reported using a microwave torch reactor, which was developed by Mitsuda et

al [110]. Growth of diamond films on silicon and other substrates at low temperature < 500 °C were also reported [111, 112]. J. Wei, et al. deposited diamond films on Al substrates at 0.1 Torr and 500 °C using magneto-microwave plasma [113].

A high quality diamond film was also achieved in a large area by a Microwave plasma disk reactor (MPDR) [107]. The MPDR was developed at Michigan State University by Asmussen *et al.* [114]. The MPDR system is an electrodeless, internally tuned reactor design which uses a circular cylindrical cavity which can be adjusted to a single resonant mode by means of two degrees of tuning. Microwaves are introduced into the system via a short antenna, which is a coaxial microwave input probe. The processing vacuum chamber is composed of a quartz disk, a graphite substrate holder which is held by two quartz tubes, stainless steel baseplate and a perforated stainless steel sheet which is affixed to the baseplate in the bottom part of the processing chamber and serves to terminate the cavity and still allow gas to flow through. The height of the quartz disk is 6 cm and its inner diameter is 9.25 cm. The quartz disk sits on 3.5 cm thick stainless steel baseplate. The MPDR is scalable with frequency (915 MHz/ 2.45 GHz) which allows for the possibilities of depositing uniform diamond film on large area. [115]

Radio frequency plasma technique developed by S. Matsumoto, et al [102] operated at atmospheric pressure, has also been used to deposit diamond. In this method, rf of 4 MHz inductive heating and a power of 60 kW were used. Up to 10 % methane concentrations (much higher than in other techniques) could be used. High quality diamond films at growth rate up to 180 μm per hour were obtained on molybdenum substrates. However, the handling of such plasmas is not easy, the plasma temperature was estimated to be greater than 4000 °C.

2.5.2 Nucleation

Generally, the nucleation density for diamond growth on non-diamond substrates is very low, roughly 10^4 cm^{-2}. Enhancing nucleation on a wafer surface is the requirement for the development of a pinhole-free film in a reasonable deposition time. Several techniques have been used to enhance the nucleation density for diamond growth on non-diamond substrates by many investigators. The most commonly known technique is based on scratching the host substrate manually or via ultrasonic by diamond powder [106, 116, 117].

In the case of diamond powder the nucleation on the substrate can be achieved by abrading the surface directly with the powder [116], or by ultrasonic treatment in a suspension of diamond powder in organic solvents, such as ethyl alcohol, methanol, etc. [118, 119]. Following the treatment, the substrate is always rinsed by deionized water or by one or more organic solvents. This method has substantially increased the nucleation density of diamond growth by several orders of magnitude, up to 10^{11} cm^{-2} has been reported [106, 116].

More recently a novel technique was developed at Michigan State University, which does not require scratching of the substrate [119]. This method is based on spreading diamond seed crystals, suspended in photoresist, on the substrate surface. During CVD diamond deposition, the photo-resist evaporates in initial stages and the diamond particles act as nucleation sites for the diamond growth. The nucleation density of this method is relatively 5-8 times smaller than that of ultrasonic or damaging treatment [119]. However, this method is compatible with the lithographic process used in IC technology. The nucleation density and the grain size in the deposited diamond film is easily controllable through the size and density of diamond particles to be suspended in the photo-resist and the spin speed of substrate during photo-resist coating [119]. A further extension of the method has resulted in nucleation densities

in the range of 10^{11} cm^{-2} [120].

Transmission electron microscopy (TEM) indicates that scratching leaves very small plaques of diamond ≈ 50 $\AA$ in size, which serve as nucleation sites for diamond growth [121]. It has been also reported that diamond nucleation density was enhanced by only sand-blasting the silicon wafer without using the diamond powder[103].

2.5.3 Effect of Substrate Temperature

The typical substrate temperature for diamond CVD, growth on a variety of substrates, in almost all the techniques, is in the range of 800-1000°C. Lowering the substrate temperatures usually results in the formation of the amorphous carbon films which contain mixed bonding of sp^3 and sp^2. Low temperature growth of pure diamond films is an important goal for the extension of diamond applications towards semiconductor, optical emitting materials as well as optical and mechanical coating materials or heat sinks. Ramesham *et al.* [122] used a high pressure microwave plasma-assisted (HPMA) chemical vapor deposition system to grow low temperature diamond films. It was observed that deposition at lower temperatures (460-600°C) requires a higher percentage of methane than at higher temperatures (800-1000°C) [111, 112, 122]. It was also noted that, as the substrate temperature decreases, deposition rate decreases, smoothness increases, and diamond crystal size decreases [122]. Liou *et al.* [123] have deposited diamond on different substrates at low temperatures in a microwave plasma enhanced chemical vapor deposition (MPCVD) system. they have reported that, diamond could be deposited at less than 300°C via the addition of oxygen to the gas mixtures. Films deposited without oxygen were white soot coatings and easily scraped off. The deposition rates of films on silicon with 2% methane drop down quickly with decreasing substrate temperatures. The deposition rate decreases as the oxygen concentration increases. However, the quality of the diamond deposited films was increased with increasing oxygen concentrations[123]. Most of

the reported results on the deposition of diamond at low temperatures were achieved by plasma CVD systems. However, highly crystallized and purified films has never been reported.

Low temperature diamond deposition by hot filament chemical vapor deposition system HFCVD has not yet been achieved. Matsumoto *et al.* [93] in their first reported experiment, they deposited diamond at a substrates temperatures in the range of 600-1000°C using HFCVD system. They found that lower temperatures (600 -700°C) decreased the number and size of the diamond particles formed. In addition, no continuous film was reported by these authors, this might be due to that, no special method to enhance nucleation was used.

Kikuchi *et al.* [124] deposited a continuous film by HFCVD systems, where the temperature of the surface of the substrate was kept at 750°C with radiation from the filaments. The silicon substrate was scratched by 3 μm diamond powders before deposition. High quality and continuous diamond films were achieved after 12 and 16 hours deposition time for 1% and 0.5% methane concentrations in hydrogen, respectively. The effect of substrate temperature was also studied by A. Masood at Michigan State University [125] using HFCVD method. It was observed that the quality of the diamond film improves when the temperature increases from 830°C to 890°C and then the quality shows some deterioration at a temperature greater than 900°C. It was also observed that the growth rate of the diamond films increases with increasing temperatures from 830°C to 890°C. It is very important to known that, when the substrate temperature is greater than 1300°C, only graphitic carbon, if any, is deposited.

2.5.4 Diamond Film Characterization

An extensive range of analytical techniques are currently used to monitor and characterize various stages of CVD process of diamond. Most of them are, however,

used either to study in situ gas reaction and substrate surface chemistry or physical composition of the films. In this research, diamond films will be characterized after deposition. Raman spectroscopy, scanning electron microscope (SEM) and surface profilometers will be used in this work. A brief description of each in context with its specific use in diamond film characterization is given here.

Raman Spectroscopy

Raman spectroscopy is based on the phenomenon of inelastic scattering of radiation by a medium. In case of diamond, they are dominated by the intramolecular vibrational transitions corresponding to optical phonons.

Raman spectroscopy is widely used in CVD diamond characterization due to its high sensitivity not only to crystalline material, but also to the various possible non-crystalline phases. A factor of 30 for the ratio of graphite to diamond has been reported [126]. Raman analysis for natural diamond indicate a strong peak at relative wavenumber of 1332 cm^{-1} [127]. Well-ordered graphite, similarly, has only one Raman peak at $\approx$1600 cm^{-1} [128]. The presence of disorder or small crystallite size gives rise to a peak at 1355 cm^{-1} [128, 129]. A peak at around 1550 cm^{-1} has been commonly attributed to the presence of graphite i.e., sp^2 hybridization. This is not an accurate assignment, since it has been argued to arise from diamond-like carbon (DLC), which may not be graphitic in nature [130]. In addition, films with nanocrystallites show a broad peak centered at $\approx$1133 cm^{-1} [131]. Despite some objections, the quality of deposited diamond is generally judged from the relative intensity of the peaks at 1332 and 1550 cm^{-1} [130]. Robins et al. has published a comprehensive analysis of various attributes to the shape of Raman Spectra [132].

Scanning Electron Microscope (SEM)

One of the most commonly analytical tool for studying the morphology and visual analysis of diamond films is scanning electron microscope (SEM). Since the CVD diamond films generally have micron or sub-micron size grains, optical microscopes which has an upper limit of magnification of about 2000 *times* and, at that magnification, a small depth of field, cannot resolve them effectively. The high resolution of SEM, is capable to resolve objects in dimensions down to 100 $\mathring{A}$. SEM micrographs of the film surface provides details of the surface morphology, film uniformity, voids, cracks, selectivity of patterns and crystal orientations, etc. In this work SEM will be also used to determine the thickness of diamond film by inspecting the film's cross section.

2.5.5 Doping of Diamond

Natural semiconducting diamond was discovered in 1952 [133]. This discovery revealed its outstanding electronic properties in addition to its already known physical properties. Semiconducting type II-b diamond is lightly p-doped. It has been shown that the acceptor center is substitutional boron. Nitrogen also is a common impurity in diamond and it has been suggested that nitrogen is present on isolated substitutional lattice sites and is known to be the donor center in semiconducting natural diamond [55].

Many researchers have attempted to realize semiconductive diamond by doping impurity atoms such as boron and phosphorus and lithium [134, 135, 136]. The p-type diamond doped with boron atoms is more easily obtained than the n-type diamond. Because of the low diffusivity of most impurities (dopants) in natural diamond, the diffusion doping technique that is commonly used to dope semiconductors can not be used for diamond. Doping by ion implantation is the only technique to introduce

impurities in natural diamond. Ion implantation technique was first investigated by workers in the Soviet Union [134, 135, 136]. Lithium (Li^+), boron (B^+) and phosphorus (P^+) ions have been used with varying degrees of success. Li^+ and P^+ ions produced n-type layers. However, post-implant annealing of these n-type layers at 1200 °C resulted in an increase in sheet resistance, but the layer remained n-type. The alkali metals of smaller atomic size may be good n-type dopants since it is known from nuclear reaction studies that lithium occupies an interstitial site in the diamond lattice and can therefore donate an electron to the conduction band [134, 135, 136]. In 1982, Prins [137] produced n-type regions in natural p-type diamond. These n-type regions were induced by implantation of carbon ions into diamond in order to fabricate n-p-n transistor[137]. Experiments have shown that the conductivity is dependent on the ion dose, dose rate, and the temperature during implantation. However, the lack of large area single crystal semiconducting diamond and the high cost of fabrication combined with the difficulty in controlling dopants limit the applicability of these devices in microelectronics.

Synthetic semiconducting diamond was successfully manufactured in 1962 by researchers at General Electric [138, 139]. They reported synthetic p-type semiconducting diamond from a mixture of graphite and catalyst metals (Ni, Fe, etc.) and small amounts of B, Be, and Al using high pressure high temperatures process. Electrical transport measurements on B, Al, and Be doped synthetic diamond, [48] showed p-type conductivity with impurity activation energies of 0.17-0.18, 0.32 and 0.2-0.36 eV, respectively. Similar measurements by Wilson [56] in the temperature range of 88 K to 293 K on B doped specimens yielded nearly 30 discrete activation energies ranging between 2.9 and 87 meV. These data were interpreted as evidence of impurity conduction or hopping transport which is commonly observed in heavily doped and highly compensated semiconductors at low temperatures [58,59,165]. In both natural and synthetic semiconducting diamonds acceptors are typically compensated by deep

nitrogen donors with activation energy of about 4 eV above the valence band. The acceptor activation energy for boron in natural semiconductor diamonds has been recognized at 0.37eV [134, 135, 136]. However, HPHT method is costly and is not suitable for production a thin film diamond. Furthermore, the metal catalyst creates metal inclusions and small voids. Therefore, synthetic semiconducting diamond is not suitable in semiconductor devices.

The latest developments in the growth of doped and undoped diamond films on diamond and non-diamond substrate by chemical vapor deposition CVD has led to the current interest in the use of diamond for semiconducting devices [1, 93, 99, 140]. This CVD method enhanced the possibility of semiconducting diamond devices with extraordinary characteristics. Doping during growth (*in-situ*) from gas phase and solid sources using the CVD method has been demonstrated. Semiconductive n-type diamond was produced with phosphorus pentoxide (P_2O_5) as the doping sources [141, 142]. The n-type films demonstrated a high resistance. The problem of producing (*in-situ*) n-type layer with very low resistance has not been solved at the present time.

The production of device quality diamond requires techniques for introducing controlled amounts of dopant impurities. So far, boron is the only dopant successfully used to fabricate thin film diamond based devices [140] using CVD techniques. It has been known that the boron atoms are present on substitutional sites which creates acceptor centers with activation energy of 0.37 eV [143]. Typically, 0.1% of the acceptors are ionized at room temperature. In most of the experiments boron doping was achieved by admixing relatively toxic diborane B_2H_6 to methane and hydrogen during film growth process [141]. A nontoxic saturated solution of boron trioxide B_2O_3 powder in CH_3OH mixed with acetone was also used [144]. A high purity boron powder was also used during diamond film growth in CVD deposition chamber [145]. During the growth process boron is etched away by the hydrogen plasma to

form boron hybrids. The boron hybrids enter the plasma and boron is incorporated in the diamond film during the growth process. Boron doping can also be performed by lowering a boron rod into the plasma during the growth process. Homoepitaxial semiconducting diamond films have been grown selectively on natural diamond substrate (type Ia) using sputtered SiO_2 as a masking layer [69, 145, 146]. Polycrystalline semiconducting diamond films have been grown on many substrates.

2.5.6 Patterning

Because of diamond's extreme resistance to chemical attack, it is very difficult to pattern using chemical etch. The geometry and physical dimensions are some of the prime parameters in determining the functionality of any electronic and micromechanical devices. Dry etching and selective nucleation techniques were studied by many investigators [59, 61, 119, 147, 148, 149, 150, 151, 152, 153, 154, 155].

Several techniques such as ion beam etching, reactive ion etching, and plasma assisted etching and electron cyclotron resonance (ECR)-assisted etching for the dry etching of diamond have been reported [151, 152, 156].

T. J. Whetten, et al. [151] reported that they etched single crystal diamonds by exposing the (100) face to argon and oxygen ion beams. Etch steps were made in the diamond surface by masking a region of the diamond with a silicon chip. Ion energy of 500 eV, 750 eV, and 1000 eV was used. No etch rate was reported [151].

Reactive ion etching (RIE) with oxygen was also investigated by N. N. Efremow, et al [152]. Etch rates on the order of 20 nm/min and poor etch selectivity between the masking material Ni or Cr and the single crystal diamond (type IIa) was reported [152]. However, in a later experiment, an ion-beam-assisted etching system was used by the same group. A beam of 2 keV Xe^+ ions with a flux density of 1 mA/cm^2, and a reactive gas flux of nitrogen dioxide (NO_2) were used, etching rate of 200 nm/min

was obtained with an etching rate ratio of 20 between the diamond and an aluminum mask.

The use of an electron cyclotron resonance plasma source for oxygen etching of type IIa (100) natural and synthetic diamond was also investigated by Beetz et al [153]. Etch rates of 290 $\AA$/min were obtained. The metals used for masking the diamond were gold (1 μm) and titanium (1000 $\AA$).

K. Tankala and T. Debroy investigated the etching of HFCVD diamond films in air, nitrous oxide and argon using an oxidation method [154]. The weight of the sample was measured before and after oxidizing the sample in a heated furnace. They reported that the oxidation of the diamond films starts at 773 °K in air and at 873 °K in N_2O. The etch or oxidation rates for the HFCVD films were 600 $\AA$/min and 280 $\AA$/min in air and N_2O, respectively. Oxidation of natural diamond crystals starts at about 900 °K in air. Dry etching was also performed at room temperature using argon plasma etching which was generated by capacitively coupling two electrodes energized by a 13.56 MHz radio frequency generator inside a vacuum chamber. Etching rate of 250 $\AA$/min was reported (25 watt radio frequency power and pressure of 3.0 torr were used).

An alternative approach to etching an existing film is to actually grow a patterned film through selective nucleation. Different methods of patterning have been reported on the selective deposition of diamond [61, 119, 147, 148, 157, 158].

In the approach reported by Hirabayashi et al. [157], the selective growth of diamond was achieved by using an Ar^+ ion beam with vertical incidence on a pretreated silicon substrate which was patterned with resist. They explained that, Ar^+ beam was used to remove the pretreated surface layer which was not covered with photoresist. Ma et al. [158], in a similar attempt, obtained selective nucleation of diamond particles by using Ar beam irradiation on a pretreated substrate having small SiO_2 dots on silicon.

Davidson et al. [147] reported that polycrystalline diamond films were selectively deposited on a pretreated silicon surface. In their approach, the polish side of silicon wafer was manually scratched using diamond paste. Silicon nitride was then deposited after cleaning the wafer. The silicon nitride was then photolithographically patterned and plasma etched. An oxide layer of 1.2 μm in thickness was then thermally grown on the exposed area of silicon. The silicon nitride was then completely etched in boiling phosphoric acid, washed with D.I. water, rinsed with acetone, methanol, and nitrogen dried. The diamond was then deposited on the exposed pretreated areas.

Recently, a novel technique to selectively deposit high quality polycrystalline diamond films has been developed at Michigan State University [119]. The selective nucleation was achieved by patterning photoresist, which was premixed with fine diamond powder (0.1-0.2 μm), using standard photolithographic process. The nucleation density, uniformity, and smoothness of the resulting diamond films were optimized by controlling the photoresist thickness through the careful choice of spinning time and speed. In this method, fine diamond particles acted as seeds for the growth of diamond only in the patterned areas.

Comparing this technique, to the previously described ones, diamond powder photoresist is the simplest one. It may be employed on nearly all substrates found in electronic device manufacturing. This method is easily incorporable in the existing integrated circuit fabrication technology. It only requires one mask step process, The method described by Davidson et al. required two or more mask process steps in addition to scratching the substrates.

2.5.7 Highly Oriented Films

The growth of highly oriented or single crystal diamond films on non-diamond substrates (heteroepitaxy) is a necessity for most practical electronic devices. To date, most semiconducting diamond films grown on non-diamond substrate are polycrys-

talline.

The growth of heteroepitaxy is believed to be dependent on matching the lattice parameter of diamond and/or the thermal coefficient of expansion to the deposited substrate. The effects of varying the deposition parameters controlling both the gas phase chemistry and the surface chemistry are other factors. Substrate orientation and process conditions are also important factors.

Heteroepitaxy has been accomplished on Ni, C-BN , SiC [159, 160] and most recently Si single crystals[161]. The epitaxial films grown on c-BN single crystals were highly oriented although the size and quality of the substrate material has limited the exploitation and further development of this epitaxial approach [159].

Geis et al. [65] have demonstrated a technique named "artificial epitaxy" or "MOSAIC"to achieve large area single crystal diamond on silicon substrate. In that approach, diamond seed crystals were aligned by placing them in inverted pyramid shaped structures micromachined on a silicon substrate surface. During diamond deposition, the growth of each diamond particle proceeds laterally as well as vertically, joining with the other particles in close proximity, forming a continuous layer of diamond.

As explained by Van der Drift [162], textured growth can be understood as a result of growth competition between differently oriented grains. The basic parameter which determines the film texture is the direction of fastest growth. The growth of polycrystalline film starts from distinct nucleation sites. As individual randomly oriented nuclei grow larger, their diameters equal the average distance between the nucleation sites and they begin to form a continuous film. With increasing film thickness, more and more grains are over grown and buried by adjacent grains. Only those crystals with the direction of fastest growth perpendicular to the surface will survive. For an initial distribution of randomly oriented diamond nuclei, the resulting film-texture will be a function of the relative growth rate parameter (α) which is

described as [161]

$$\alpha = \sqrt{3}\,\frac{V_{100}}{V_{111}} \tag{2.23}$$

where V_{100} and V_{111} are the growth rates on the {100} and {111} faces respectively. In order to obtain < 100 >-textured diamond films, the direction of fastest growth must be < 100 >, that is $3.0 < \alpha < 2.6$ [161].

Most recently, it was demonstrated by Stoner et al. [161] using microwave plasma enhanced chemical vapor deposition system, that under certain growth conditions the growth competition between differently oriented grains can result in the formation of strongly < 100 >- textured diamond films with smooth {100}-faceted surfaces. In that approach, textured films were nucleated by a two step process that involved the conversion of the silicon surface to an epitaxial SiC layer, followed by bias-enhanced nucleation (BEN) process.

Boron-doped layers were selectively deposited onto the surface of these oriented films. Room temperature hole mobilities between 135 and 278 cm^2/V-s were measured, this indicated a 3 to 5 times improvement in hole mobility over polycrystalline diamond films grown under similar conditions.

2.6 Diamond Devices

From an electronic perspective, diamond should be a good candidate for high temperatures and harsh radiation environments due to its wide band gap, high speed due to its carrier mobility, and high power due to its high thermal conductivity and breakdown voltage. Most common semiconductors require reverse biased junctions in order to avoid leakage current. In contrast, a very high electric field may be applied across a diamond device without producing significant leakage current.

In 1982, Prins [137] was able to fabricate a bipolar transistor behavior. He produced n-type regions in natural p-type diamond. These n-type regions were induced

by implantation of carbon ions into diamond. However, very low current gain was obtained and the conductivity disappeared after annealing at 700-800 °C,

Point-contact transistors and Schottky diodes were formed on a synthetic boron doped diamond [69]. The transistors exhibited power gain at 510 °C, and the Schottky diodes were operational at 700 °C. Field effect transistors (FET's) fabricated from ion-implanted single-crystal diamonds (SCDs) have shown excellent characteristics exhibiting both current saturation and active channel pinch-off [163, 164]. Also, FET's were fabricated from *in-situ* doped homoepitaxially grown on synthetic single crystal substrates [146, 156, 163]. Operation of polycrystalline diamond FET's at temperature up to 285 °C and drain-to-source voltage of up to 100 V have been demonstrated [164, 165]. The operation of diamond-based depletion type MOSFET's has been achieved in the 300-400 °C temperature range [166]. Typically, most of the above mentioned devices were achieved by using homoepitaxy on natural or synthetic diamond substrates. These devices were not commercially produced, because of high cost and limited size.

2.7 Diamond Sensors

Diamond as a sensor material has been studied by many investigators, especially for the application as radiation and high temperature sensors [125, 167, 168, 169, 170].

The intrinsic radiation hardness of a semiconductor relates primarily to its chemical bonding energy and the manner in which radiation induced lattice dislocations produced energy states within the forbidden band. The chemical bonding energy of diamond is the strongest of all semiconductors and therefore the most immune to radiation damage. Photoconductive UV and ionizing radiation detectors have been used for over 70 and 50 years, respectively. Due to the large band gap, high resistivity 10^{14} ohm-cm, high carrier mobility and the large saturated carrier velocity of insu-

lating diamond, very high electric field may be applied across diamond film without producing significant leakage current. The high carrier saturation velocity permits the high speed and high sensitivity operation of diamond detectors. Any radiation that generates free carriers in the diamond can be detected. These radiations include electromagnetic radiation with an energy of greater than 5.5 eV. This incorporates UV, X-rays and γ rays. High energy particle radiation such as α particles, electrons, neutrons, and other exotic particles can also be detected.

A diamond radiation detector is a simple two-terminal metal-insulator-metal (MIM) structure. The generation of free carrier is usually detected by an external circuit. The motion of the free charges is driven by an externally applied electric field. The generation rate is proportional to the intensity of the absorbed radiation divided by the average ionization energy ϵ, that forms mobile electron-hole (e-h) pair. The figure of merit for radiation detectors is the average distance a carrier moves (distance the electron-hole pairs drift apart). This is expressed as the product of the carrier mobility μ, the lifetime τ of the mobile charges, and the applied electric field E and is given by [168]:

$$d = \mu \tau E \tag{2.24}$$

The lifetime may be limited by material defects or device geometry. For a given electric field, d is a measure of the sensitivity of the material to radiation detection.

Kania *et al.* [168] have studied the radiation detector properties of polycrystalline CVD diamond films by two methods: (1) UV transient photoconductivity (PC) and (2) charge collection measurements using ionizing radiation. The collection distance d was measured between two electrodes on the surface of the sample. They observed that d increases with thickness. According to their explanation, this might be due to the reduction in the defect density of the material as it grows thicker. It has been concluded by the authors that, the current state of the art in CVD diamond films

gives $d \approx 20$ μm, which is equal to that of type-IIa single crystal diamond detectors.

The diamond thermistor is the first application of diamond films in the field of sensors. The thermistor is a passive device and a very simple one. The thermal properties of p-type semiconducting diamond have been reported by many investigators [125, 169, 170, 171].

Thermistors fabricated from single crystal diamond type IIb have been reported [172]. However, economic considerations have rendered these thermistors unacceptable for most applications. The first synthetic diamond thermistors were produced by General Electric in 1969 [173]. These thermistors were doped by boron during synthesis. They observed that the p-type synthetic diamond thermistors are superior to natural diamonds, since they did not exhibit the resistivity increase with temperature between 700 and 800 K. Because, of high production cost and limited shape and size, none of these thermistors were produced commercially, Thermistors made of synthetic semiconducting diamonds were also reported by other investigators [169]. These thermistors were used as the level meter for liquids which was corrosive such as acids or alkalis and were shown to operate at temperatures from -100 to 400 °C [169].

Thermistor made of CVD diamond films have been reported by [125, 170, 174]. Fujimori and Nakahata [170] have claimed the first fabrication of a polycrystalline and homoepitaxial CVD diamond thermistors. The diamond films were deposited by microwave plasma CVD. Undoped and boron-doped resistive elements were deposited on silicon nitride substrates. The ohmic metal contacts were fabricated using Ti/Mo/Au multilayers. The use of Mo as a barrier layer was introduced to stop alloying between the gold and titanium at elevated temperatures. Silicon dioxide was used as a passivation layer. Nickel wire was used to be the lead wire and brazed to the electrodes by refractory silver paste. Highest temperature of diamond thermistor was 600 °C. The device made by non-doped film is the most sensitive to temperature.

The sensitivity decreases with increasing B/C ratio. The response time of thermistor is compared by 63% change of applied temperature difference. Using oil bath, the response time was measured to be 1.4 sec. For homoepitaxial film the response time was observed to be 0.15 sec. It was observed that at 500 °C the resistance of one thermistor increased by 5% after 100 h in air.

P-type CVD polycrystalline diamond thermistors have been also fabricated at Michigan State University [120, 125]. The diamond films were deposited using HFCVD reactor. The resistivity of poly-diamond film thermistors, measured as a function of temperature (77 - 1273 K) for three doping levels, is shown in Fig. 2.8 [125]. All the samples were annealed at temperatures of 600 °C and 1000 °C for 35 and 8 minutes, respectively, at a pressure of 10^{-7} torr before taking measurements for temperature response of resistivity. The high sensitivity is achieved at low boron concentration. All devices exhibit a negative temperature coefficient (NTC) over the entire temperature range. This is unique to poly-diamond films, because other conventional semiconductors display NTC only in freeze-out and intrinsic regions and positive temperature coefficient (PTC) in extrinsic region. The sensitivity of a temperature sensor is characterized by its temperature coefficient $\alpha = \frac{1}{\rho}\frac{\delta\rho}{\delta T}$ where ρ is the resistivity of the sensor at temperature T. For the samples shown in Fig. 2.8, α is in the range of 0.005 - 0.02 K^{-1} over most of the temperature range. The response time was in the range of 290ns-25μs which is three to four order of magnitude smaller than previously reported results [170]. In addition to the reduction of the response time, the temperature range was also extended to 1000 °C comparing to 600 °C reported earlier [170]. The parameters of these highly sensitive devices are characterized by a high stability because the diffusion of electrically active impurities in diamond is very slight in the temperature range. The responsiveness of a thermistor is determined by the thermal conductivity (high) and the specific heat (low) of diamond. Diamond thermistor made by CVD technique are superior to that of any other material in

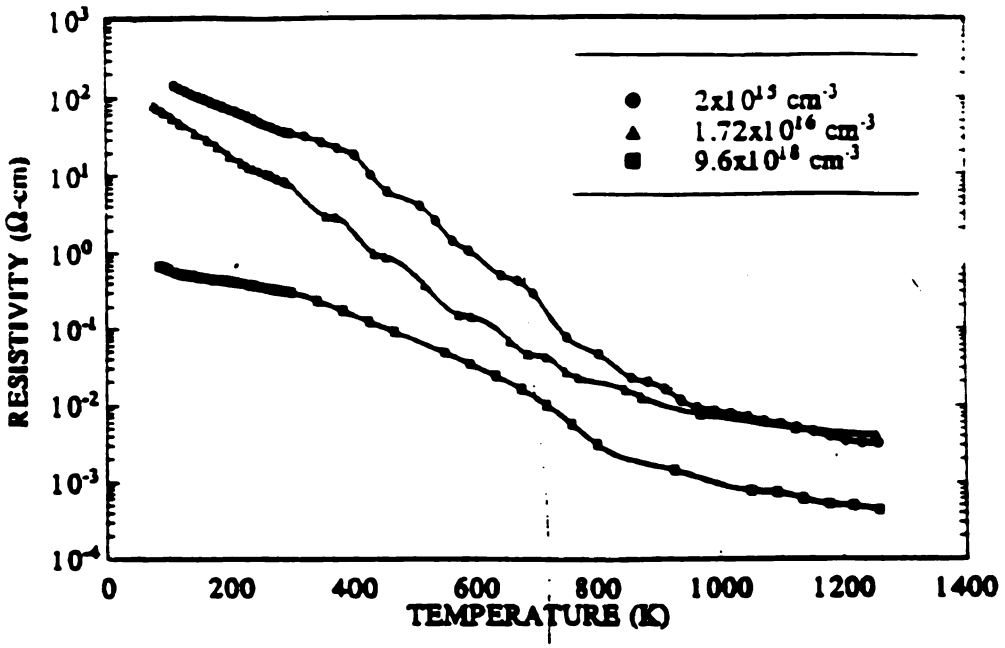

Figure 2.8. Resistivity of poly-diamond film thermistors, measured as a function of temperature (77 - 1273 K) for three doping levels.

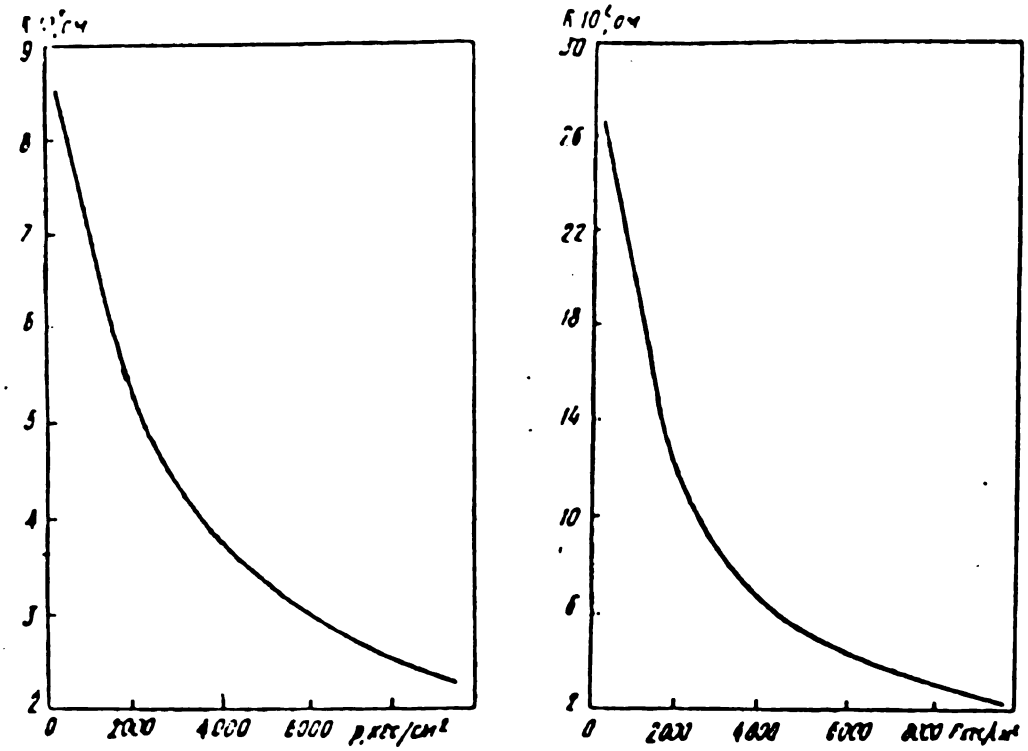

a b

Figure 2.9. Stress dependences of resistance of the semiconducting synthetic diamond doped with boron (p-type) in the (a) <100> and (b) <111> directions (original plots).

terms of temperature range, speed, stability and sensitivity.

The piezoresistive effect in CVD diamond was not investigated before our work. However, there was some early Russian work done in the piezoresistance of the HPHT synthetic diamond [175, 176]. The samples were p-type synthetic diamond doped with boron. The samples were orderly shaped as cubooctahedrals with side facet 0.5-1mm. Before measurement the samples were subjected to chemical heat treatment and following annealing in vacuum at temperature in the range of 800-900 °C for 30 minutes. In their experiment, a uniaxial (compression) stress was applied through a small sphere with different dimensions. Measurement of the stress was calculated from the contact area between the surface of the sample and the sphere. Figure 2.9 shows the resistance as a function of stress in (a) <100> direction and (b) <111> direction. For both directions of stress the resistance decreases drastically within the range of pressures 0 to 2000 $kg.cm^{-2}$. With the increase of pressure the curve slope decreases and the resistance tends to saturation. It is seen from their results that semiconducting diamond is extremely sensitive to the change of pressure (uniaxial stress). Therefore, diamond piezoresistive sensors could be a good candidate for micromechanical sensor applications in harsh environments. In this work we estimated their gauge factor from their curves. The results are given in Chapter 6.

2.8 Summary

Silicon-based and diamond-based sensors were discussed in this chapter. Chemical vapor deposition, nucleation, patterning and doping methods of diamond film were also presented in this chapter.

CHAPTER 3

Diamond Film Technology

3.1 Introduction

In this chapter, film preparation by the HFCVD deposition system will be explained. The description of the diamond powder photoresist (DPPR) nucleation method will be presented. Raman spectroscopic and SEM techniques will be used to characterize the diamond films. Pure boron powder was used as a doping source for *in-situ* doping. Two new approaches have been developed to improve the doping profile across the surface of the sample.

3.2 The HFCVD Deposition System

3.2.1 Description of the System

The simplest and most widely used method for growing the diamond films is the HFCVD technique. This technique was first used by Matsumoto et al [93]. In this research, the diamond films were deposited using the HFCVD technique. The system was originally designed and built at Ford Scientific Research Lab. The improvements are mainly in terms of control and stability of growth parameters, doping and flexi-

bility of operation.

Figure 3.1 shows a schematic diagram of the deposition system. The deposition chamber is a 6″ hollow cube made of stainless steel provided with openings for flanges on each face. Visual access during deposition to the substrate and various components inside the chamber has been provided by a glass window. Before the deposition, the reaction chamber is evacuated by a mechanical pump to reduce residual gases. Nitrogen is used to purge and backfill the chamber. Pressure measurement within the vacuum chamber is performed by a baratron pressure transducer. This transducer supplies suitable signals through a controller to a down stream valve which maintains the chamber pressure to be within 0.1% of the preset value up to 100 torr. Up to three different gases may be used simultaneously. The source gases were H_2, CO, and CH_4 or C_2H_2. The flow rate of all three gases is precisely adjustable independently by three mass flow controllers. The flow controller for H_2, CO, and CH_4 or C_2H_2 has maximum operating flows of 100, 50 and 1 sccm respectively. The gas output of each mass flow controller is mixed simultaneously into a single gas channel which feeds the processing chamber. The gas is uniformly distributed above the filament.

The filament is a horizontal array of seven 2″ long parallel Ta wires (0.005″ diameter, 99.9% pure) spaced at 8 mm. A sample with surface area of 2.5x6 cm^2 can be uniformly coated with diamond using this arrangement. The temperature of the filament is monitored by a two wavelength pyrometer and controlled automatically to within ± 2 °C by a controller using an SCR based power supply. The filament typically draws 25-30 A current at 25-35 VAC at nominal temperature of 2400 °C. The filament is placed within ≈ 1 cm of the substrate surface to minimize thermalization and radical recombinations. However, radiation heating can produce excessive substrate temperatures leading to nonuniformity and even graphitic deposits [177]. In our system, the substrate temperature caused by the heat radiation from the filament is about 725 ±1 °C.

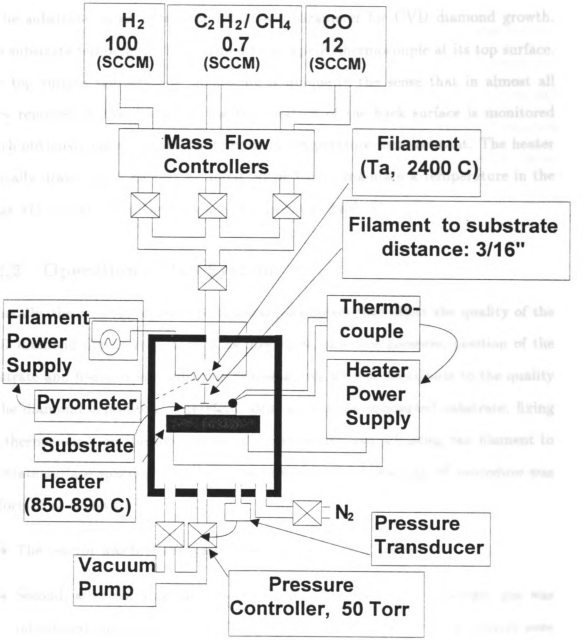

Figure 3.1. Schematic diagram of the deposition system.

The substrates are placed on a $1\frac{3}{4}''$ diameter Boralectric heating plate (made of BN with graphite heating element embedded inside) below the filament. The temperature of the substrate, is an extremely important parameter for CVD diamond growth. The substrate temperature is measured by a type K thermocouple at its top surface. The top surface temperature monitoring is unique in the sense that in almost all cases reported in the literature, the temperature of the back surface is monitored which obviously causes an indefinite error in temperature measurement. The heater typically draws 5-8 A current at about 50-70 Vac to maintain a temperature in the range 875 to 890 ° C in the presence of filament at 2400 °C.

3.2.2 Operation of the System

Generally, the number of the experimental parameters that affect the quality of the CVD diamond film is very large. Gas flow rates, chamber pressure, position of the substrate and filament and substrate temperatures all may contribute to the quality of the diamond deposition. Therefore, after setting the pretreated substrate, fixing the thermocouple on the top surface of the substrate and adjusting the filament to substrate surface spacing to (3/16)", the turning on and shutting off procedure was performed as follows.

- The reactor was first evacuated down to less than 10 mtorr.
- Second, after reaching the pressure range (<10 mtorr), the hydrogen gas was introduced into the chamber. Then, the filament and heater temperatures were brought up slowly in hydrogen environment (>20 torr) in the respective order manually to their desired temperatures. It is important to avoid any damage to these elements or substrates by heavy in rush current or sudden temperature changes especially beyond the desired temperature.

- After two or three minutes of reaching the deposition temperature (typically 890 °C), the carbon sources were switched on.

- Because of the presence of a very thin conducting carboneous layer on the surface of CVD diamond film, a special procedure to terminate the deposition process was followed. In that, only carbon containing gases are shut down and all other parameters are left unchanged including hydrogen gas for 3 minutes before the termination of the deposition process. In this period hydrogen, being the preferential etchant, is assumed to etch away the non-diamond layer.

3.3 The Nucleation Method

Generally, the nucleation density for diamond growth on non-diamond substrates is 10^4 cm^{-2} [119]. Enhancing the number of nucleation sites on the wafer surface is very important for the development of a pinhole-free film in a reasonable deposition time. Different nucleation methods have been developed by many investigators which were reviewed in chapter 2 [106, 116, 117, 118, 119]. In this research, the diamond powder photoresist (DPPR) is used to enhance the nucleation density [119]. This method is highly compatible with standard integrated circuit (IC) processes. In this research DPPR was prepared according to the following steps.

- First the diamond powder (particle size 0.1 to 0.2 μm) was initially dried at temperature of $\approx$ 60°C for 2 hours on a heating plate.

- Second, the dried diamond powder was mixed in the photoresist thinner and stirred magnetically for 15 minutes followed by 15 minutes of ultrasonic agitation. The magnetic stirring and ultrasonic agitation were repeated for three cycles.

- Finally, the photoresist was added to the suspension and further stirred and ultrasonically agitated for 15 minutes each. Again the magnetic stirring and ultrasonic agitation were repeated for three cycles.

Table 3.1. Sample preparation for nucleation study

Group I.D.	Diamond powder density in DPPR (mg/ml)	Spin speed (RPM)	Number of DPPR layers	Nucleation density (cm^{-2})
G-1	1.98		1	
G-1a		3000		2.7×10^7
G-1b		2000		3.1×10^7
G-2	2.27		1	
G-2a		4000		7.5×10^7
G-2b		2000		8.7×10^7
G-3	5.68		1	
G-3a		3000		1.56×10^8
G-3b		3000		
G-3c		2000		1.62×10^8
G-4	2.27		2	
G-4a		2000		
G-4b		3000		1.75×10^8
G-4c		3000		

The substrate is a 4″ (100) single-crystalline silicon wafer or thermally oxidized silicon or deposited SiO_2 layer on a silicon wafer. Before spreading the DPPR on the Si wafer, the wafer was cleaned by piranha solution (H_2SO_4:H_2O_2, 1:1) for 30 minutes, then rinsed in the DI water and dried with nitrogen gun. After that the wafer was coated with a photoresist adhesion promoter (HMDS). The HMDS was applied by evaporation method in a special furnace at 150 °C for 30 minutes. During CVD diamond deposition, the photoresist evaporates in initial stages and the diamond particles act as nucleation sites for the diamond growth.

Four different groups of samples were prepared. These samples are grouped according to the quantity of diamond powder mixed in the photoresist and the number of DPPR layers used to coat the substrate. The samples and their parameters are listed in Table 3.1. The spin time for all sample was 20 second. The deposited diamond films were inspected by SEM. SEM micrographs of the diamond films deposited on the substrates pre-treated by this method are shown in Figs. 3.2, 3.3 and 3.4.

Figure 3.2 shows SEM micrograph for sample G-1a from Group G-1. The film was not continuous after 6 hours of deposition time. The nucleation density was calculated by counting the number of diamond particles in a square area in the early stage of deposition periode. The result is shown in Table 3.1. It was also observed that the nucleation density increased by decreasing the spin speed of the substrate during photoresist coating. Approximately, 10 hours of deposition time was needed to have a continuous film.

In order to obtain a continuous film for less than 10 hours of deposition time the density of diamond powder was increased from 1.98 mg/ml to 5.68 mg/ml. The result of this approach is shown in Figure 3.3. The SEM micrograph is for sample G-3a (7 hours of deposition time). The nucleation density of this sample is an order of magnitude higher than sample from groups G-1 and G-2. Slowing the spin speed to 2000 RPM resulted in a large amount of cluster particles and nonuniformity of the film with very little increase of nucleation density (see Table 3.1). A continuous film was obtained for about 7 hours of deposition time.

In Group G-4 samples, two layers of DPPR were spun on the substrate. The DPPR used for this group of samples, was from the same mixture of group G-2 (2.27 mg/ml). After coating the first layer, the substrate was loaded into the furnace in order to cure the first layer (Softbake, 90 °C, 20 min). As shown by SEM in Figure 3.4, the film is continuous for 7.5 hour of deposition time.

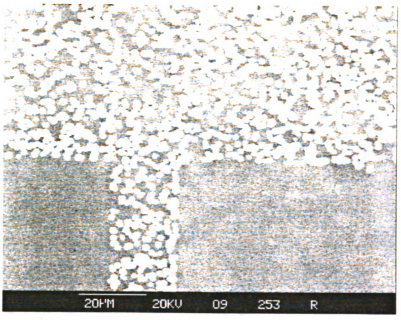

Figure 3.2. SEM micrograph for sample G-1a.

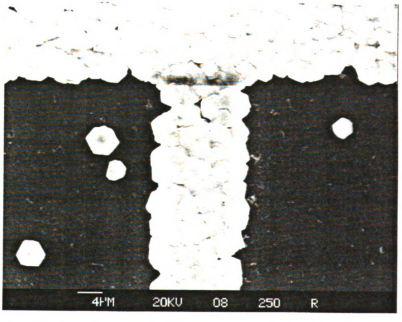

Figure 3.3. SEM micrograph for sample G-3a.

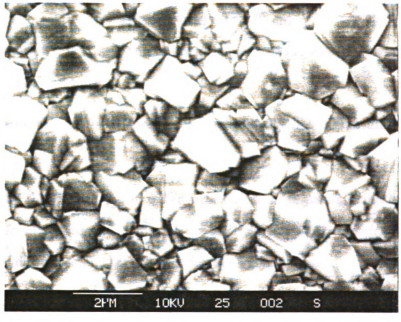

Figure 3.4. SEM micrograph for sample G-4b.

It is visible from the SEM micrographs, especially Figure 3.3 and Figure 3.4, that the film has fairly uniform grain size ($\approx$ 1 to 2 μm). In fact, by utilizing the pretreatment of the last two approaches (G-3 and G-4), it was possible to obtain a complete surface coverage after roughly seven hours of deposition time with deposition rate in the range of 0.25 0.30 μm/hour. Raman spectra of the diamond films deposited on the silicon substrate show a strong peak at 1332 cm^{-1}.

In conclusion of this study, the following observations were recorded during SEM inspection of diamond films.

- Higher spin rate leads to lower nucleation density but higher uniformity (Group G-2).
- Spreading the DPPR on the wafer after half hour of preparation has led to more non-uniformity and clustering. Using DPPR suspension which is rested for two hours leads to less clusters than a freshly agitated one.
- A larger quantity of diamond powder in a given solution of photoresist and thinner gives higher nucleation density (Group G-3). Using two layers of DPPR has also led to higher nucleation density (Group G-4).

This experiment provided an optimum quantities of diamond powder, photoresist and photo-resist thinner in DPPR suspension which leads to a continuous diamond films with deposition time for almost 7 hours.

Surface Roughness

In order to quantify film roughness, a Tencor P-2 surface profiler was used. Fig. 3.5(a) shows the surface roughness of sample deposited for 9 hours. The maximum surface roughness is about 1450 $\AA$. The film thickness is about 2.1 μm. Fig. 3.5(b) shows the surface roughness of sample deposited for 20 hours. The thickness of this film is 5.8 μm and the maximum surface roughness is about 4000 $\AA$.

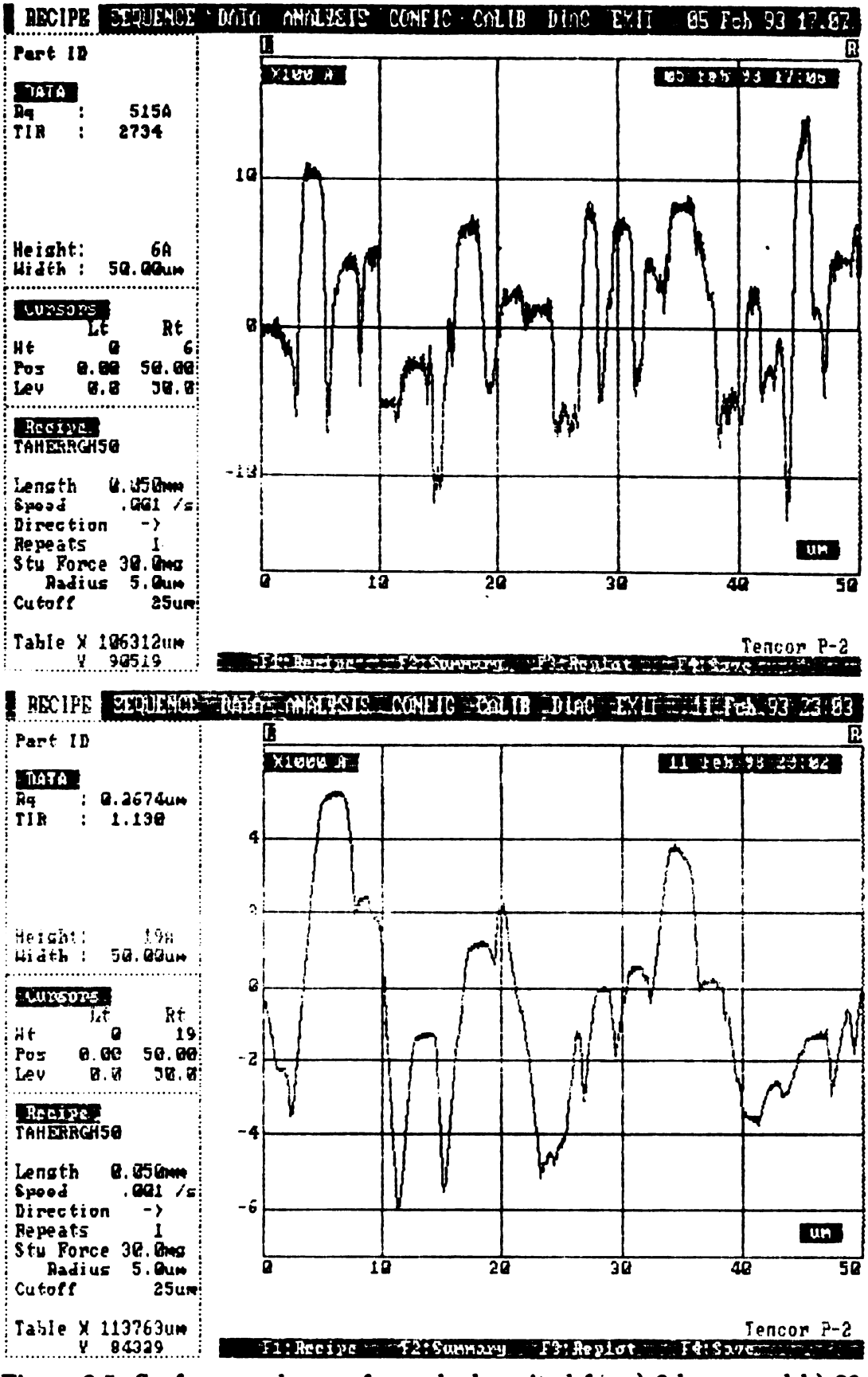

Figure 3.5. Surface roughness of sample deposited for a) 9 hours and b) 20 hours.

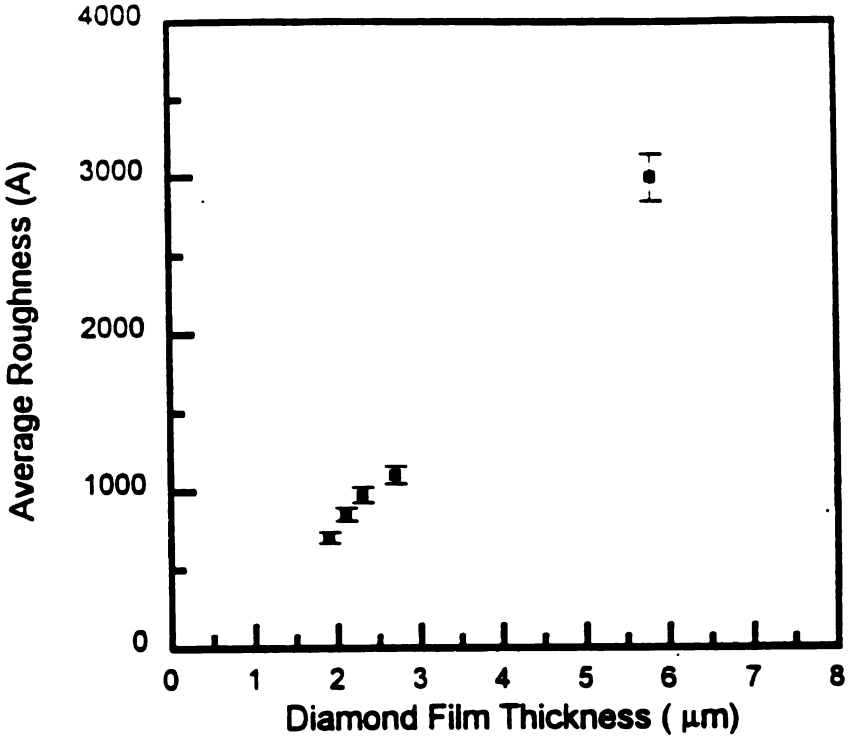

Figure 3.6. Effect of diamond film thickness on the surface roughness.

Generally, as the film thickness grows (longer deposition time) the surface roughness was also observed to grow. Figure 3.6 shows the effect of diamond film thickness on the surface roughness. A larger surface roughness of the thicker films results from the larger grains on the surface.

3.4 Diamond Film Patterning

Many of the potential microelectronic and microsensor applications require patterned thin films of polycrystalline diamond. Etching of diamond film by dry etching techniques has been investigated [151, 152, 153]. The non-uniformity of the etch, the low etch rates and poor etch selectivity between mask materials and the diamond have limited the application of the dry etching techniques [59].

Selective deposition of polycrystalline diamond can be achieved if the two regions on the substrate have nucleation densities differing by several orders of magnitude. Many attempts employing varying methods of patterning of diamond films on non-diamond substrates through selective nucleation have been reported [61, 119, 147, 148, 157, 158]. Many of these techniques were described earlier in section 2.4 chapter 2. Most of these techniques cause surface damage.

Recently, a novel process has been developed to selectively deposit high quality polycrystalline diamond films [119]. This has been achieved by patterning photoresist, which was premixed with fine diamond powder (0.1-0.2 μm), using standard photolithographic process. The preparation of this solution was described in section 3.4 chapter 3. This technique not only preserves the high quality of substrate surface but is also compatible with the existing integrated circuit fabrication technology. Consequently, this technique will be adopted for this research.

Double-Layer Patterning

In this work, as the substrate is a 4″ (100) silicon wafer and minimum feature size is 5 μm, an improvement of this technique was suggested and studied. A double layer structure was used to enhance the patterning. Three different approaches were developed during this work. Fig. 3.7 shows the schematic of 3 configurations used for double-layer patterning. Mask 1 of the microchip was used in this study.

In the first configuration (Config-1), the samples were patterned by first coat the oxidized wafer with layers of photoresist (PR)(AZ1470) and a double layer of DPPR. The PR layer helps removes residual diamond particles during the spray-developing. After patterning the photoresist layers and prior to the diamond deposition, the sample was treated by BHF for 2 minutes via ultrasonic treatment. Fig. 3.8 shows SEM micrograph for diamond microchip prepared by Config-1, It is clear that some scattered diamond particles were grown on the undesired areas. However, These particles did not form a continuous film as shown in the Figure. The nucleation density in the undesired area was $\approx$ 1.1 x10^5/cm^2 which is very small comparing to the nucleation density in the desired area which was $\approx$ 1.75 x10^8/cm^2.

In the second configuration (Config-2) a layer of undoped polycrystalline silicon was deposited on the top of the oxidized wafer. The polycrystalline silicon layer was deposited in a LPCVD furnace at a SiH_4 pressure of 320 mT and a temperature of $\approx$ 600 °C. Polycrystalline silicon layers with different thicknesses (2000 $\AA$, 1 μm, 2 μm and 3 μm) were used for this study. Two layers of DPPR were then dispensed on the poly-Si/SiO_2/Si wafers. After patterning the photoresist, the wafer was then loaded into a plasma reactor to etch the exposed polysilicon areas. The polysilicon was etched by using SF_6 and Freon 115 (C_2F_6) gases. The gas flow rates was 50 sccm for each gas. The power was 110 watt and the over all pressure in the reactor was 150 torr. The etch rate of the polysilicon was $\approx$ 700 to 900 $\AA$ per minutes. After etching

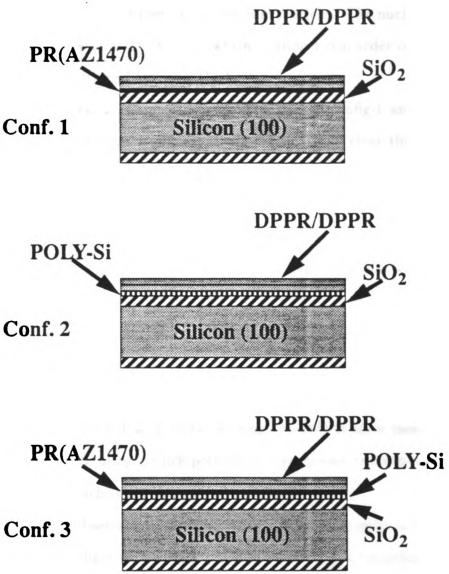

Figure 3.7. Schematic diagram of 3 configurations used for double-layer patterning.

the polysilicon, diamond was then deposited. Figure 3.9 shows SEM micrograph for diamond microchip prepared by Config-2. It is clear from this micrograph that the polysilicon layer also helped remove the residual particles. The nucleation density in the undesired area was $\approx$ 3 x10^4/cm^2 which is almost one order of magnitude less than the samples patterned by using Config-1.

The last configuration Config-3 is a combination of Config-1 and Config-2. The result of this configuration is shown in Fig. 3.10. It is clear that the sample is the cleanest. The nucleation density in the undesired area was $\approx$ 1 x10^4/cm^2. The above results show that the polysilicon layer was very successful. However, the most successful result was achieved by using sample with 1 μm and 2 μm in thickness. In the case of thin polysilicon layer 2000 $\mathring{A}$ in thickness, the film was stripped away during diamond deposition and the patterns were destroyed. In the case of thick polysilicon layer (3 μm), the problem was during etching the polysilicon. The etch of the thick polysilicon layer required longer time (> 17 minutes). The photo-resist mask was unable to withstand the etching process for a time longer than $\approx$ 17 minutes. Since the DPPR was used as a mask, etching the DPPR layer means loosing the nucleation sites. Also, using a thick polysilicon layer makes the step of the diamond patterns too high which is not desired for metalization.

Based on these observations, most of the diamond films used in this study were patterned using Config-1 or Config-3. A 3 to 4 μm of low temperature oxide was deposited instead of a 2 μm thermally grown oxide in the case of Config-1. In the case of Config-3 only 1 μm of polysilicon layer was used. Using the double-layer patterning technique developed in this research we were able to have a microstructure with minimum feature size of 5 μm in width. Fig. 3.11 shows SEM micrograph for an array of resistors with different dimensions.

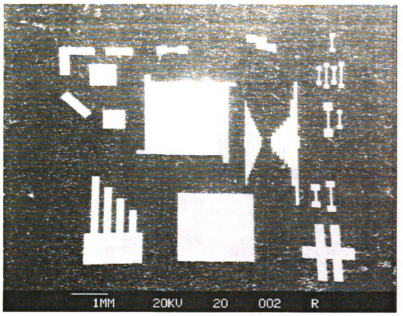

Figure 3.8. SEM micrograph for diamond microchip prepared by Config-1.

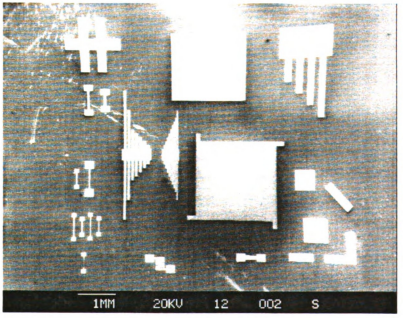

Figure 3.9. SEM micrograph for diamond microchip prepared by Config-2.

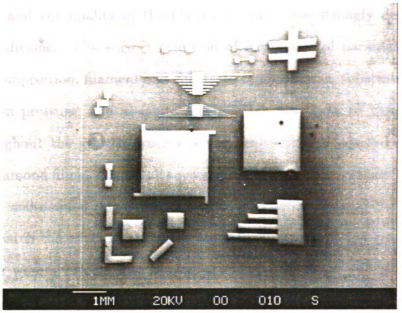

Figure 3.10. SEM micrograph for diamond microchip prepared by Config-3.

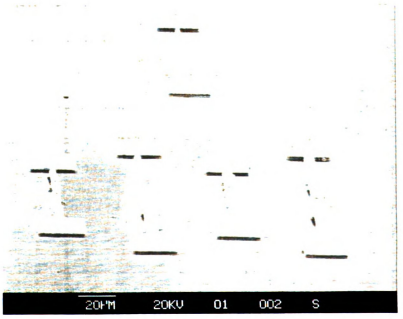

Figure 3.11. SEM micrograph for an array of resistors with different dimensions.

3.5 Effect of Deposition Parameters

The structure and the quality of the CVD diamond films strongly depend on the deposition conditions. The correct selection of experimental parameters, such as reactant gas composition, filament and substrate temperatures, substrate to filament spacing, system pressure, and absolute and relative flow rates of gases, and their stability throughout the growth process is very important to achieve reproducible, high quality diamond films. Almost all successful diamond growth experiments appear within a fairly well-defined range of parameters.

In this research the effect of the substrate temperature and the gas composition and flow rates were studied. The source gases were H_2 and CH_4 or C_2H_2 in the presence or absence of CO. The deposited films were characterized by SEM, Raman spectroscopy and surface profiler.

3.5.1 Effect of Substrate Temperature

In this research the substrate temperature was studied at 825 °C, 890 °C and 925 °C. In all cases, the total pressure was kept at about 50 Torr and the gas flow rates used were 100 sccm, 0.75 sccm and 12 sccm for H_2, C_2H_2 and CO, respectively. Raman spectra for the samples deposited at different substrate temperatures are shown in Figure 3.12. All spectra show the characterization peak at 1332 cm^{-1}. The broad shoulder around 1500 cm^{-1} indicates amorphous diamond-like component in the film.

These results show that the quality of the diamond film improves when the substrate temperature increases from 825 °C to 890°C, and then the quality shows some deterioration at 925°C. As determined by surface profiler, it was also observed that the growth rate of the diamond film increases with increasing temperatures from 825 °C ($\approx$0.18 μm/hr) to 890 °C ($\approx$0.28 μm/hr). This observation is consistent with the results reported by other investigators [122, 123, 125].

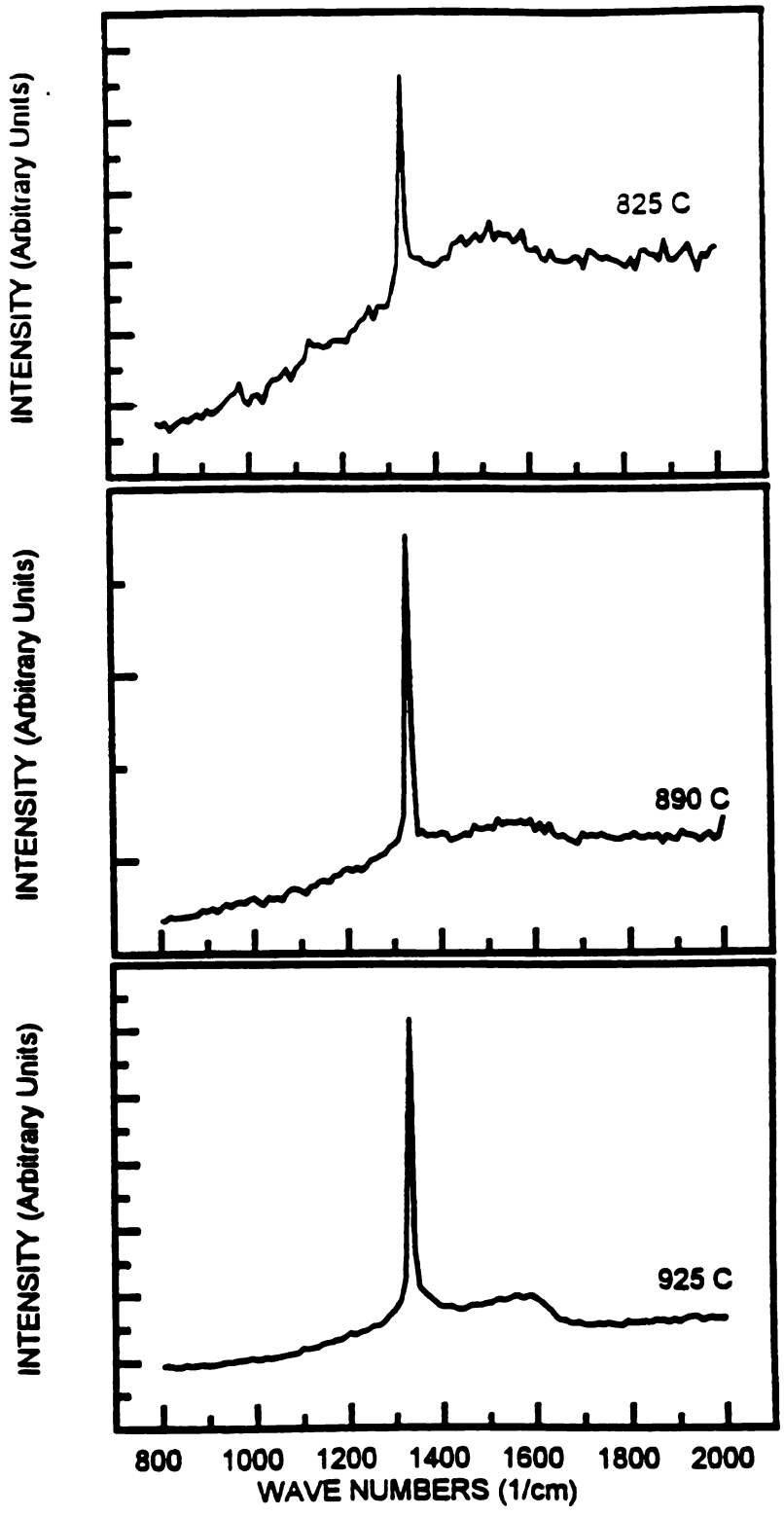

Figure 3.12. Raman spectra for the samples deposited at different substrate temperatures; a) 825 °C b) 890 °C c) 925 °C.

3.5.2 Effect of Gas Composition and Flow Rates

Most of the reported results at high substrate temperatures showed that the graphitic components in the film increased with increasing methane concentration in the hydrogen gas mixtures [111, 123]. To investigate this effect, a number of diamond films were deposited at different hydrogen flow rates while keeping all other deposition conditions the same.

In Fig. 3.13, the Raman spectra of deposited films on silicon at 890 °C show the effect of different concentrations of methane in hydrogen. CH_4 flow rate was kept at 0.75 sccm and CO flow rate was kept at 12 sccm. The total gas pressure was kept at 50 Torr during deposition. An inspection of these Raman spectra show that, as the hydrogen flow rate decreased from 100 sccm to 40 sccm (methane concentration increased), the graphitic components in the film increased. A degradation in purity of the diamond is clearly visible from the presence of large graphitic peak especially in spectrum 95L (40 sccm of H2), 93L (50 sccm of H2) and in spectrum 96L (55 sccm of H2). The diamond peak was relatively small in these samples. The best quality was for sample 92L (100 sccm for H2, 0.700 sccm for CH4, 12 sccm for CO). The effect of methane concentration on the internal stress of the diamond film will be described in chapter 4 (section 4.5).

Effect of CO

Various studies have shown that oxygen plays an important role in the growth mechanism of CVD diamond [97, 98]. These studies have shown that addition of oxygen improves CVD diamond purity and growth rate. However, adding even small amounts of oxygen resulted in failure of filament. Therefore, an alternative way was adopted and CO instead of pure oxygen was used. The effectiveness of CO in supplying oxygen or modifying the character of the film was observed by Raman Spectra. Raman Spectra for two samples deposited with and without CO are shown

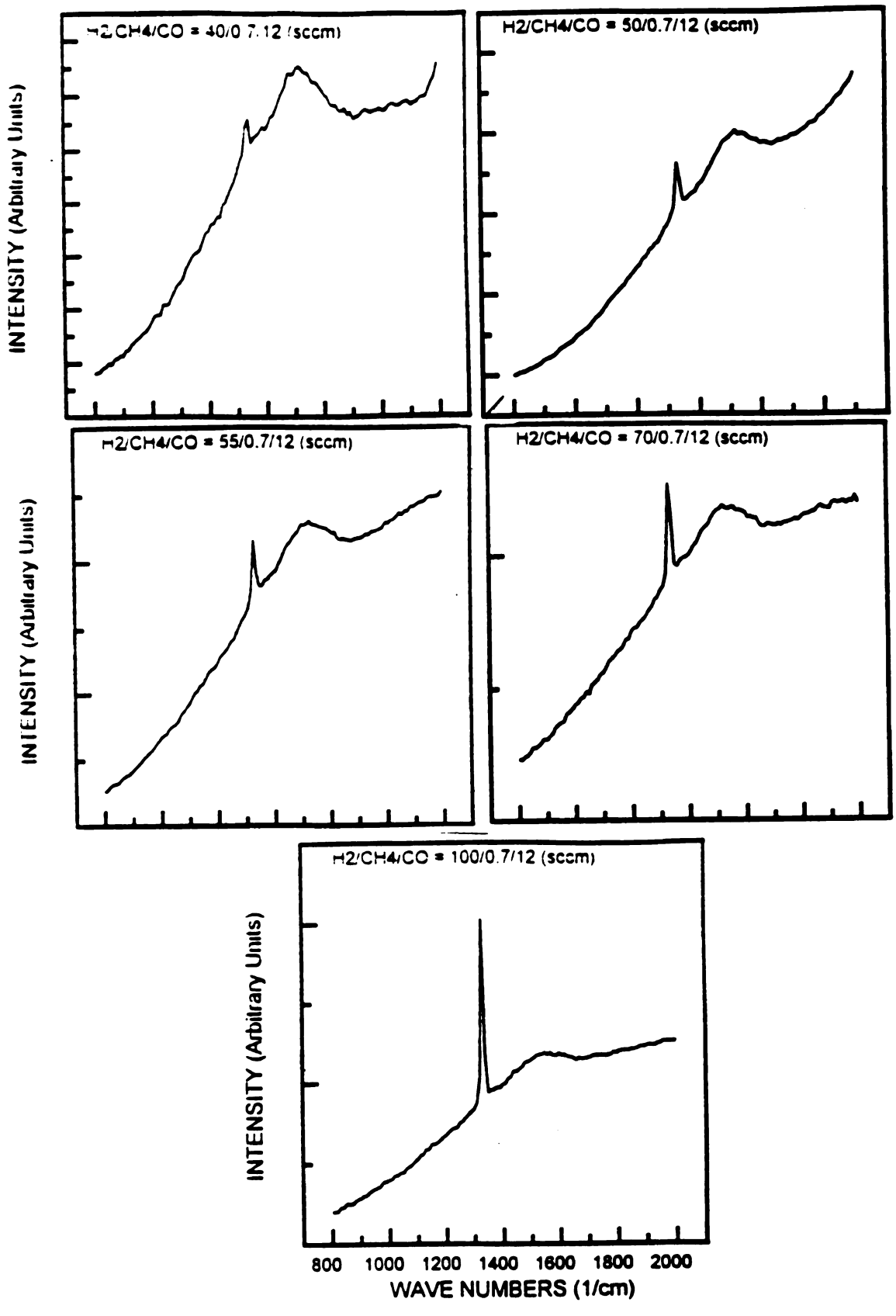

Figure 3.13. Raman spectra for the samples deposited at different hydrogen flow rates. CH_4 = 0.7 sccm and CO = 12 sccm for all samples.

in Fig.3.14. A degradation in purity in the absence of CO was clearly visible from the presence of large graphitic peak (spectrum a). However, an SEM inspection of the film without CO did not reveal any significant difference. In addition to the above mentioned effect, another effect was also observed for the first time which is related to the internal stress of the diamond film. This effect will be described in chapter 4 (section 4.5).

In summary of this study, the correct selection of deposition parameters for best quality diamond film was optimized and given in Table 3.2. some of the value individually or in combination are reactor dependent. Therefore, this formulation should be considered more specific to the present deposition system than a general one.

Table 3.2. Optimum processing parameters.

Substrate to filament spacing	Gas Flow (SCCM) H_2	CH_4	CO	Fil. Temp. (°C)	Sub. Temp. (°C)	Pressure (Torr)
(3/16)"	100	0.7	12	2400	890	50

3.6 Doping of Diamond Films

Since gaseous doping sources are highly poisonous, only solid sources (boron powder) were considered in this research. Pure boron powder was introduced directly into the chamber. The powder is placed on the substrate holder (heating plate) using a specially designed holder. Fig. 3.15 shows a schematic diagram of the boron holder. The holder consists of Mo plate (1 mm thick) with a number of 1 mm diameter holes drilled in it. The plate is inserted in a clip which covers its one face and a selected number of holes are filled with boron powder. One hole takes an average 0.2 mg of

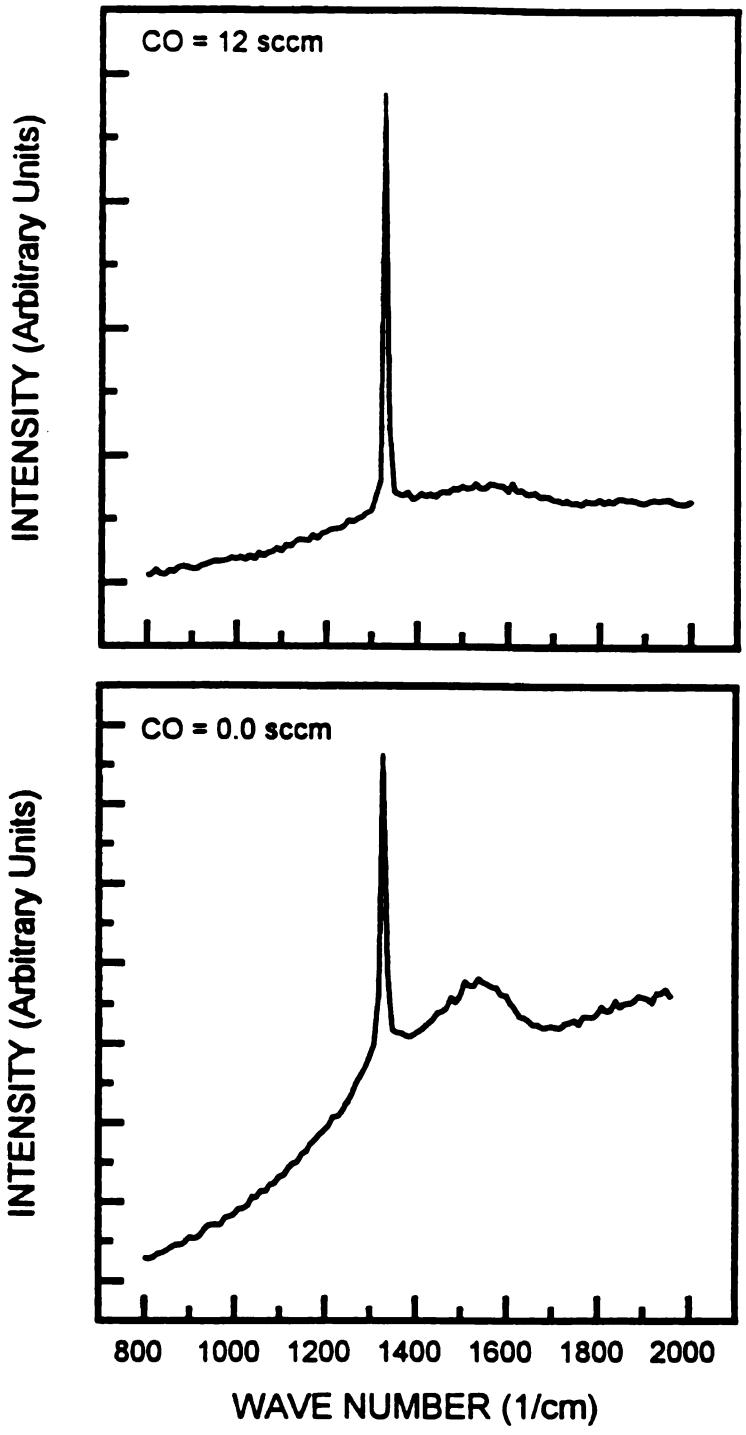

Figure 3.14. Raman spectra for the samples deposited with or without CO.

boron powder to fill. The boron powder was introduced into the chamber in two different approaches. In the first approach only one boron holder was used. The boron holder is placed very close to the substrate (within 0.5 cm) at a fixed place on the substrate holder. In the second approach two boron holders were used and were placed one at each side of the substrate.

In order to see the effect of each approach, a test chip was designed and fabricated. The size of the chip is 1.1 inch x 1.1 inch. It employs two masks. The masks were designed using CAD software and fabricated on 2 inch x 2 inch high resolution photographic glass plates at Ford's photographic facility. The first mask is used to define the desired diamond growth area. The second mask is for metalization. In most cases, the metal pattern was generated by shadow mask. The mask was fabricated on thin Cu plate at the Ford's photographic facility.

The test chip consists of a rectangular shaped diamond resistors of various size, 500 to 1000 μm wide and 1500 to 4000 μm long structures. Figure 3.16 shows a composite layout of this test chip. Since the test chip contains only diamond resistors, the chip will be refered to as discrete-chip. The resistors are grouped into four identical groups (G-1, G-2, G-3 and G-4). Each group contains five different resistors which are labeled as R_A, R_B, R_C, R_D and R_E as shown in Fig.3.16 and illustrated further in Table 3.3. The discrete-chip was fabricated in three steps. Using the first mask, an undoped diamond film was deposited on the top of an oxidized silicon substrate. After the deposition of the undoped diamond films, the substrate was loaded back into the chamber to be doped with boron powder using one of the two approaches described earlier. After the deposition of the doped layer, the metal was then evaporated using the shadow mask. The resistance of each resistor was measured using a multimeter(HP 3468A).

Table 3.3 shows the result of the resistance measurement using the first approach (one boron holder). The boron holder was placed in the right side of the undoped

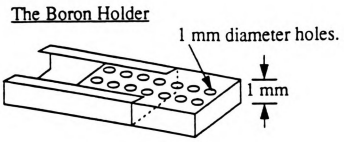

Figure 3.15. Schematic diagram of the boron holder.

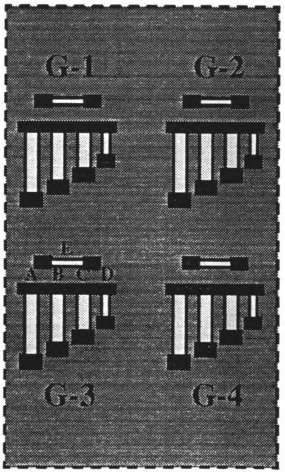

Figure 3.16. Composite layout of the discrete-chip.

Table 3.3. Resistance measurements for one boron holder.

Resistance (kΩ)		Change %
G-1	G-2	
$R_A = 1100$	$R_A = 267$	+312
$R_B = 821$	$R_B = 186$	+341
$R_C = 630$	$R_C = 157$	+301
$R_D = 297$	$R_D = 61$	+386
$R_E = 476$	$R_E = 163$	+192
G-3	G-4	
$R_A = 1400$	$R_A = 393$	+256
$R_B = 970$	$R_B = 237$	+309
$R_C = 798$	$R_C = 206$	+287
$R_D = 405$	$R_D = 97$	+317
$R_E = 563$	$R_E = 209$	+169

Table 3.4. Resistance measurements for two boron holders.

Resistance (kΩ)		Change %
G-1	G-2	
$R_A = 83$	$R_A = 189$	+127
$R_B = 101$	$R_B = 119$	+18
$R_C = 97$	$R_C = 64$	+51
$R_D = 114$	$R_D = 39$	+192
$R_E = 75$	$R_E = 127$	+69
G-3	G-4	
$R_A = 149$	$R_A = 271$	+82
$R_B = 147$	$R_B = 165$	+12
$R_C = 131$	$R_C = 95$	+38
$R_D = 174$	$R_D = 76$	+128
$R_E = 113$	$R_E = 89$	+27

substrate (closer to resistor R_D (G-2) and R_D (G-4)). The result shows that the resistor closest to the boron holder has the lowest value of resistance. The percentage change in resistance was in the range of 170 to 486 %.

By using two boron holders (second approach), one at each side of the substrate, the percentage change of resistance for most resistors was in the range of 12 to 82 % less than 100 % except for resistor R_D and R_A which was over 100 % . This is because one resistor was located next to the boron holder and the other was located in the center of the sample (see Figure 3.16 and Table 3.4).

Based on this observation, a new boron holder was designed and fabricated. The schematic diagram of the new design is shown in Figure 3.17. In the new design, two different size of holes were drilled in the Mo plate from the top to the bottom. The large hole (six large holes were drilled in each Mo plate) with 1.2 cm in diameter is surrounded by 8 small holes 1 mm in diameter. The small holes are used to carry the boron powder as was done in the old design. Each one of the large holes encloses a different diamond chip. The doped layer of diamond was deposited thru the opening of the large hole. This new boron holder was especially designed to be used for the microsensor microchip. The fabrication process of the microchip will be described in chapter 4 section 4.3. The size of the microchip is 1 cm x 1 cm. Each sample contains six chips. Table 3.4 shows the result of resistance for an identical resistor from each chip. Six chips were fabricated at the same time. Since in the new design, the holes filled with boron surrounded each chip, as expected, the change in resistance at any position on any chip was very small. Table 3.4 shows that the maximum percentage change was $\approx$ 16 %, depending on the number of holes filled with boron. Therefore, for better reproducibility of temperature and hence, of doping concentration and distribution of boron everywhere on the surface of the chip, the new design is the most successful and reliable approach to dope diamond chips. The vapor pressure of boron at growth temperature appears to be sufficient to evolve boron vapor for

controlled doping of the diamond films. The temperature of the boron powder is assumed to be equal to the substrate temperature as measured by thermocouple and is not measured independently.

All the films display typical Raman spectra of diamond with a strong peak at 1332 cm^{-1}. Although there is some scatter in the data (resistance measurements), the controlling of doping through the quantity of boron powder appears to hold sufficiently. As a result of these observations, all the films for the piezoresistive measurements were deposited on an undoped buffer layer of diamond using the second or third approach.

3.7 Homoepitaxial Doped Film

In this research a thin doped diamond film was grown on a synthetic diamond substrate. The diameter of the diamond substrate was 3 mm and the thickness was 400 μm. The boron holder was placed next to the diamond substrate. The Raman spectrum of doped homoepitaxial film deposited on thin diamond sample is shown in Fig. 3.9. The spectrum shows strong peak at 1332 cm^{-1}. The intensity of Raman signal for homoepitaxial films is much larger than polycrystalline films (see Fig. 3.13). The full width at half maxima (FWHM) of diamond peak is relatively much smaller for homoepitaxial films (3 cm^{-1} for homoepitaxial, 7 to 9 cm^{-1} for polycrystalline film). An important observation to note is that a peak corresponding to Diamond-like Carbon (DLC) or disordered carbon at 1355 cm^{-1} is totally absent which is another evidence of the superior purity of the homoepitaxial diamond films.

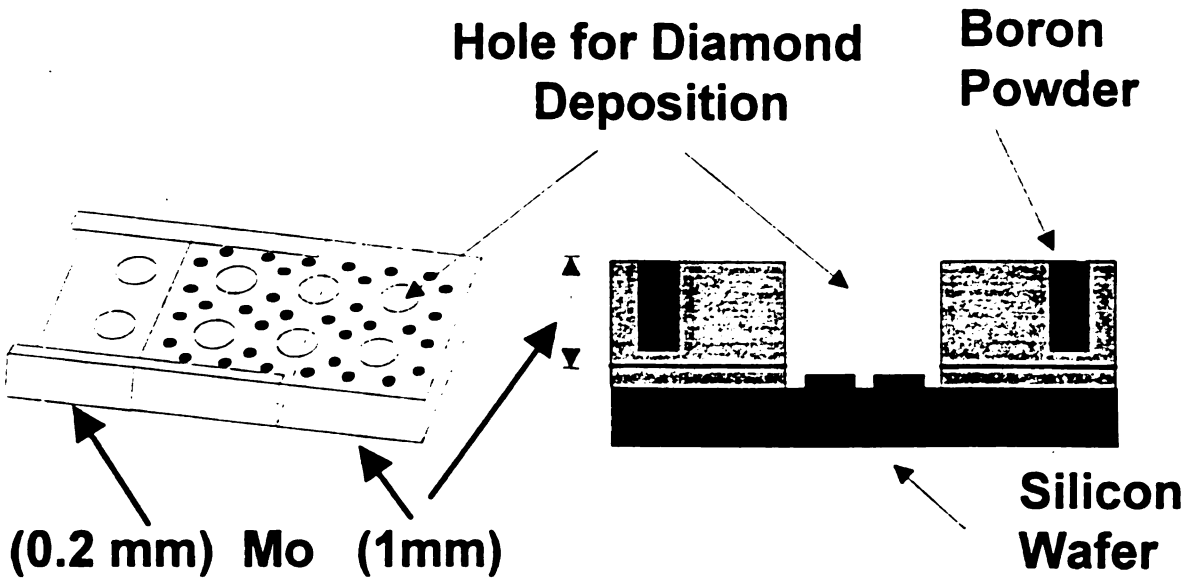

Figure 3.17. a) Boron powder holder b) Cross-section holder placed on silicon.

Table 3.5. Resistance measurements for two samples.

Sample I.D.	Resistance (kΩ)		Change %
355D	Chip-1, R = 385.1	Chip-2, R = 410	+6
	Chip-3, R = 302.4	Chip-4, R = 310.25	+3
	Chip-5, R = 130.15	Chip-6, R = 128	+2
353D	Chip-1, R = 20.4	Chip-2,	
	Chip-3, R = 18.3	Chip-4, R = 21.25	+16
	Chip-5, R = 19.5	Chip-6, R = 22.3	+14

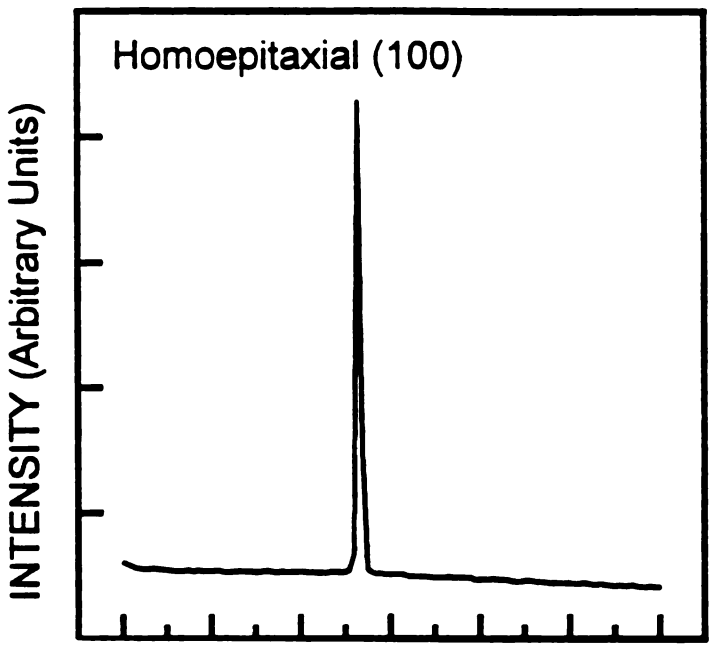

Figure 3.18. Raman spectrum of doped homoepitaxial films deposited on type 2a diamond substrates (Dubbelldee Harris Corp., Mt. Arlington, NJ).

3.8 Summary

In this chapter, the study to synthesize and characterize semiconducting diamond film for device fabrication has been presented. The DPPR seeding method to enhance the low intrinsic nucleation density of diamond on non-diamond substrates was described and was improved by using two layers of DPPR instead of one layer. Experimental parameters such as substrate temperature and relative flow rate of gases were studied and optimized. Three different approaches to load the boron powder into the chamber were studied.

CHAPTER 4

Design and Fabrication of a Multisensor Microchip

4.1 Introduction

This chapter deals with the design and fabrication of a multipurpose test microchip. Fabrication details of micromechanical structures such as cantilever beams, bridges, and membranes with different dimensions and shapes are described. Boron doped layers were selectively deposited on undoped diamond films using boron powder as doping source and low temperature oxide as doping mask. For metalization of diamond devices, a double layer of Pt/Ti is used. An appropriate process for patterning of the Pt/Ti layers with wet chemical etching solution was developed. The total stress in the diamond film was also measured. All the patterning methods presented in this chapter are adopted from IC fabrication technology.

4.2 Microchip Design

A multisensor test microchip is designed to demonstrate the feasibility of diamond film for sensor applications. The sensor test chip contains a series of resistors of

varying sizes, shapes and orientation. It also contains cantilever beams, bridges, membranes, a MOSFET, Hall structure, a pressure sensor and an accelerometer. Each device is designed for a specific purpose. The resistors are designed for thermal and piezoresistive measurements. The size of the chip is 1 cm x 1 cm. The smallest feature size is about 5 μm in width. It employs a six mask fabrication process.

Fig 4.1 shows a composite layout of the masks whereas the individual mask layouts are shown in Figs. 4.2, 4.3, 4.4 and 4.5. The masks were 5 inch x 5 inch with chrome patterns which were designed and fabricated at Ford Scientific Research Laboratory.

Mask 1 : Mask 1 is used to define the desired diamond growth area (first undoped diamond layer). The layout of Mask 1 is shown in Fig. 4.2(a).

Mask 2 : Mask 2 is used to define holes on the back side of the wafer for membrane (pressure sensor). The layout of Mask 2 is shown in Fig. 4.2(b). Two sided mask aligner and infrared microscope are used for simultaneous mask alignment using masks 1 and 2. The design of the back etch mask is based on the following equation [178].

$$l = M - \sqrt{2}(T - h) \tag{4.1}$$

where l is the diaphragm size, M is the mask opening and T is the wafer thickness. In case of silicon membrane h is the membrane thickness. However, in this work the wafer is etched to the back side of the diamond film. KOH is used to etch silicon. Since KOH does not etch diamond, thus $h = 0$. Figure 4.3(a) shows Mask 1 and Mask2 aligned simultaneous and the expected membrane size (light area) in the middle.

Mask 3 : The third mask is used to selectively deposit doped diamond on the previously deposited undoped diamond films. Selective growth of boron-doped polycrystalline diamond films is achieved using low-temperature SiO_2 as a masking

layer. SiO_2 is removed selectively using mask 3. Fig. 4.3(b) shows the layout of this mask.

Mask 4 : The fourth mask is designed to define the metal contacts in the passivation layer. The layout of this mask is shown in Fig. 4.4(a).

Mask 5 : The metal mask is designed to define the metal interconnection lines and pads. The width of all the interconnection lines is 50 μm. The size of bonding pads is 500 μm x 500 μm, except for the Hall structure for which the size of bonding pads is 700 μm x 700 μm . Fig. 4.4(b) shows the layout of this mask.

Mask 6 : The layout of mask 6 is shown in Fig. 4.5. This is designed to define window for sacrificial layer etching in order to fabricate microstructures such as cantilever beams and bridges. This also can be used to fabricate the accelerometer sensor.

4.3 Metalization

Since the diamond devices are intended to operate at high temperatures in chemically and physically harsh environment, the choice of the metal is important.

In case of test chip, diamond film is deposited on SiO_2 or undoped polycrystalline silicon. Therefore, in addition to a good ohmic contact of metal with diamond, an additional requirements of a good metalization scheme may include planarization and good mechanical bonding with both diamond and the insulated layers.

A double-layer Pt/Ti structure was used for ohmic contacts in this research. This is because, the carbide of titanium is easily formed at 400 °C [145] (good adhesion). This is also because of the high melting point of Pt and its high resistance to oxidation and to KOH etchant.

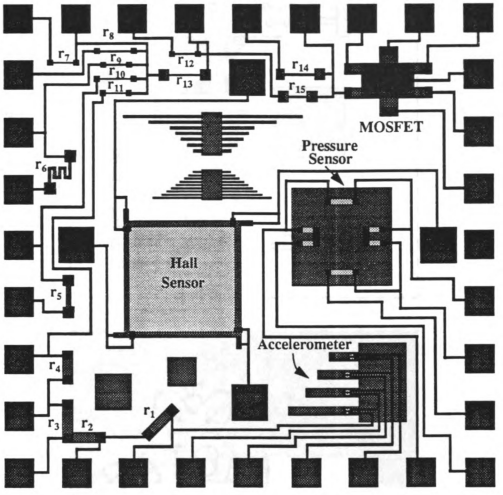

Figure 4.1. Composite layout of the masks. Resistors r_1 to r_{15} are used for piezoresistive and temperature measurements.

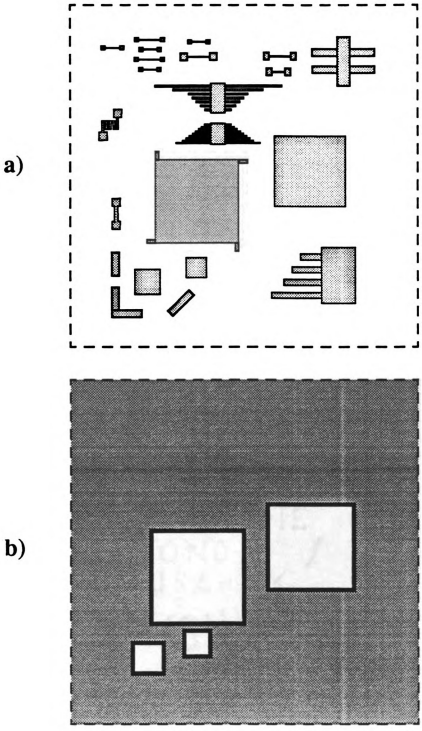

Figure 4.2. (a) Layout of mask 1 (undoped diamond), (b) Layout of mask 2.

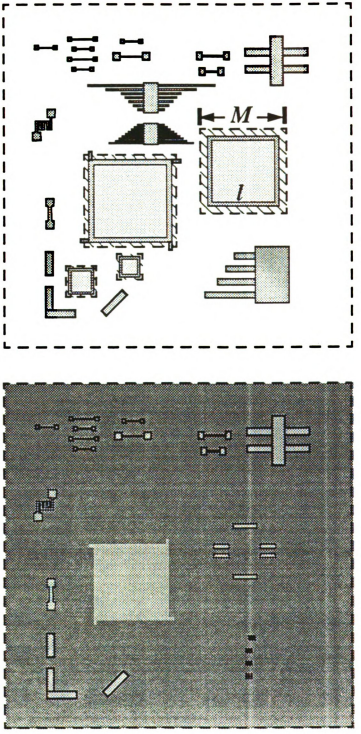

Figure 4.3. (a) Combined mask 1 and mask 2, (b) Layout of mask 3 (doped diamond).

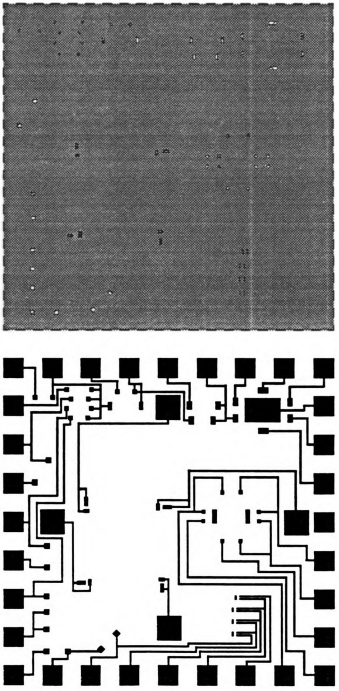

Figure 4.4. (a) Layout of mask 4 (metal contacts), (b) Layout of mask 5 (metal patterns).

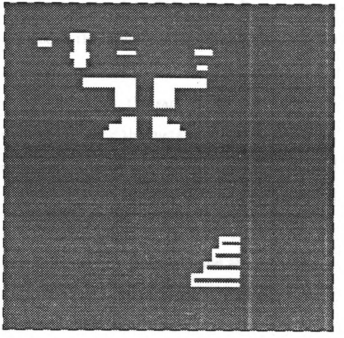

Figure 4.5. Layout of mask 6 (Sacrificial layer window).

In earlier work [125] on the double-layer Pt/Ti structure, the metal pattern was generated by shadow mask. However, in the case of the microchip it is necessary to develop a process which is compatible with the IC fabrication technology. A wet chemical etch process which was developed in this research is described next.

As a first experiment, the thickness of the Ti layer was 200 $\AA$ and the thickness of the Pt layer was 0.5 μm. Both metals were deposited using E-Beam evaporation system. In order to avoid oxidation of the Ti layer, the Pt was evaporated immediately after the Ti without breaking the vacuum in the system. Pressure during evaporation process was $\approx 1 \times 10^{-7}$ torr.

After evaporation of the metals, the sample was coated with photoresist. Next the photoresist was patterned using the metal mask of the microchip (Mask 5). The Pt/Ti layer was then etched in a saturated solution of H_2O:HNO_3:HCl/4:4:1 at 90°C for 2 min, followed by a rinse in deionized water. Figure 4.6 shows SEM micrographs for sample during the etch and before striping the photoresist. It is clear that the photoresist was etched by the chemical etchant and the photoresist lines were pulled away from the substrate surface.

From these observations following deductions were drawn.

- The photoresist film as a mask by itself was not sufficient. Other or additional mask is required.

- The diamond film step coverage was not good. A thicker Pt film is required.

- After testing the devices by a multimeter, it was observed that the devices were not electrically isolated from each other. This might be due to the base layer (Ti) forming its oxide during the inspection and before ending the etch process. A thinner Ti layer is suggested and the etching should be done in one step without removing the sample from the etch solution.

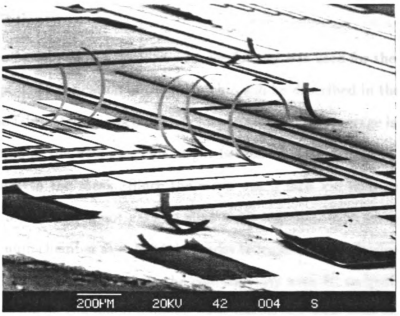

Figure 4.6. SEM micrographs for sample during the etch and before striping the photoresist. Photoresist lines were pulled away from the substrate surface.

On the basis of the above observations, the metalization scheme was changed as follows:

- (1) Decrease of Ti layer thickness from 200$\mathring{A}$ to 125$\mathring{A}$.
- (2) Increase of Pt layer thickness from 0.5 μm to $\approx$ 1.0 μm.
- (3) Cover the Pt/Ti layer with plasma nitride or oxide before coating with photoresist.

The above metalization scheme was successful and was used for the fabrication of the microchip. The fabrication of the microchip will be described in the next section. In most of the fabricated microchips the cross sectional step coverage is still not good enough on some of the devices. This might be due to mishandling or misalignment of the sample with the mask. Since the mask was 5 inch x 5 inch and the sample was 1 inch x 3 inch it was not easy to align both together. The samples were heat treated in vacuum chamber at $\approx$ 500 °C in order to improve the adhesion and stabilize the contacts. Furthermore, to verify the compatibility with IC technology, gold wire bonding was made on the metal bonding pads before and after heat treatment. The gold wire adhesion was stronger after the heat treatment.

4.4 Microchip Fabrication

In order to demonstrate the feasibility of diamond for microsensor applications in harsh environments, it is important to test the use of diamond piezoresistive and micromechanical structures on the same chip. This can be achieved by selectively deposited two polycrystalline diamond layers. The first layer is undoped polycrystalline diamond layer which can be used as micromechanical structures such as cantilever beams, bridges and membranes. The second layer is for piezoresistor which can be achieved by selectively deposited p-type doped layers.

4.4.1 Undoped Diamond films

The major fabrication sequence of the multisensor microchip is shown in Fig. 4.7. Starting substrates were 4-inch p-type (100) silicon wafers.

Mask 1 and Mask 2

First, the wafer was cleaned by piranha solution (H_2SO_4:H_2O_2, 1:1) for 20 minutes. Second, two layers of LPCVD silicon nitride and of low temperature oxide (LTO), with thicknesses of 100 nm and 3 μm, respectively, were deposited on both sides of a Si wafer Fig. 4.7(a). Wafer was then coated with positive resist on the backside and front side. The front side was coated after baking the wafer at 100 °C for 45 seconds on a hot plate. Wafer was then heat treated (softbake at 90 ° for 15 minutes). Two diamond powder photoresist DPPR layers were then dispensed on the front side of the wafer. The wafer was again heat treated (softbake at 90 ° for 15 minutes).

Using a double-sided mask aligner, both resists were patterned as shown in Fig. 4.7(b). Mask 1 and Mask 2 were used in this step. The LTO and Si_3N_4 layers were then dry-etched from the backside Fig. 4.7(c). The wafer was then cut into 1 inch x 3 inch piece and loaded into the diamond deposition system. An undoped diamond film was grown at 890 °C in the HFCVD reactor. The photoresist evaporates in the reactor and the remaining diamond particles act as seeds for the growth of polycrystalline diamond film only on the front side. A part of the LTO layer is removed by the atmosphere of diamond deposition process (Fig. 4.7(d)). Figure 4.8 shows SEM micrographs for a structure from the microchip fabricated at this level.

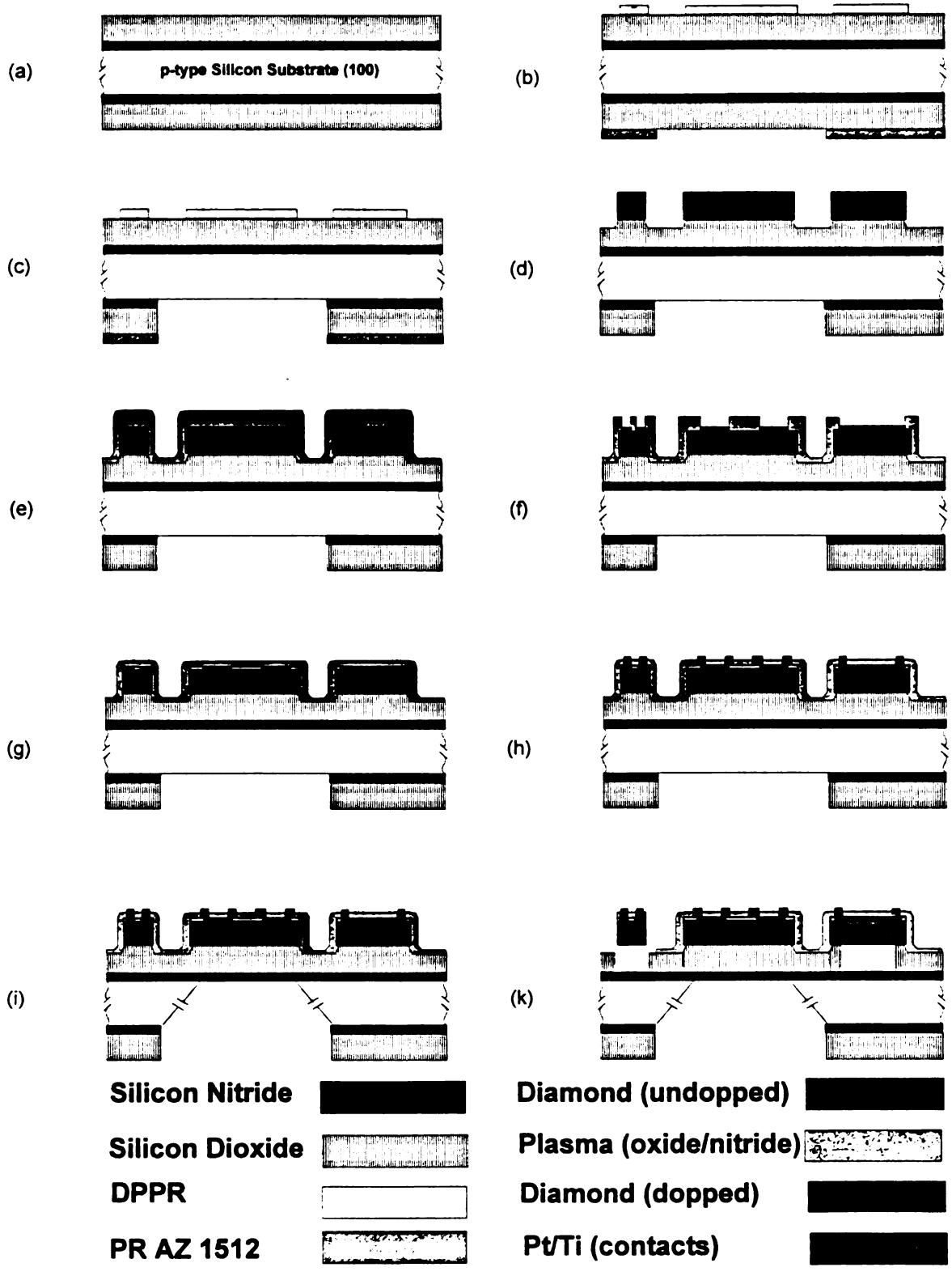

Figure 4.7. Major fabrication process steps for the multisensor microchip.

4.4.2 Selectively Doped layer

Mask 3

A new layer of Low temperature oxide was then deposited over the entire sample and patterned using Mask 3 (standard photolithography was used). The diamond was then exposed by removing the oxide from the desired areas by using buffered oxide etchant. The sample was again loaded in HFCVD reactor to grow p-type diamond which can only grow in exposed areas as shown in Fig. 4.7(f). Boron holder which was designed and fabricated in this research was used to carry the boron for in-situ doping. The effectiveness of this technique was described in chapter 3. An SEM micrograph taken after the deposition of the doped diamond is shown in Fig. 4.9.

4.4.3 Metalization Steps

Mask 4 and Mask 5

Plasma oxide and plasma nitride were then deposited over the entire sample (Fig. 4.7(g)). Then plasma oxide and plasma nitride were dry etched in order to define holes for metal contacts. Titanium and platinum layers were evaporated on the entire sample using E-beam system. The metal were then patterned as described in the metalization section.

4.4.4 Micromechanical Structures

Mask 2 and Mask 6

A process has been developed in this work for fabricating micromechanical structures, particularly cantilever beams, bridges (doubly supported beams) and membranes. Surface and bulk micromachining techniques are used to fabricate the cantilever beams, bridges and membranes. The sacrificial layers were low temperature

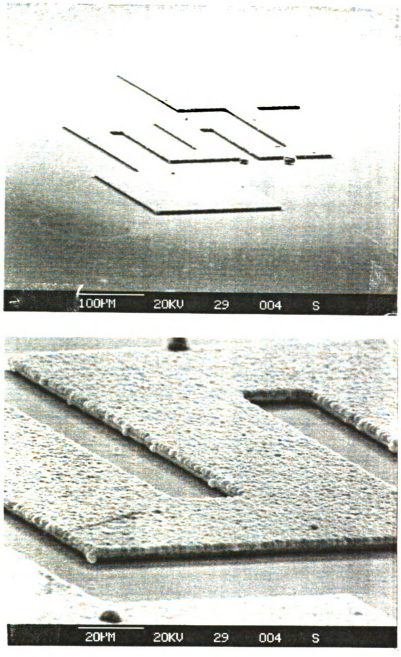

Figure 4.8. SEM micrographs for a resistor (a) top view and (b) close-up view from the microchip.

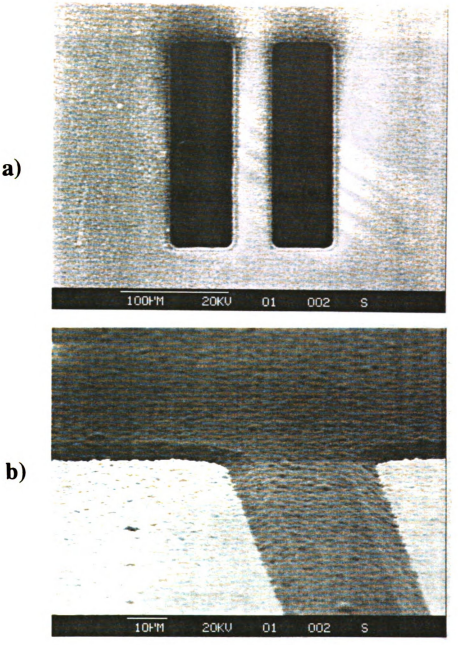

Figure 4.9. SEM micrographs showing doped diamond and SiO_2 (LTO) mask; (a) top view, doped diamond (dark areas) and LTO (bright area), and (b) close-up view, doped diamond (bright areas) and LTO (dark area).

a)

b)

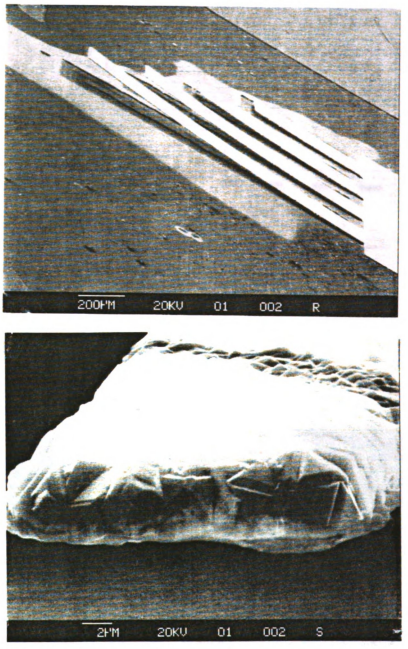

Figure 4.10. SEM micrograph showing (a) array of cantilever beam structures curled upward (600 to 1500 μm in length, 150 μm in width and 4 μm in thickness) (b) close up view of one of the beam.

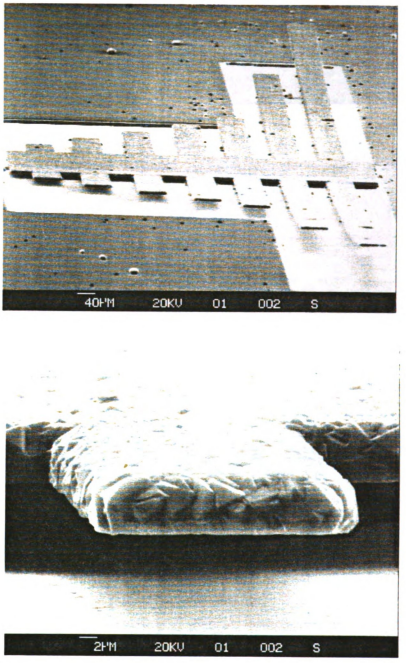

Figure 4.11. SEM micrograph showing (a) array of cantilever beam structures (200 to 1200 μm in length, 20 μm in width and 4 μm in thickness) (b) close up view of one of the beam.

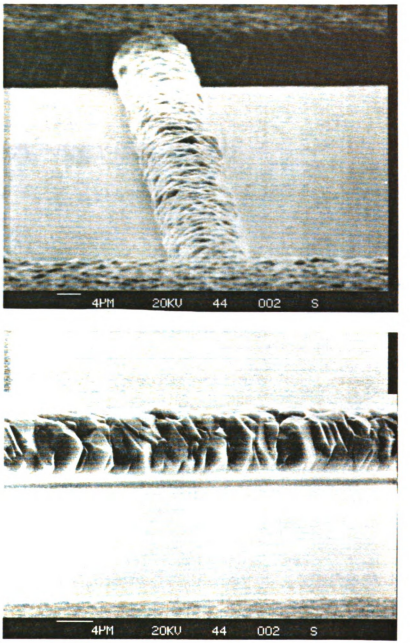

Figure 4.12. SEM micrograph of a bridge (≈ 8 μm in width, 100 μm in length and 4 μm in thickness); (a) top view and (b) side view (bridge does not touch the substrate).

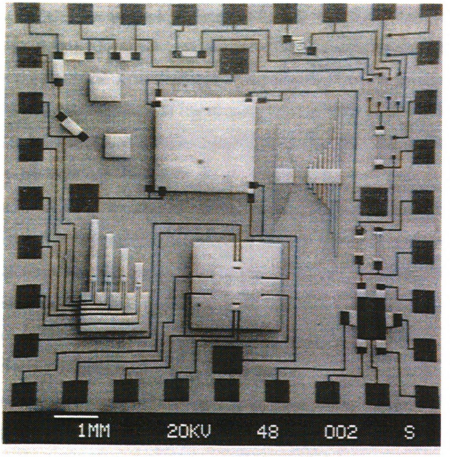

Figure 4.13. SEM micrograph showing an overview of the multisensor microchip.

oxide (LTO) or undoped polycrystalline silicon. An array of cantilever beams of various sizes ranging from 100 to 1500 μm in length, from 20 to 150 μm in width and 3 to 5 μm in thickness were fabricated on the microchip. An array of bridges of various sizes ranging from 100 to 200 μm in length, from 5 to 50 μm in width and 3 to 5 μm in thickness were also fabricated on the microchip. These micromechanical structures were fabricated as follows:

After patterning the metal (Fig. 4.7(h)), the sample was loaded in a KOH bath (30 % at 80 °C) for anisotropic etching of silicon (Fig. 4.7(i)). Prior to the loading into the KOH bath, the sample was heated to 500 °C to improve the adhesion of the metal to the substrate. After heating the sample, a thin layer of plasma nitride 3000 to 4000 $\AA$ was then deposited on the sample. This layer was used to protect the edge of the titanium layer and other structures from KOH, since the etch of the silicon usually takes more than 12 hours.

After silicon etch, two layers of photoresist AZ1470 (in order to have a thick layer of photoresist) were then spun on the sample and then softbake (30 min at 90 °C). The photoresist was then exposed and developed using Mask 6 of the test chip. The photoresist thickness after patterning was $\approx$ 2.5 μm. The plasma nitride which was deposited earlier, was then dry etched to expose the sacrificial layer.

The sacrificial layer LTO was etched by buffered hydrofluoric acid (BHF 7:1) to form the free standing structures as shown in Figures 4.10, 4.11 and 4.12. During this step, the sample was removed from the etching solution every three hours. The sample was inspected under the microscope and then loaded in a furnace to hardbake the photoresist and again loaded back into the etchant bath.

Fig. 4.10(a) shows that the diamond cantilever beams are curled upward indicating an intrinsic stress in diamond films. The intrinsic stress in the diamond film will be explained in the next section. Different micromechanical structures are shown in Fig. 4.11 and in Fig. 4.12. An SEM micrograph shown in Fig. 4.13 gives an overview

of the multisensor microchip. The light areas are Pt/Ti interconnects and bonding pads. The test-chip contains a number of structures, including piezoresistors, thermistors, a Hall structure, a MOSFET, a pressure sensor, an accelerometer, cantilever beams, bridges and membranes. The fabrication technology of pressure sensor and accelerometer was demonstrated in this chip. However, these sensor were not tested.

4.5 Intrinsic Stress in the Diamond Films

Generally, most deposited diamond thin films on silicon or other substrates used in microsensors are in a state of internal stress, either compressive or tensile [179, 180, 181]. The internal stress has an effect on the deflection of beams (accelerometer) and diaphragms (pressure) and thus influences the response parameters of sensors which use them. Tensile stress exceeding the strength of the film may break the film, and large compressive stress can cause films to buckle. Therefore, knowing the properties of internal stress of the diamond film is very important in controlling the flatness of films and in predicting the response parameters of sensors that utilize diamond films.

It is known that a layer of one material grown on another material with different mechanical properties is often in a state of stress. The stress may be due to thermal expansion mismatch between the film and substrate (thermal stress) or due to the difference in crystal structure between the bottom and top of the film or may be due to impurities or dislocations in the film.

The deformation of the thin film can be accommodated by the bending and compressing or expanding (depends on the curvature) of the substrate. The internal stress is compressive if the film tends to expand parallel to the surface (substrate bent upward) as shown in Fig. 4.14(a). The internal stress is tensile if the film tends to contract parallel to the surface (substrate bent downward) as shown in Fig. 4.14(b)

The type and magnitude of the intrinsic stress in the film usually depend on the

method of deposition and on the growing conditions of the films. In this work the stress is investigated as a function of methane fraction in a hydrogen environment with or without addition of carbon monoxide. Films with both tensile and compressive total (thermal and intrinsic) stress were produced depending on deposition conditions. The preparation of the sample and the measurement technique used to measure the stress is described next.

4.5.1 Sample Preparation

Starting material was a 4-inch p-type (100) silicon wafer. No oxide or nitride layers were deposited on the silicon wafer used for this study. After cleaning the wafer with piranha solution, two layers of DPPR were dispensed on the polish side of the wafer, using the coating procedure described in chapter 3. After coating the wafer with the DPPR layers, the wafer was heat treated (softbake) at 120 °C for 1 hour.

After this step the wafer was cut into pieces 1 inch x 1 inch each. The sample curvature was measured by determining the surface profile using Tencor P-2 instrument. The sample curvature was measured before and after the deposition of the diamond films. The total (thermal and intrinsic) stress was calculated from a radius-of-curvature measurement. The equation for the stress is [180, 181]

$$X = \frac{Y}{6(1-\nu)} \frac{t_s^2}{R\, t_f} \tag{4.2}$$

where $\frac{Y}{(1-\nu)}$ is the substrate biaxial Young's modulus, which for (100) silicon is 180 GPa. R is the net change in radius of curvature of the substrate, t_s and t_f are the substrate and film thickness.

4.5.2 Results

The result of this study is shown in Table 4.1.

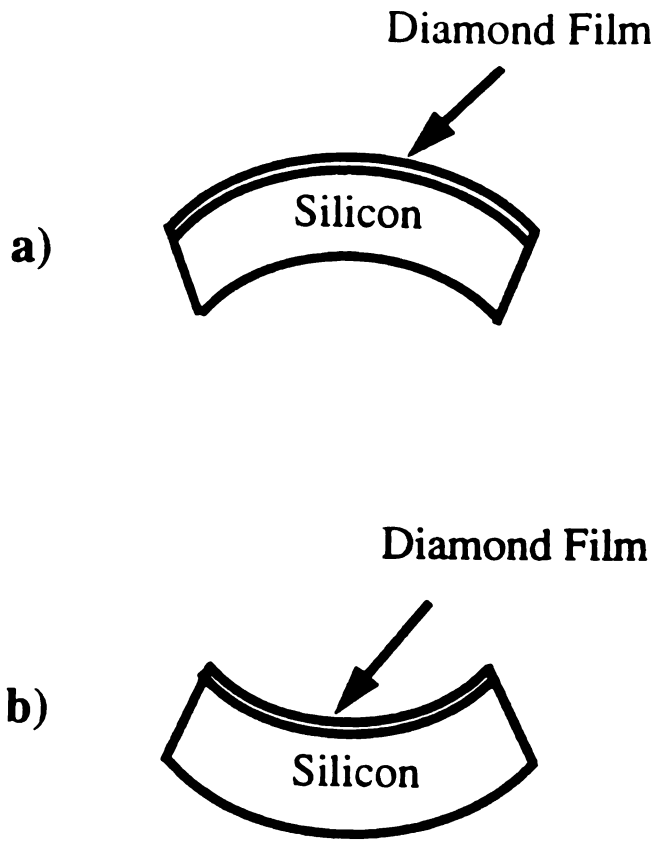

Figure 4.14. Convention showing (a) Compression (b) Tension.

Table 4.1. Stress dependence on methane concentration and carbon monoxide.

Sample I.D.	Gas Flow (SCCM) H_2	CH_4	CO	Methane %	Total Stress (MPa)
S3H92	100	0.7	12	0.621	- 80
S3H93	50	0.7	12	1.116	+ 81.4
S3H94	70	0.7	12	0.962	- 87.4
S3H95	40	0.7	12	1.328	+ 38
S3H96	55	0.7	12	1.034	+ 83.6
S3H97	50	0.7	12	1.116	+ 90.2
S4H00	50	0.7	0.0	1.38	+ 126
S4H01	60	0.7	0.0	1.15	+340
S4H02	70	0.7	0.0	0.99	+ 260
S4H05	100	0.5	0.0	0.497	- 149

Figure 4.15 shows the dependence of the total stress on methane concentration with or without carbon monoxide. In the present of carbon monoxide and for methane concentrations below 1 % the total stress in the film is compressive. For methane concentrations above 1 % the total stress in the film is tensile. The maximum stress was $\approx$ 90 MPa for 1.1 % of methane concentration. However, in the absence of CO the total stress is compressive for methane concentration of $\approx$ 0.5 % and is tensile for methane concentration above 1 %. It was also observed that the magnitude of the total stress was very high in comparison with the samples deposited in the presence of CO. The maximum tensile stress was 340 MPa which is more than 3 times higher than the sample deposited in the presence of CO. This result indicates that by using CO in the gas mixture, it is possible to control the type and magnitude of the total stress in the diamond films. This is very important for micromechanical sensor applications. To our knowledge, no study has been made or reported on the effect of CO on the total stress in the diamond films. Windischmann et al [181] have studied the dependence of the total stress on methane concentration. Their diamond films were deposited by microwave plasma CVD. They reported that the total stress was tensile with a

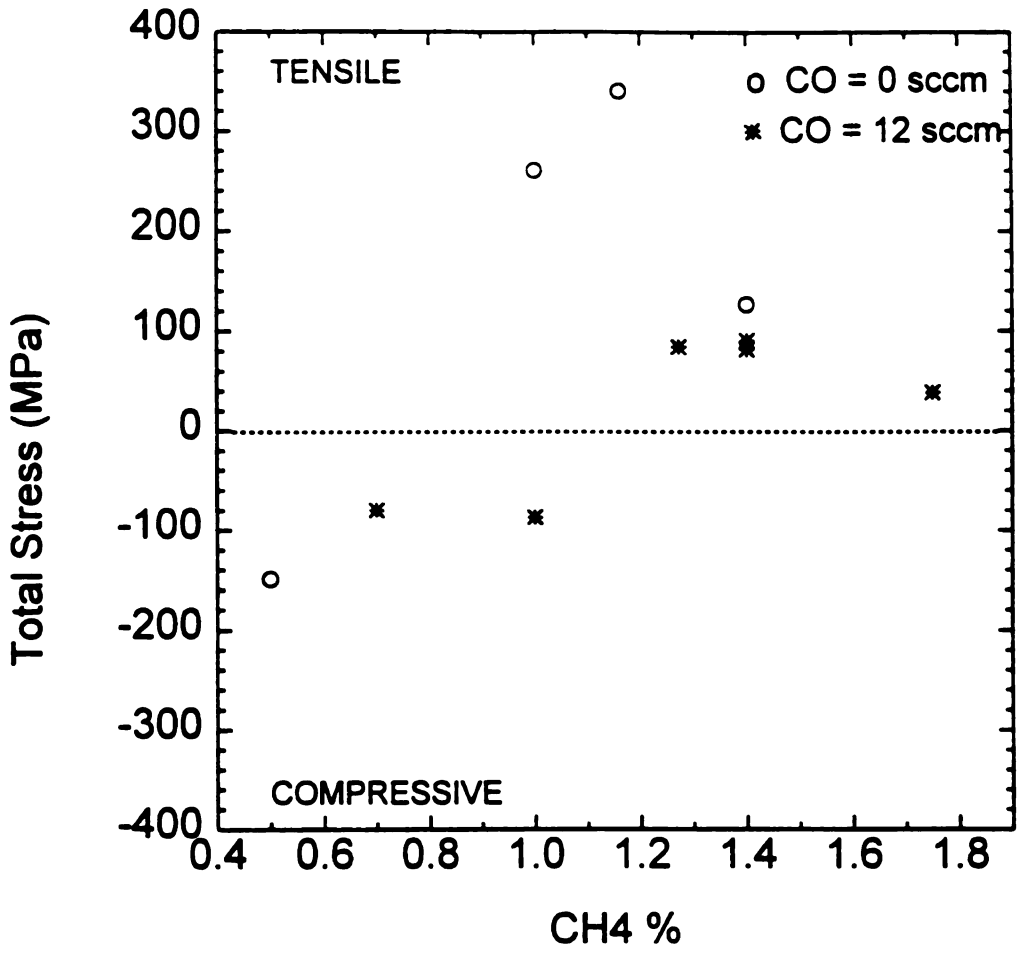

Figure 4.15. Dependence of the total stress on methane concentration. Data points are for CO = 0.0 sccm (open circle) and for CO = 12 sccm (*).

maximum value of 460 MPa at 0.2 % methane, and decreases with increasing methane concentration. They have also observed that the total stress converts from tensile to compressive at about 1.5 % and remains compressive up to 3 % methane.

The inconsistency between our result and their result may be due to the method of deposition, the deposition temperature and the film structure.

4.6 Summary

The feasibility of fabricating diamond-based sensors has been demonstrated. Fabrication details of micromechanical structures such as cantilever beams, bridges, and membranes with different dimensions and shapes were described. The selectivity of deposited boron doping layers on undoped diamond films using low temperature oxide as doping mask was presented. For metalization of diamond devices, wet chemical etching solution was developed to pattern Pt/Ti double structure. Total stress in the diamond film was measured and presented.

CHAPTER 5

Measurement Techniques

5.1 Introduction

The experimental apparatus and techniques used to characterize the piezoresistive effect of p-type polycrystalline CVD diamond thin films are described in this chapter. Two systems for gauge factor measurements were used, one using a simple plate bending system and another using cantilever bending system. The difference between the two techniques is explained in this chapter.

5.2 Plate Bending System

This system was used previously to characterize the piezoresistive effect for ion-implanted p-type layer in silicon [31]. Fig. 5.1 shows a schematic diagram for the plate bending system. The sample was cut from the wafer in a rectangular shape (1 cm x 1.5 cm) and mounted to a stainless steel plate (2.5 cm x 7.5 cm), using epoxy (cured for 2 h at 150 °C). A wire strain gauge (R=350 Ohms, GF=2.07) was mounted on the top of the silicon sample next to and parallel to the diamond piezoresistor using special glue (3M610, cured for 1 h at 150 °C). The purpose of the wire strain gauge is to calculate directly the strain induced on the silicon surface, by measuring the

resistance changes using a digital multimeter (HP 3468A Multimeter). The stainless steel plate is bent in flexure over a pivoting cylindrical surface. As illustrated in Figure 5.1, the stress was applied by two parallel forces. Thus inducing tensile strain at the surface of the plate.

Only preliminary measurement was done using this technique. The result of this measurement is described in chapter 6. In this method, only the tensile strain was measured. It was not easy to apply a compressive strain (the silicon sample touched the pivot by flipping the plate up side down). Also, it was not easy to apply a uniform and uniaxial strain (the application of two equal forces at both ends of the plate was not easy). Therefore, a new technique was developed in this work to measure and characterize the piezoresistive effect of CVD diamond which can be used for measurements of compressive and tensile strain. This technique is described in the following section.

5.3 Cantilever Beam Technique

For measurements of the piezoresistive effect, it is necessary to apply uniaxial mechanical strain to the piezoresistors. In order to apply a uniaxial strain (tension or compression) our experiment involved using a silicon sample with dimensions of 7.5x2.5x0.045 cm^3 as a cantilever beam. The beam is clamped in a fixture at one end and a mechanical strain is produced in the beam by applying force at its free end. Fig. 5.2(a) shows a schematic diagram of the cantilever beam method. The strain at a point on the beam can be calculated by a knowledge of the beam geometry and displacement at the free end. The displacement is measured with a micrometer head. The strain was calculated using an expression which is developed in appendix C. The expression for the strain (C.22) is given by

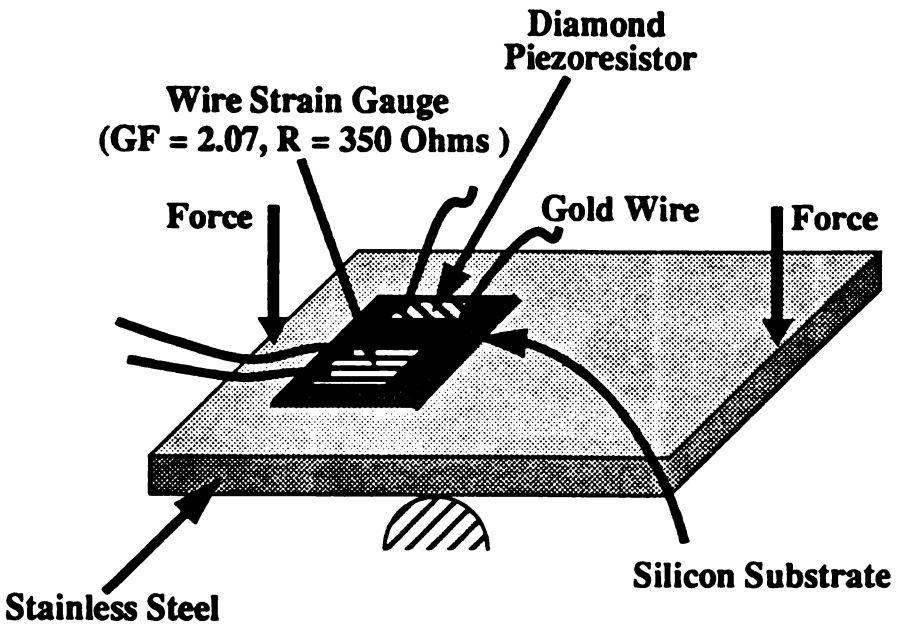

Figure 5.1. Schematic diagram of arrangement for strain measurements by plate bending method.

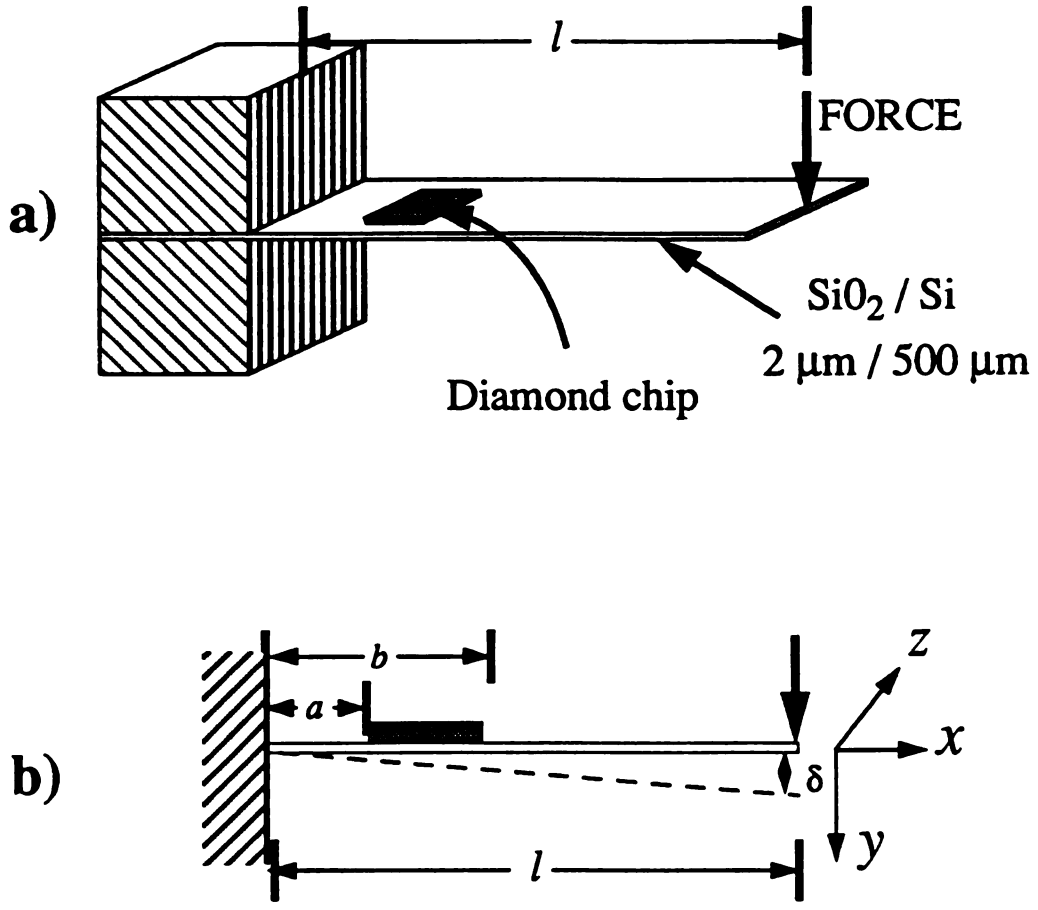

Figure 5.2. Schematic diagram of arrangement for strain measurements of cantilever beam method.

$$\epsilon_x = \frac{3}{2}\frac{h}{l^3}\left[l - \frac{1}{2}(a+b)\right] y, \tag{5.1}$$

where y is the deflection of the beam at the free end, h is the beam thickness, l is the beam length and a and b are the distance of the two terminals of the piezoresistor to the clamped edge of the beam.

The majority of gauge factor measurements were made using the cantilever beam technique. The displacement is measured with a micrometer. By monitoring the resistance of the piezoresistor with a digital multimeter, the gauge factor can be calculated by dividing the relative resistance change by the applied strain. The strain was calculated using equation (5.1). The validity of this method was first checked by using a calibrated metal foil strain gauge (R=350 Ohms, GF=2.07) to determine the actual applied strain. The computed and measured strain were found to differ by less than (10-15)%. Table 5.1 shows the predicted strain and the measured strain.

Table 5.1. Computed and measured strain

Computed Strain (μstrain)	Measured Strain (μstrain)	Variation %
75	68	9.3
155	136	12.2
227	204	10.1
316	272	13.9
403	340	15.6

Comparing the two measurement techniques, the cantilever beam method has some advantage over the plate bending method. In the case of cantilever beam method it was easy to measure strain for both cases of strain (compressive and tensile). The strain was induced uniformly, since only the force that create the stress/strain was

slowly

meth

strain

two

bend

temp

T

ther

piez

sam

mer

In t

the

bet

of

5.

Tw

ad

slowly applied by the micrometer head. However, in the case of the plate bending method two forces were applied at the same time at both ends of the plates. The strain induced by the two forces might be nonuniform, due to difficulty of applying two equal forces. In addition to the above mention problems in the case of plate bending method it was not easy to apply force when measuring the gauge factor at temperatures higher than room temperature.

The temperature dependence of the gauge factor was measured in a chamber thermally controlled, to prevent any effect on the detected change in resistance of the piezoresistor except the desired change. A 1.5 cm x 1.5 cm sample was used. This sample was mounted on the top of stainless steel beam (2 cm x 6 cm x 0.08 cm) in dimension using epoxy. The measurement was done using the cantilever beam method. In this case the beam was placed horizontally instead of being placed vertically as was the case for room temperature measurement. Unfortunately due to adhesive problem between the sample and the beam our measurement was limited to 75 °C. The result of this measurement is described in chapter 6.

5.4 Summary

Two experimental techniques used to measure the gauge factor were presented. The advantages of one technique over the other were also discussed in this chapter.

CHAPTER 6

Piezoresistive Effect of CVD Diamond Films

6.1 Introduction

The piezoresistive effect in CVD diamond was studied for the first time in this work. The results of the piezoresistive effect of CVD diamond films are presented in this chapter. All piezoresistors, used in this study consisted of p-type polycrystalline or homoepitaxial diamond films. Two groups of samples were used for the poly-diamond films measurements. The first group consists of rectangular shaped discrete diamond resistors 500 μm wide and 3 mm long and the second group of piezoresistors were included in a sensor test chip.

6.2 Polycrystalline Diamond Films

As a preliminary experiment, discrete polycrystalline piezoresistors were used. The plate bending method described in section 5.1 of chapter 5 was used to produce strain. Evaporated Al was used for the Ohmic contact to diamond. The sample was cut from the silicon wafer containing the diamond piezoresistors after the metalization step.

The s
and t
in Fi
polyc
relati
for ir
over
adhe
T
6.1(b
of m
four
usin
T
tilev
dian
were
size
the
The
hea
dev
The
a sy

The sample was then mounted in a test fixture (stainless steel plate) using epoxy, and then was deflected as described in chapter 5. The result of this study is shown in Figure 6.1. Figure 6.1(a) shows the fractional change in resistance for p-type polycrystalline diamond film as a function of tensile strain at room temperature. The relative change in resistance of the resistor was nearly linear and reproducible both for increasing and decreasing values of strain. A small hysteresis effect was observed over the range of strains investigated (0-1000 μstrain). This might be due to the adhesive which was used to mount the sample on the stainless steel plate.

The longitudinal gauge factor, computed from these results, is plotted in Fig. 6.1(b). The gauge factor is in the range of 6 to 8. Compared with the majority of metals, the gauge factor of p-type polycrystalline diamond film is about three to four times higher. Following these results more samples were prepared and measured using the cantilever beam technique.

Three groups of samples were used for piezoresistive measurements using the cantilever beam technique. The first group consists of rectangular shaped discrete poly-diamond resistors 500 μm wide and 3 mm long. The second group of piezoresistors were included in an earlier test chip, with a chip area of 1 cm^2 and a minimum feature size of 160 μm, which was used for temperature sensors [120]. Beams were cut from the silicon wafers containing the diamond piezoresistors after the metalization step. The sample was then mounted in a test fixture and deflected using a micrometer head. The strain on the surface of the bending beam was calculated using Eq. (5.1) developed in chapter 5. This equation is rewritten here for convenience.

$$\epsilon = \frac{\frac{3h}{2}\left(l - \frac{a+b}{2}\right)}{l^3} \cdot \delta \tag{6.1}$$

The third group of samples were boron-doped homoepitaxial diamond films grown on a synthetic diamond substrate.

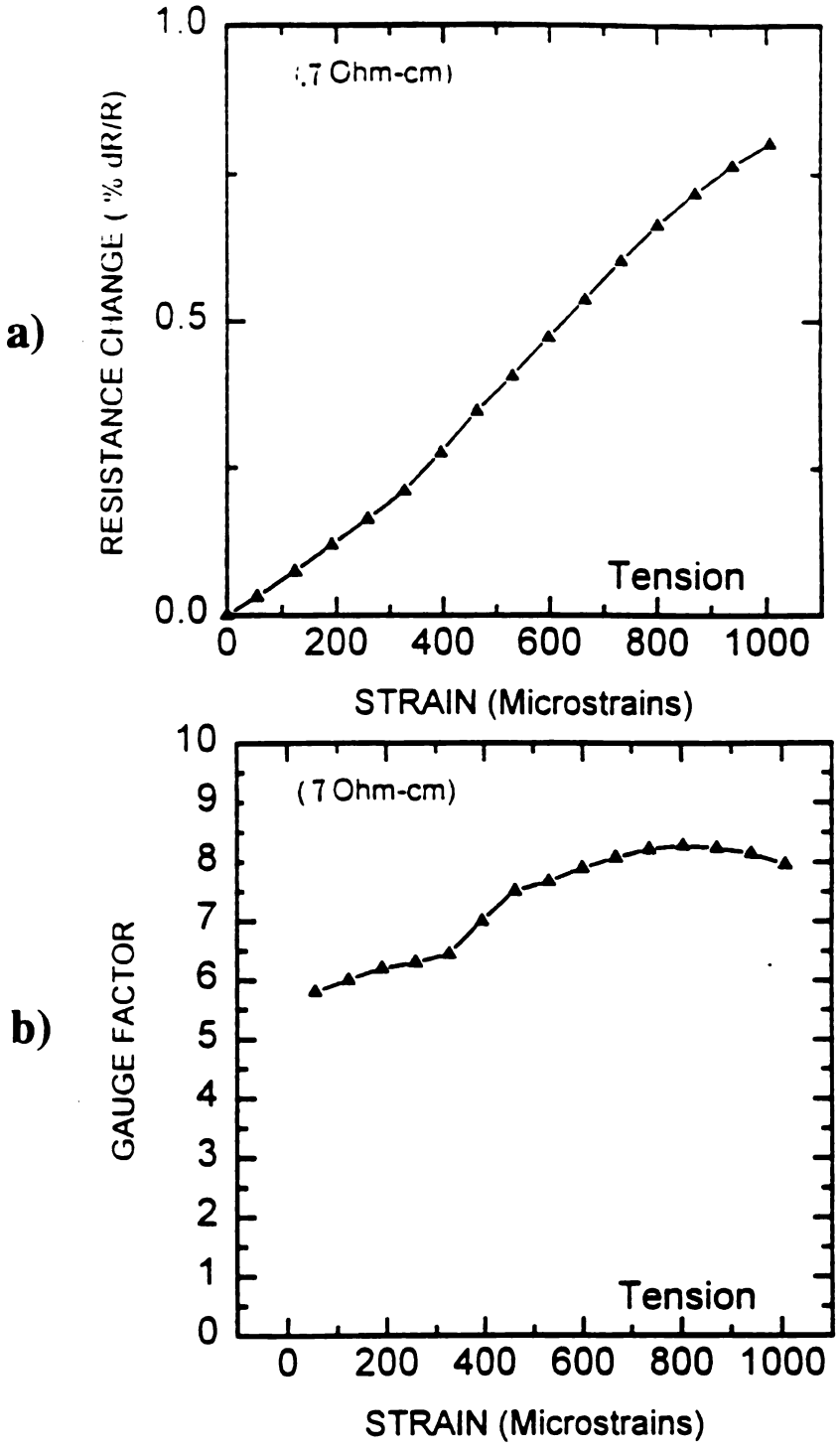

Figure 6.1. Fractional change in resistance (a) and gauge factor (b) as a function of tensile strain in the longitudinal direction.

6.2.1

Sampl
is give

Fig
amon
at roo
pressi
resisti
repro
Figur
sive s
negat
the m
betw
gaug
be ≈

6.2.

The
first
canti
at hi

F
piezo
the s
samp

6.2.1 Doping Dependence

Samples with different resistivities were studied. The result of the doping dependence is given in Figure 6.2.

Figure 6.2(a) shows the fractional change in resistance for the polycrystalline diamond film as a function of tensile and compressive strain for different resistivities at room temperature. The resistance increases with tension and decreases with compression. The slope of the fractional change in resistance increases with increasing resistivity. The fractional change in resistance of the piezoresistors was nearly linear, reproducible and no hysteresis was observed over the range of strains investigated. Figure 6.2(b) shows the longitudinal gauge factor as a function of tensile and compressive strain. The gauge factor was found to be positive in the case of tensile strain and negative in the case of compressive strain. As expected for a typical semiconductor, the magnitude of the gauge factor increases with increasing resistivity. Gauge factors between 7 and 20 were observed, depending on doping concentration. The transverse gauge factor was also measured for some samples. For the 20 Ω-cm, it was found to be ≈-2.5.

6.2.2 Temperature Dependence

The dependence of the piezoresistance on the temperature was also studied for the first time in this work. Since the diamond sample was epoxied on a stainless steel cantilever beam, the temperature range was limited to ≈60 °C. Epoxy became soft at higher temperatures, thus strain did not transfer to the sample.

Figure 6.3 shows the fractional change in resistance of a polycrystalline diamond piezoresistor as a function of strain at four different temperatures. The resistivity of the sample is 5 Ω-cm. The fractional change in resistance and the gauge factor of this sample at room temperature are shown in Fig. 6.2(a) and Fig. 6.2(b), respectively.

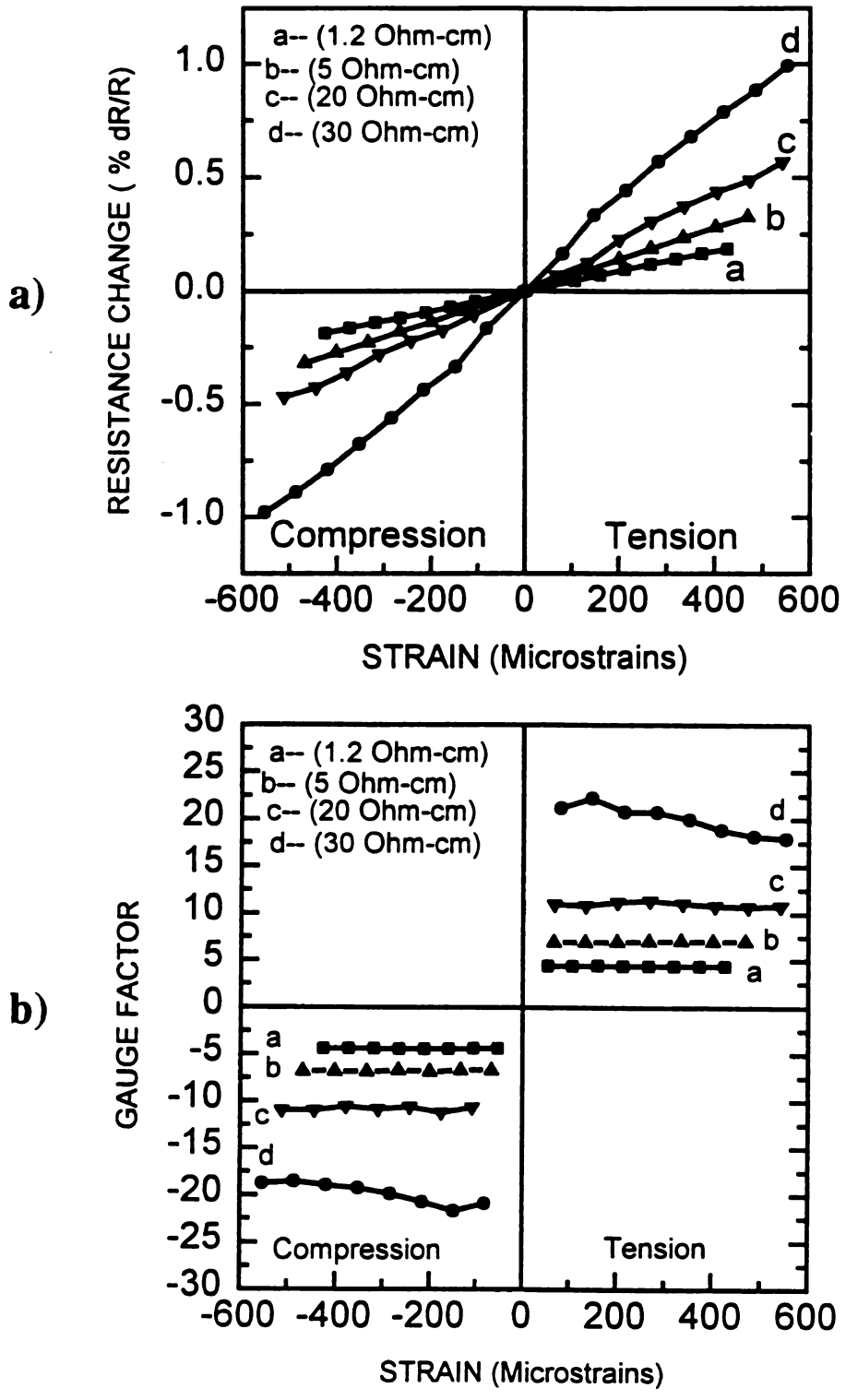

Figure 6.2. Doping dependence of piezoresistance; fractional resistance change (a) and gauge factor (b) as a function of strain, in the longitudinal direction.

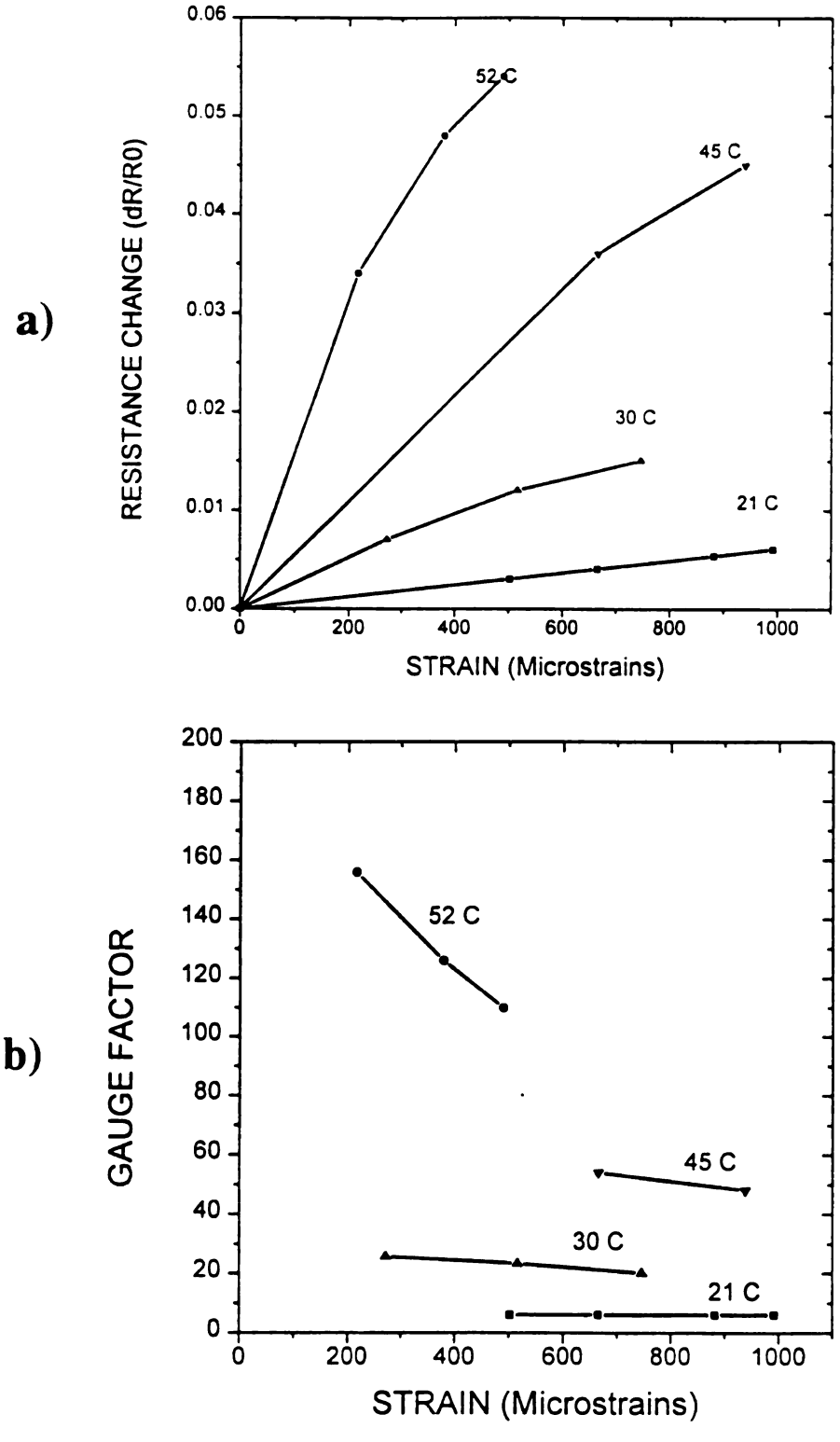

Figure 6.3. Fractional change in resistance of a polycrystalline p-type diamond piezoresistor (a) and gauge factor (b) as a function of strain at different temperatures.

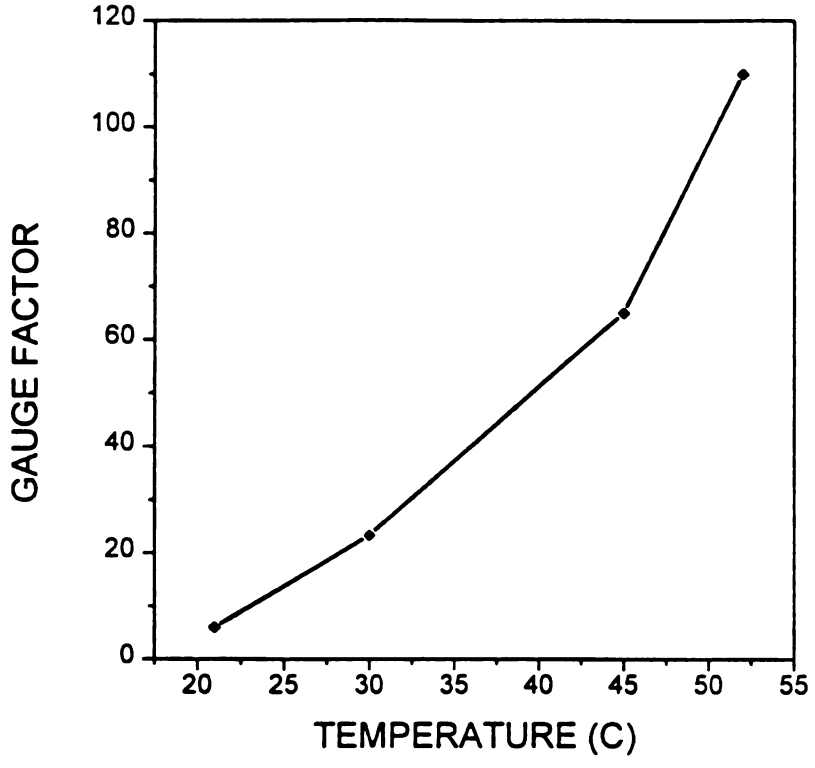

Figure 6.4. Gauge factor as a function of temperature at 500 microstrains in the longitudinal direction.

The measurement was done in the longitudinal direction. Positive tensile strain was applied on this sample.

The temperature dependence of the longitudinal gauge factor for the same sample under tensile strain is shown in Figure 6.4. Figure 6.4(a) shows the gauge factor as a function of strain at different temperatures. Figure 6.4(b) shows the gauge factor as a function of temperature at 500 microstrains. As shown, the gauge factor shows a very strong increase with temperature, and exceeds that of poly-Si above 30 °C and that of single-crystal Si above 50 °C. In contrast, the gauge factor of Si decreases with increasing temperature [42]. No measurement was done on sample with a resistivity higher than 5 Ω-cm. The temperature dependence of the gauge factor was confirmed by other investigators [182].

6.3 Homoepitaxial Diamond Films

For the study of the piezoresistive effect of single-crystal diamond, boron-doped homoepitaxial films were grown by microwave CVD on commercially available type 2a diamond substrates (Dubbelldee Harris Corp., Mt. Arlington, NJ). The diamond samples were epoxied on a stainless-steel cantilever beam. A metal strain gauge could not be mounted on the surface of diamond due to the small size of the samples (4-mm disk or 3-mm squares). Instead, the strain was measured on the surface of the beam. The tensile strain on the diamond surface was estimated using the known elastic properties of the diamond and steel, and the ABAQUS finite-element modeling program (Hibbit, Karlsson and Sorenson, Inc., Providence, RI). For the 4-mm x0.25-mm disk used for this study, the strain in the surface of the diamond was found to be 31% of that in the top of the steel cantilever at the location of the strain gauge. The epoxy was assumed to be a perfect adhesive.

Figure 6.5 (a) shows the fractional change in resistance of the homoepitaxial film

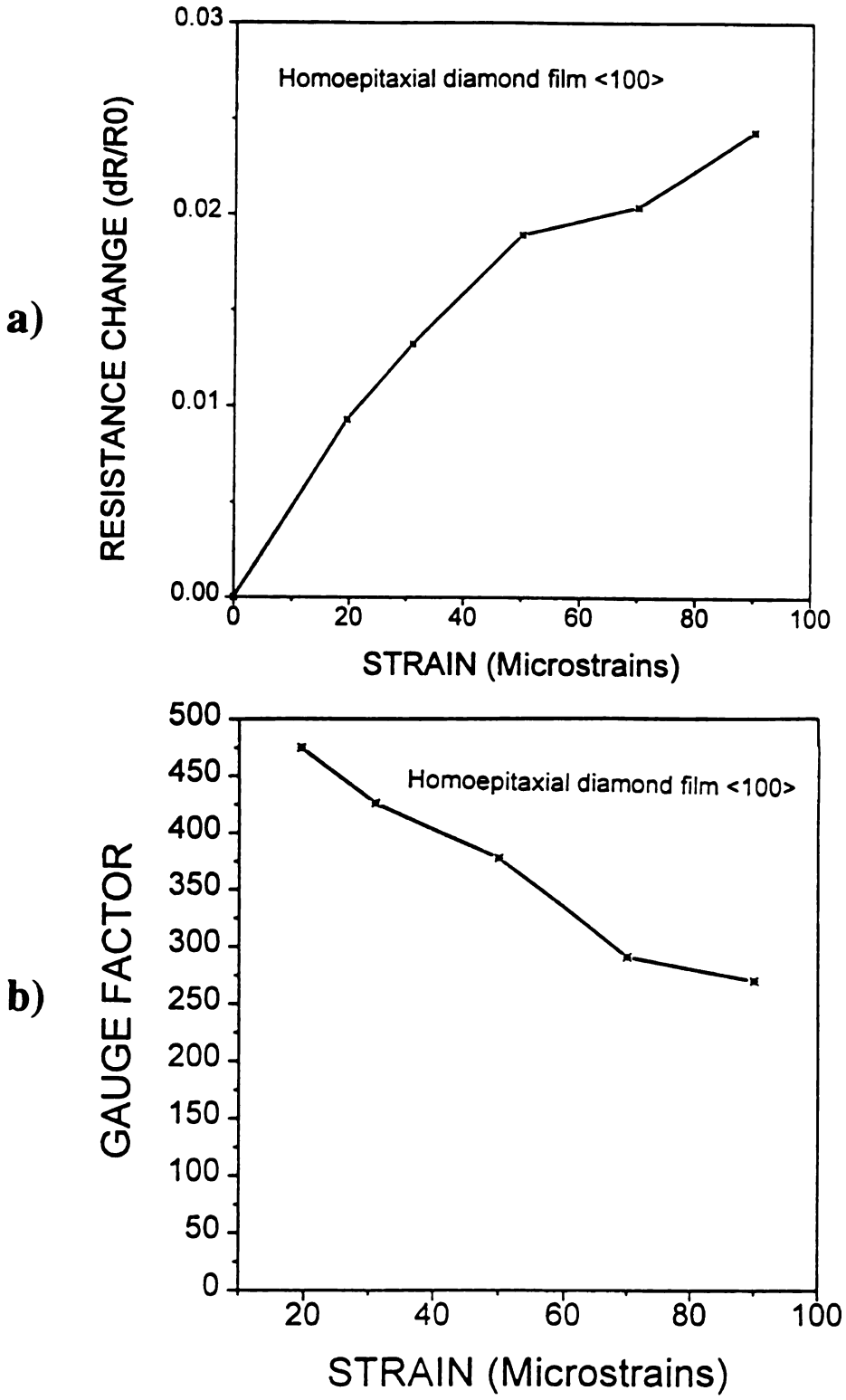

Figure 6.5. Strain dependence of the (a) fractional change in resistance and (b) gauge factor of a (100)-oriented homoepitaxial diamond film.

Table 6.1. Diamond piezoresistance coefficients.

Diamond	ρ (Ω-cm)	Units in 10^{-12} cm^2/dyne		
		π_l	$<\pi_l>$	$<\pi_t>$
Synthetic				
Stress in <100>	N/A	92- 206		
Stress in <111>	N/A	114- 319		
Homoepitaxial <100>	0.03	20- 45		
Polycrystalline	1.2		0.38	
	5		0.58	
	7		0.65	
	20		0.90	- 0.22
	30		1.60	

as a function of tensile strain. Figure 6.6 (b) shows the measured gauge factor as a function of strain. The gauge factor decreases with strain, suggesting that not all the strain is transmitted through the epoxy layer. To partially correct for this, we take the gauge factor to be the value obtained by extrapolating back to zero strain. Even this corrected value should be taken as a lower limit to the actual gauge factor. With these uncertainties, the gauge factor measured in the [100] direction in a (100)-oriented homoepitaxial p-type diamond film is at least 550 at room temperature.

6.4 Diamond piezoresistance coefficients

The average longitudinal piezoresistive coefficient $< \pi_l >$ for the polycrystalline film was calculated using equation (2.19) which was derived in Chapter 2, and is given by

$$< \pi_l > \; = \; GF_{il} \frac{1}{Y} \tag{6.2}$$

The results are shown in Table 6.1. As shown $< \pi_l >$ is in the range of (0.38 - 1.6) x10^{-12} cm^2/dyne depending on the resistivity. The average transverse piezoresistive coefficient was also calculated using equation (2.20) derived in Chapter 2 and is given by

$$< \pi_t > \; = \; GF_{it} \frac{1}{Y} \tag{6.3}$$

It is found to be $\approx$ - 0.22 x10^{-12} cm^2/dyne.

The longitudinal piezoresistive coefficient π_l of the homoepitaxial diamond film was calculated using Eq. (2.21).

$$\pi_l \; = \; S_{11} \, GF_{al} \tag{6.4}$$

It was found to be $\approx$ 45 x10^{-12} cm^2/dyne and 20 x10^{-12} cm^2/dyne for low strain (28 μstrain) and high strain (140 μstrain) regions, respectively. Table 6.1 present the result of the longitudinal piezoresistive coefficient for polycrystalline and homoepitaxial diamond films.

The effect of pressure on the HPHT p-type synthetic diamond doped with boron was previously investigated by Russian workers [175, 176]. Their work was described in Chapter 2. The original plots were also shown in Chapter 2. In their paper, they reported neither the gauge factors nor the piezoresistance coefficients. However, in this work we estimated the piezoresistive coefficients and gauge factors from their curves.

The plot was enlarged first then printed out on scale paper. Ten data points were read from each curve. The fractional resistance change $\frac{\Delta R}{R_0}$ was calculated. The piezoresistive coefficients were then calculated. The stress was then converted to strain. In the computation of strain from their results, we used a Young's modulus

Table 6.2. Estimated Piezoresistive coefficients and gauge factors of HPHT p-type synthetic diamond.

Stress Direction	Resistance x(10^5 Ω)	Stress (Kg/cm^2)	Stress x10^8 (dyne/cm^2)	$\frac{\Delta R}{R_0}$	π_l x 10^{-12} (cm^2/dyne)	Strain μstrain	Gauge Factor
<100>							
	9	0	0	0		0	
	7.178	1000	9.8067	0.20244	206	82	2472
	6.045	1500	14.710	0.32833	223	123	2678
	5.335	2000	19.6134	0.40722	207	163	2491
	4.400	3000	29.4201	0.51111	173	245	2086
	3.67	4000	39.2268	0.5922	151	326	1816
	3.335	5000	49.0335	0.62944	128	408	1540
	2.933	6000	58.8402	0.67411	114	490	1375
	2.665	7000	68.6469	0.70388	102	572	1230
	2.5025	8000	78.4536	0.72194	92	653	1105
<111>							
	2.8934	0	0	0		0	
	1.9866	1000	9.8067	0.3134	319	81.7	3836
	1.56	1500	14.71	0.4608	313	122.58	3777
	1.26	2000	19.6134	0.56452	287	163.445	3453
	0.8773	3000	29.4201	0.69679	237	245.16	2844
	0.706	4000	39.2268	0.75599	193	326.89	2319
	0.546	5000	49.0335	0.81129	165	408.613	1985
	0.4396	6000	58.8402	0.84806	144	490.335	1730
	0.3653	7000	68.6469	0.8737	127	572.05	1527
	0.3066	8000	78.4536	0.8940	114	653.78	1369

value of 12 x 10^{12}dynes.cm^{-2}. Table 6.2 shows the estimated piezoresistive coefficients and gauge factors.

6.5 Discussion

The results of studies of piezoresistivity in monocrystalline and polycrystalline p-type diamond are summarized in Fig. 6.6. With the exception of synthetic diamond, all the strain values are tensile. The data for monocrystalline (homoepitaxial) and polycrystalline CVD diamond are from our measurements. The results for Si [33] are provided for comparison. It may be pointed out that the curves for synthetic diamond were estimated from the reported pressure dependence of resistivity measured by Latsa et al. [176] who did not provide any information about the degree of accuracy of their results, the doping level of diamond and the gauge factor.

The gauge factor of homoepitaxial diamond, is a factor of 4 higher than the highest value for Si and is an order of magnitude lower than the values shown for synthetic diamond. The lower values of gauge factor for homoepitaxial diamond as compared to synthetic diamond are believed to be due to very low resistivity, defects in the film and due to the measurement problems related to the epoxy used between a 3 mm^2 diamond sample and a cantilever beam [62].

At 300 K, the gauge factor for the polycrystalline diamond film is shown in Figure 6.2(b), is in the ranges of 5 - 20 [183]. Values up to 40 or higher have been found for some doping levels in our recent experiments and up to 100 are reported by other researchers [184]. It was also reported that the gauge factor increases with increasing of the grain size [184]. These relatively low values of gauge factor may be related to grain sizes, grain boundaries and high densities of defects which have been observed in the grain boundaries and within the grains [177]. For polycrystalline semiconductor material, the resistivity of the film can be described by contributions from both the

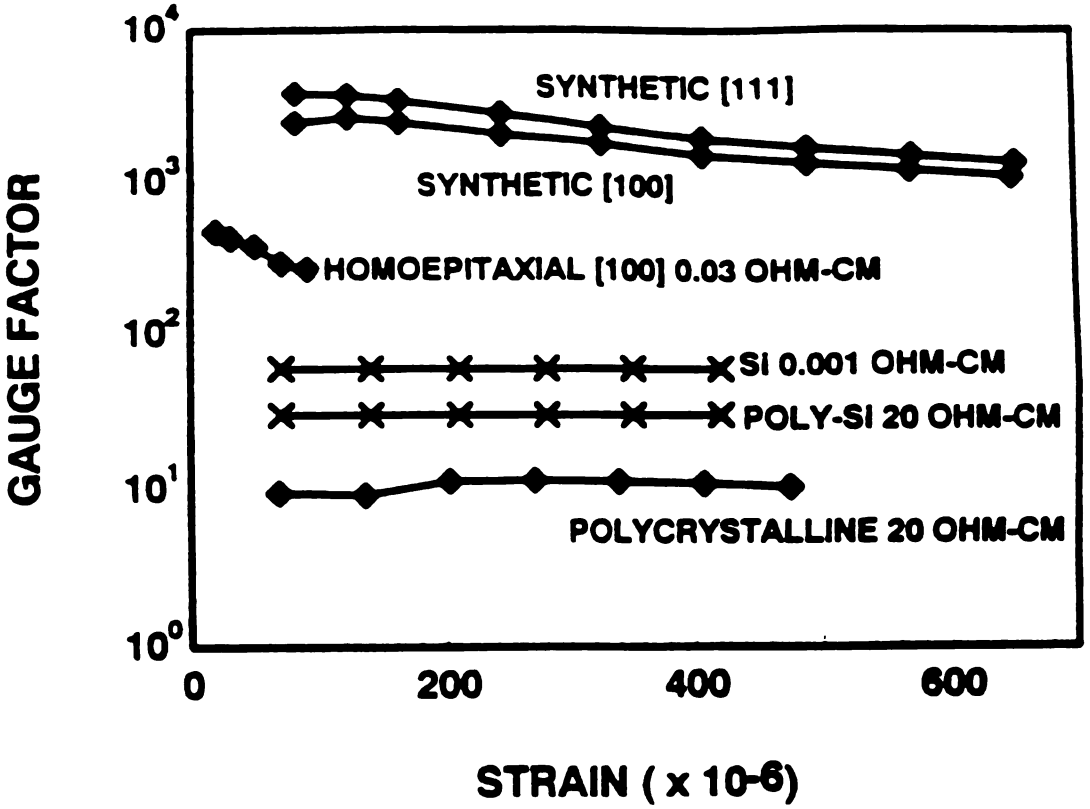

Figure 6.6. Gauge factor of diamond and silicon as a function of strain.

grain and the grain boundary and is given by [44]

$$\rho = \frac{L-(2w+\delta)}{L}\rho_g + \frac{(2w+\delta)}{L}\rho_b \tag{6.5}$$

where ρ, ρ_g and ρ_b are the resistivities of the film, grain and grain boundary, respectively, and δ is the grain boundary thickness. L and w are the lengths of the grain and depletion region, respectively.

From Eq. (6.5) the fractional change in resistivity per unit strain (gauge factor) can be given by:

$$\frac{\Delta\rho}{\rho}\frac{1}{\epsilon} = \frac{L-(2w+\delta)}{L}\frac{\Delta\rho_g}{\rho_g}\frac{1}{\epsilon} + \frac{(2w+\delta)}{L}\frac{\Delta\rho_b}{\rho_b}\frac{1}{\epsilon} \tag{6.6}$$

It was observed that for high doping levels, the electrical properties of polycrystalline silicon approach those of single-crystalline silicon [185]. This is because the effect of the grain boundary is very small (w decreased). This is also true when the grain size of the crystallite is large as compared to the thickness of the grain boundary.

From the temperature dependence of Hall concentration of p-type (B-dopant) polycrystalline diamond film, it was observed that the Hall concentration increases with temperature [125]. The Hall concentration measured at 50 °C, was found to be three times higher than the Hall concentration measured at room temperature. This is because at room temperature $< 1\%$ impurities are ionized. Thus, the effect of crystallites on the conductivity of the diamond film is increased and the effect of the grain boundary on the conductivity of the polycrystalline diamond film is decreased or could be negligible. Equation (6.6) can now be given by

$$\frac{\Delta\rho}{\rho}\frac{1}{\epsilon} = \frac{L-(2w+\delta)}{L}\frac{\Delta\rho_g}{\rho_g}\frac{1}{\epsilon} \tag{6.7}$$

Therefore, the increase of the gauge factor with temperature might be mainly due to

the bulk crystallites.

6.5.1 Energy Band and Qualitative Model

Due to difficulties in producing n-type CVD diamond films piezoresistive data for n-type diamond is not available. Consequently, our qualitative discussion of the piezoresistive effect is limited only to p-type diamond. The qualitative model is based on studies of the energy band structure of diamond [140, 186].

The energy band structure of diamond [140] is shown in Fig. 6.7. A simplified band diagram of diamond valence band is shown in Fig. 6.8(a) for zero stress. The heavy hole band with an effective mass of $m^*_{hh} = 2.18\ m_0$ and light hole band with an effective mass $m^*_{lh} = 0.7\ m_0$ [186] are degenerate at $k = 0$, where m_0 is the free electron mass. The split-off band with an effective mass $m^*_{sh} = 1.06\ m_0$ is separated from the degenerate bands only by 6 ± 1 meV due to spin-orbit interaction. Since the separation is small, the valence band is nearly tripled degenerate in energy. Since, the valence band structures of p-type silicon and diamond are similar to a certain degree, the discussion of the former can be extended carefully to the later.

In the case of Si, the energy separation between the degenerate bands and the split-off is $\approx$ 44 meV and is usually neglected in the discussion of stress -induced changes in the valence band. Following a similar discussion for diamond it is assumed that, for a qualitative discussion, only the changes in the heavy and light hole bands play a dominant role in the stress -induced change of resistivity of diamond. When a uniaxial positive stress (tension) is applied in the longitudinal direction, the heavy hole band E_{Vhh} moves up relative to the light hole band E_{Vlh} (Fig. 6.8(b)). This results in an increase in the number of the heavy holes and a decrease in the number of the light holes. Consequently, the resistivity increases. The compressive stress (negative) causes the light hole band to move up w.r.t the heavy hole band resulting a decrease in resistivity.

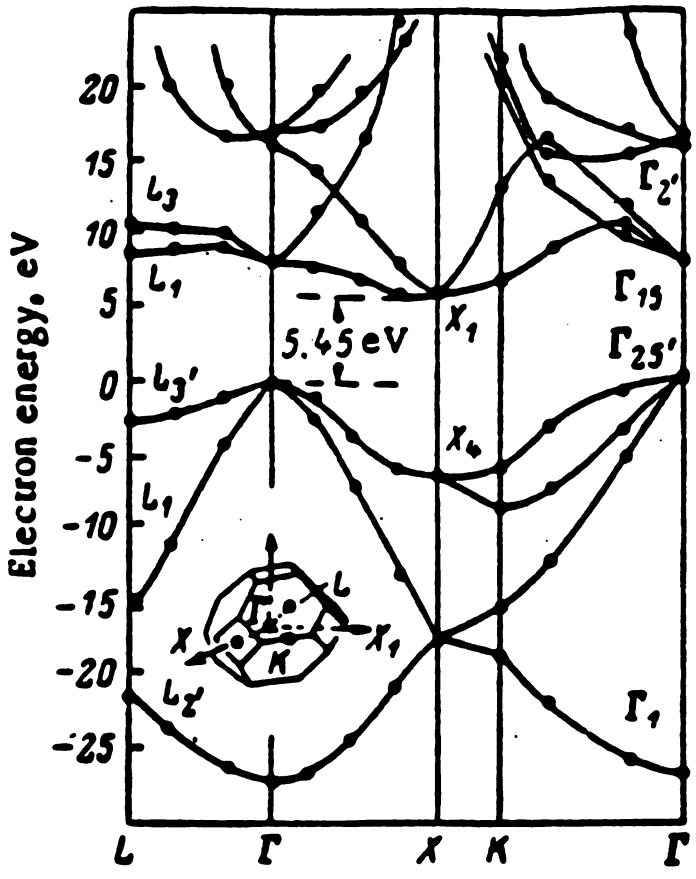

Figure 6.7. Energy band structure of diamond.

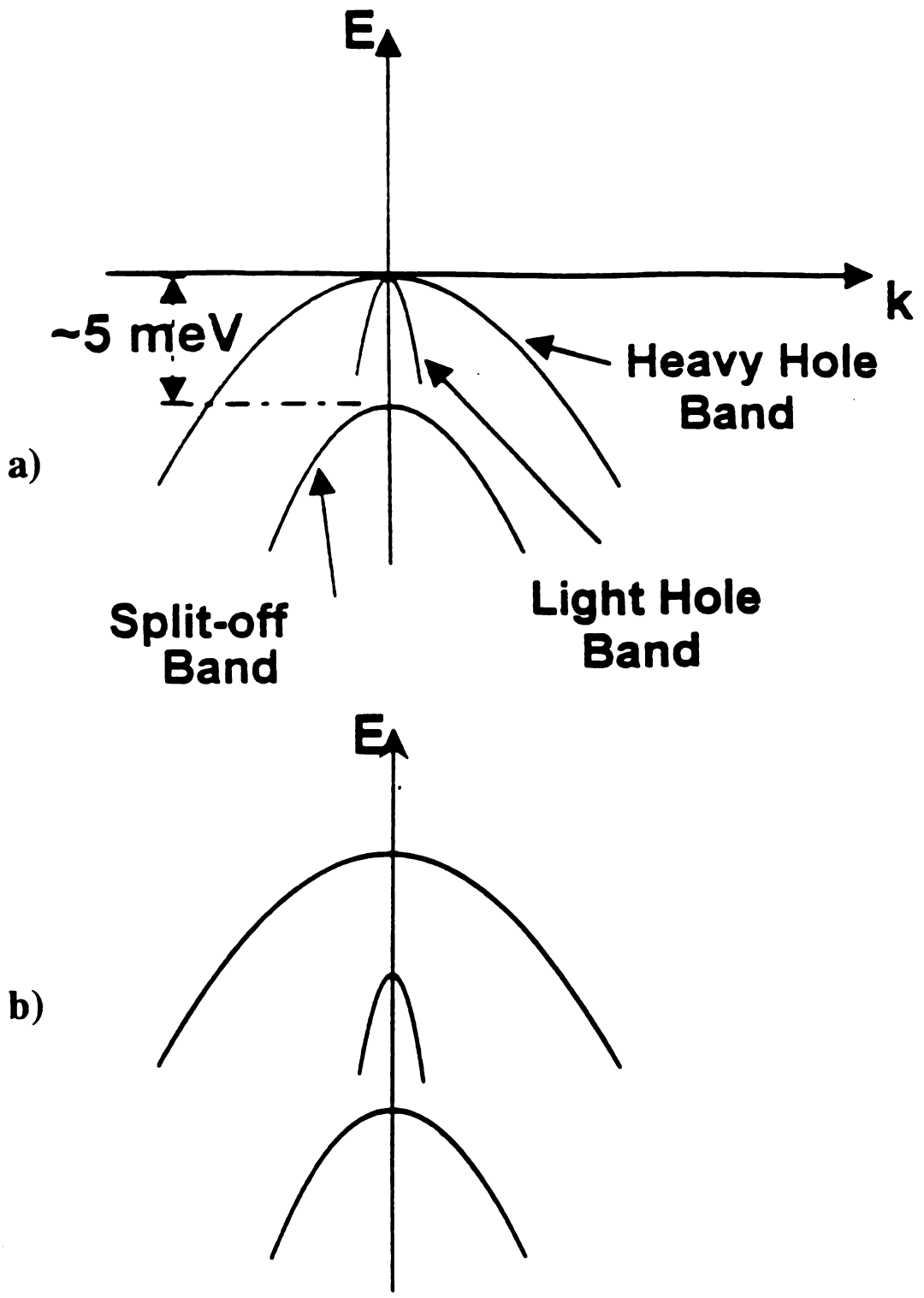

Figure 6.8. A simplified band diagram of diamond valance band; (a) zero stress (b) under uniaxial stress.

In the above discussion, only the relative shifting of subbands is considered. The direct changes in effective mass may also occur if the stress causes a change in the curvature of the subbands. The stress-induced changes in the band gap, as suggested Latsa et al. [176], seem less likely because of large band gap (5.5 eV) of diamond. Since in the case of diamond Λ is $\approx 6 \pm 1$ meV, and the effective mass is not small, the effect of uniaxial stress on split-off subband may be appreciable.

6.6 Summary

The piezoresistive effect in both polycrystalline and homoepitaxial CVD diamond films was studied and presented in this chapter. The piezoresistive gauge factors, measured at 300 °K are in the ranges of 200 - 550 and 6 - 25 for homoepitaxial and polycrystalline p-type diamond films, respectively. The gauge factor for polycrystalline films decreases with decreasing resistivity but increases with increasing temperature. Although the piezoresistivity in diamond is not well understood, the high gauge factor of diamond films demonstrates superiority of diamond sensors over Si or SiC counterparts. The diamond piezoresistive sensors are appropriate for applications in chemically/radiation harsh environments, especially at elevated temperatures.

CHAPTER 7

Summary and Future Research

The aim of this thesis has been to investigate the piezoresistive effect in CVD diamond film deposited by chemical vapor deposition method and to demonstrate the feasibility of CVD diamond for piezoresistive sensor applications. To our knowledge, the piezoresistive effect of diamond film was not investigated at all before this work. Owing to the originality of this work a full characterization was required. The effects of processing parameters on the quality of the diamond film was first investigated and the results were presented in chapter 3.

A multisensor microchip was designed and fabricated. The feasibility of diamond as piezoresistive sensor material was demonstrated by fabricating a very small micromechanical structures. The minimum feature size was 5 μm.

The piezoresistive effect was characterized by measuring the gauge factor as a function of resistivity and temperature. Gauge factor was found to be in the range of 6 to 20 depending on the resistivity of the polycrystalline diamond film. The gauge factor was found to increase with increasing resistivity. The temperature dependence for piezoresistive diamond film was investigated between room temperature and 52 °C. An increase of the gauge factor with temperature was observed. The gauge factor of homoepitaxial diamond film was also measured in this work.

The piezoresistive coefficients of polycrystalline diamond film and homoepitaxial

diamond film were calculated and presented for the first time in this research.

7.1 Future Work

It was mentioned in chapter 6 that the attempt to investigate the piezoresistive effect at high temperature was limited due to epoxy problem. It is very important to investigate the piezoresistive effect at a wider temperature range before the application of this effect in pressure sensor. It was also reported that the gauge factor increases with increasing grain size. Thus, the effect of grain size on the piezoresistive effect need also to be investigated. It was also demonstrated in chapter 4 that a very small micromechanical sensor (pressure and accelerometer) can be fabricated.

APPENDICES

APPENDIX A

Piezoresistive Coefficient

From a mathematical point of view, the effect of homogeneous mechanical stress on the electrical resistance of a conducting crystal can be described generally in terms of a set of constants. These constants are known as the piezoresistance coefficients, the number of which is equal to the number of elastic moduli. The piezoresistance coefficients connect the resistance with stress by equations very much like the equations connecting strain with stress, except for the difference of a factor of 2 in some of the terms. These piezoresistance coefficients have to be determined completely in order to characterize the piezoresistance effect in a conducting crystal.

In order to determine the piezoresistance coefficients in a cubic crystal materials, let us consider first a rectangular coordinate system, with its axes x_1, x_2, and x_3 aligned along the crystallographic axes {100} of the crystal. Fortunately, these coefficients can be determined by the general form of Ohm s's Law.

According to Ohm's Law the relationship between the electric field intensity E_i, the current density J_j and the electrical resistivity ρ_{ij} is given by

$$E_i = \sum_{i=1}^{3} \sum_{j=1}^{3} \rho_{ij} J_j \tag{A.1}$$

Since E_i and J_j are vector quantities, the resistivity components form a second rank

tensor with nine components which is symmetric, that is $\rho_{ij} = \rho_{ji}$. Eq. (A.1) can be written in matrix form as:

$$\begin{bmatrix} E_1 \\ E_2 \\ E_3 \end{bmatrix} = \begin{bmatrix} \rho_{11} & \rho_{12} & \rho_{13} \\ \rho_{12} & \rho_{22} & \rho_{23} \\ \rho_{13} & \rho_{23} & \rho_{33} \end{bmatrix} \cdot \begin{bmatrix} J_1 \\ J_2 \\ J_3 \end{bmatrix} \tag{A.2}$$

In an unstressed symmetrical cubic crystal, the electrical resistivity tensor ρ_{ij} is isotropic, that has only the diagonal components,

$$\rho_{ij} = \rho_0 \, \delta_{ij} \tag{A.3}$$

where δ_{ij} is the Kronecker delta given by:

$$\delta_{ij} = \begin{cases} 0 & \text{if } i \neq j \\ 1 & \text{if } i = j \end{cases}$$

In order to determine the piezoresistance coefficient, it is necessary to assume that the electric field components E_i is a function of the current density J_j, as well as the stress, X_{kl} [24]:

$$E_i = E_i(J_j, X_{kl}) \qquad i,j,k,l = 1,2,3 \tag{A.4}$$

where X_{kl} is described earlier, Expanding E_i as a Taylor series about the state of zero current density $J_{j_0} = 0$, and zero stress X_{kl_0}, Eq. (A.4) will be written as follows:

$$\begin{aligned} dE_i &= \frac{\partial E_i}{\partial J_j} dJ_j + \frac{\partial E_i}{\partial X_{kl}} dX_{kl} \\ &+ \frac{1}{2!}\left[\frac{\partial^2 E_i}{\partial J_j \partial J_m} dJ_j \, dJ_m + \frac{\partial^2 E_i}{\partial X_{kl} \partial X_{no}} dX_{kl} \, dX_{no}\right. \\ &+ \left. 2\frac{\partial^2 E_i}{\partial J_j \partial X_{kl}} dJ_j \, dX_{kl}\right] + \cdots \end{aligned} \tag{A.5}$$

This expression can be reduced by considering that a cubic crystal has a center of symmetry, that is the components of an odd rank tensor vanish [187]. Therefore, the second, third, and fourth terms are identically zero. Eliminating these terms reduces the expression to:

$$dE_i = \frac{\partial E_i}{\partial J_j}\, dJ_j + \frac{\partial^2 E_i}{\partial J_j \partial X_{kl}}\, dJ_j\, dX_{kl} \tag{A.6}$$

where

$$\frac{\partial E_i}{\partial J_j} = \rho_{ij} = \text{resistivity components}$$

and

$$\frac{\partial^2 E_i}{\partial J_j \partial X_{kl}} = \pi_{ijkl} = \text{piezoresistance components}$$

Eq. (A.6) can now be written as:

$$dE_i = \rho_{ij}\, dJ_j + \pi_{ijkl}\, dJ_j\, dX_{kl} \tag{A.7}$$

The integration of Eq. (A.7) is expressed as:

$$\int_0^{E_i} dE_i = \int_0^{J_j} \rho_{ij}\, dJ_j + \int_{(0,0)}^{(J_j, X_{kl})} \pi_{ijkl}\, dJ_j\, dX_{kl} \tag{A.8}$$

Using Eq. (A.3) and considering that all components of π_{ijkl} tensor are constants, Eq. (A.8) gives

$$E_i = \rho_0\, \delta_{ij}\, J_j + \pi_{ijkl}\, J_j\, X_{kl} \tag{A.9}$$

In general, the π_{ijkl} term in equation (A.9) forms a fourth-rank tensor with eighty-one components. Since, the resistivity ρ_{ij} and the stress X_{kl} tensors are symmetric, that is the subscripts corresponding to the electric field and current density directions i and j can be interchanged with each other, and the subscripts corresponding to the

stress directions k and l can be interchanged with each other resulting,

$$\pi_{ijkl} = \pi_{jikl} = \pi_{ijlk} = \pi_{jilk}$$

Therefore, these number can be reduced to a thirty-six independent components. It can be shown that the i and j as a pair can be interchanged with the k and l as a pair resulting in only 21 components

$$\pi_{ijkl} = \pi_{klji}$$

Now, like the stiffness tensor, by using *matrix notation* and by the use of crystal symmetry, only three independent coefficients are required to determine the piezoresistive property of cubic crystal[17].

Further reduction also can be done by factoring out the zero stress resistivity ρ_0, and to introduce a factor 2 only to those coefficients whose second subscript is a 4, 5, or 6, which are those associated with shear stresses (because each single subscript shear stress is twice the corresponding tensor components), these are denoted as follows [17]:

$$\begin{aligned} \rho_0\pi_{11} &= \pi_{iiii} \\ \rho_0\pi_{12} &= \pi_{iijj} \\ \rho_0\pi_{44} &= 2\pi_{ijij} \end{aligned}$$

Thus the piezoresistive coefficients can be written as a 6 x 6 matrix which has three independent components for crystals of the diamond structures such as silicon, ger-

manium and diamond [17].

$$\begin{bmatrix} \pi_{1111} & \pi_{1122} & \pi_{1122} & 0 & 0 & 0 \\ \pi_{1122} & \pi_{1111} & \pi_{1122} & 0 & 0 & 0 \\ \pi_{1122} & \pi_{1122} & \pi_{1111} & 0 & 0 & 0 \\ 0 & 0 & 0 & 2\,\pi_{2323} & 0 & 0 \\ 0 & 0 & 0 & 0 & 2\,\pi_{2323} & 0 \\ 0 & 0 & 0 & 0 & 0 & 2\,\pi_{2323} \end{bmatrix} = \rho_0 \begin{bmatrix} \pi_{11} & \pi_{12} & \pi_{12} & 0 & 0 & 0 \\ \pi_{12} & \pi_{11} & \pi_{12} & 0 & 0 & 0 \\ \pi_{12} & \pi_{12} & \pi_{11} & 0 & 0 & 0 \\ 0 & 0 & 0 & \pi_{44} & 0 & 0 \\ 0 & 0 & 0 & 0 & \pi_{44} & 0 \\ 0 & 0 & 0 & 0 & 0 & \pi_{44} \end{bmatrix} \tag{A.10}$$

where the $\pi_{11}, \pi_{12}, \text{and} \pi_{44}$ are the fundamental piezoresistance coefficients of the crystals.

Finally, after the substitution the right-hand side of Eq. (A.10) into Eq. (A.9), the three piezoresistance equations specialized to materials of diamond crystal structures can be written as

$$\begin{aligned} \frac{E_1}{\rho_0} &= J_1[1 + \pi_{11}X_1 + \pi_{12}(X_2 + X_3)] + \pi_{44}(J_2X_6 + J_3X_5) \\ \frac{E_2}{\rho_0} &= J_2[1 + \pi_{11}X_2 + \pi_{12}(X_1 + X_3)] + \pi_{44}(J_1X_6 + J_3X_4) \\ \frac{E_3}{\rho_0} &= J_3[1 + \pi_{11}X_3 + \pi_{12}(X_1 + X_2)] + \pi_{44}(J_1X_5 + J_2X_4) \end{aligned} \tag{A.11}$$

When stress and current density are both in the x_1 direction, $X_i = 0$ for $i \neq 1$, and $E_2 = E_3 = 0$. Eq. (A.11) reduced to

$$\frac{E_1}{\rho_0} = J_1[1 + \pi_{11}\, X_1] \tag{A.12}$$

which yields

$$\frac{\rho - \rho_0}{\rho_0} = \pi_{11}\, X_1 \tag{A.13}$$

with

$$\frac{E_1}{J_1} = \rho. \tag{A.14}$$

In an arbitrary coordinate system where the coordinate axes x'_1, x'_2, and x'_3 do not coincide with the crystallographic axes x_1, x_2, x_3 of the cubic crystal, the piezoresistance equations (A.11) will be derived according to the following transformation [30, 188].

$$\begin{bmatrix} x'_1 \\ x'_2 \\ x'_3 \end{bmatrix} = \begin{bmatrix} l_1 & m_1 & n_1 \\ l_2 & m_2 & n_2 \\ l_3 & m_3 & n_3 \end{bmatrix} \cdot \begin{bmatrix} x_1 \\ x_2 \\ x_3 \end{bmatrix} \tag{A.15}$$

where l_i, m_i, and n_i (i = 1,2,3) are the direction cosines of the primed axes x'_i with respect to the crystal axes x_i, that is, cosines of the angle between the axes of the arbitrary coordinate system with the crystallographic axes [25]. Also, Eq. (A.15) can be used to transform from the new coordinate system back to the old coordinate system, which can be written as:

$$\begin{bmatrix} x_1 \\ x_2 \\ x_3 \end{bmatrix} = \begin{bmatrix} l_1 & l_2 & l_3 \\ m_1 & m_2 & m_3 \\ n_1 & n_2 & n_3 \end{bmatrix} \cdot \begin{bmatrix} x'_1 \\ x'_2 \\ x'_3 \end{bmatrix} \tag{A.16}$$

The general matrix of direction cosines can be expressed in terms of Euler's angles (θ , ϕ and ψ) (See Fig. A.1) as follows:

$$\begin{bmatrix} l_1 & m_1 & n_1 \\ l_2 & m_2 & n_2 \\ l_3 & m_3 & n_3 \end{bmatrix} = \begin{bmatrix} c\phi c\theta c\psi - s\phi s\psi & s\phi c\theta c\psi + c\phi s\psi & -s\theta c\psi \\ -c\phi c\theta s\psi - s\phi c\psi & -s\phi c\theta s\psi + c\phi c\psi & s\theta s\psi \\ c\phi s\theta & s\phi s\theta & c\theta \end{bmatrix} \tag{A.17}$$

where $c\phi \equiv \cos\phi$, $s\theta \equiv \sin\theta$, etc.

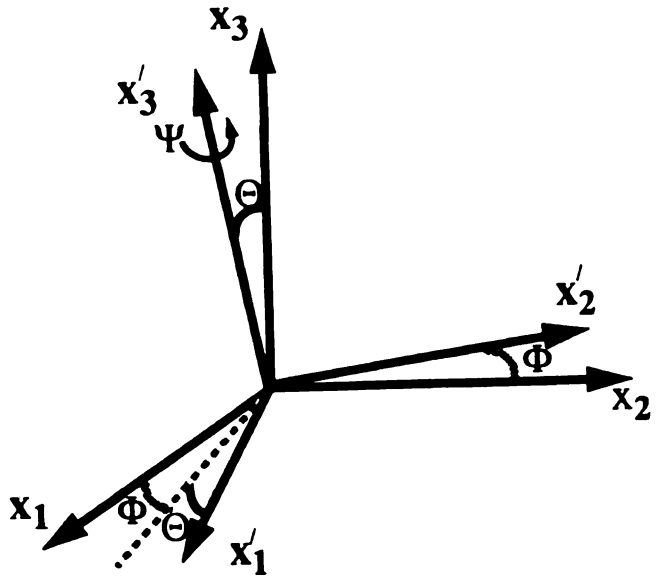

Figure A.1. Euler's angles used for axis rotation.

All the components of equations (A.11) in the crystallographic system need to be transformed to the rectangular coordinate system.

The current density components in the crystallographic coordinate system in terms of the primed coordinate system become:

$$\begin{aligned} J_1 &= l_1 \acute{J}_1 + l_2 \acute{J}_2 + l_3 \acute{J}_3 \\ J_2 &= m_1 \acute{J}_1 + m_2 \acute{J}_2 + m_3 \acute{J}_3 \\ J_3 &= n_1 \acute{J}_1 + n_2 \acute{J}_2 + n_3 \acute{J}_3 \end{aligned} \tag{A.18}$$

The old components of the normal stress X_i, (i=1,2,3) in terms of the new can be written as [187]

$$\begin{aligned} X_1 &= l_1^2 \acute{X}_1 + l_2^2 \acute{X}_2 + l_3^2 \acute{X}_3 + 2(l_2 l_3 \acute{X}_4 + l_1 l_3 \acute{X}_5 + l_1 l_2 \acute{X}_6) \\ X_2 &= m_1^2 \acute{X}_1 + m_2^2 \acute{X}_2 + m_3^2 \acute{X}_3 + 2(m_2 m_3 \acute{X}_4 + m_1 m_3 \acute{X}_5 + m_1 m_2 \acute{X}_6) \\ X_3 &= n_1^2 \acute{X}_1 + n_2^2 \acute{X}_2 + n_3^2 \acute{X}_3 + 2(n_2 n_3 \acute{X}_4 + n_1 n_3 \acute{X}_5 + n_1 n_2 \acute{X}_6) \end{aligned} \tag{A.19}$$

The old shear stress components X_i, (i=4,5,6) in terms of the new, can be written as [187]

$$\begin{aligned}
X_4 &= m_1 n_1 \acute{X}_1 + m_2 n_2 \acute{X}_2 + m_3 n_3 \acute{X}_3 + (m_2 n_3 + m_3 n_2)\acute{X}_6 \\
&+ (m_1 n_3 + m_3 n_1)\acute{X}_5 + (m_1 n_2 + m_2 n_1)\acute{X}_4 \\
X_5 &= l_1 n_1 \acute{X}_1 + l_2 n_2 \acute{X}_2 + l_3 n_3 \acute{X}_3 + (l_2 n_3 + l_3 n_2)\acute{X}_6 \\
&+ (l_1 n_3 + l_3 n_1)\acute{X}_5 + (l_1 n_2 + l_2 n_1)\acute{X}_4 \\
X_6 &= l_1 m_1 \acute{X}_1 + l_2 m_2 \acute{X}_2 + l_3 m_3 \acute{X}_3 + (l_2 m_3 + l_3 m_2)\acute{X}_6 \\
&+ (l_1 m_3 + l_3 m_1)\acute{X}_5 + (l_1 m_2 + l_2 m_1)\acute{X}_4
\end{aligned} \tag{A.20}$$

Substitution equations (A.18), (A.19) and (A.20) into (A.11) gives

$$\begin{aligned}
\frac{E_1}{\rho_0 \acute{J}_1} &= l_1[1 + \acute{X}_1[\pi_{11} l_1^2 + (\pi_{12} + \pi_{44})(m_1^2 + n_1^2)]] \\
\frac{E_2}{\rho_0 \acute{J}_1} &= m_1[1 + \acute{X}_1[\pi_{11} m_1^2 + (\pi_{12} + \pi_{44})(l_1^2 + n_1^2)]] \\
\frac{E_3}{\rho_0 \acute{J}_1} &= n_1[1 + \acute{X}_1[\pi_{11} n_1^2 + (\pi_{12} + \pi_{44})(m_1^2 + l_1^2)]]
\end{aligned} \tag{A.21}$$

The electric field components in the prime coordinate system are given by:

$$\begin{aligned}
\acute{E}_1 &= l_1 E_1 + m_1 E_2 + n_1 E_3 \\
\acute{E}_2 &= l_2 E_1 + m_2 E_2 + n_2 E_3 \\
\acute{E}_3 &= l_3 E_1 + m_3 E_2 + n_3 E_3
\end{aligned} \tag{A.22}$$

Now, in the case where the electric field, the current density, and the stress are all in the same direction for example $\acute{x}_1$, which is the longitudinal direction we will obtain

$$\frac{\acute{E}_1}{\rho_0 \acute{J}_1} = \frac{1}{\rho_0 \acute{J}_1}(l_1 E_1 + m_1 E_2 + n_1 E_3) \tag{A.23}$$

substitution Eq. (A.21) into Eq. (A.23) gives

$$\begin{aligned}\frac{\acute{E}_1}{\rho_0 \acute{J}_1} &= (l_1^2 + m_1^2 + n_1^2) + \acute{X}_1[\pi_{11}(l_1^4 + m_1^4 + n_1^4) \\ &+ 2(\pi_{12} + \pi_{44})(l_1^2 m_1^2 + l_1^2 n_1^2 + m_1^2 n_1^2)]\end{aligned} \tag{A.24}$$

Since $(l_1^2 + m_1^2 + n_1^2 = 1)$, and

$$(l_1^4 + m_1^4 + n_1^4) = (l_1^2 + m_1^2 + n_1^2)^2 - 2(l_1^2 m_1^2 + l_1^2 n_1^2 + m_1^2 n_1^2) \tag{A.25}$$

Equation (A.24) becomes

$$\begin{aligned}\frac{\acute{E}_1}{\rho_0 \acute{J}_1} &= 1 + \acute{X}_1[\pi_{11} + 2(\pi_{44} + \pi_{12} - \pi_{11})(l_1^2 m_1^2 + l_1^2 n_1^2 + m_1^2 n_1^2)] \\ &= 1 + \acute{\pi}_{11} \acute{X}_1\end{aligned} \tag{A.26}$$

where $\acute{\pi}_{11}$ is given by [25]

$$\acute{\pi}_{11} = \pi_{11} - 2(\pi_{11} - \pi_{12} - \pi_{44})(l_1^2 m_1^2 + m_1^2 n_1^2 + n_1^2 l_1^2) \tag{A.27}$$

Since $\frac{\acute{E}_1}{\acute{J}_1}$ is the resistivity component $\acute{\rho}_1$ in the $\acute{x}_1$ under the uniaxial stress $\acute{X}_1$, equation (A.26) can be written as

$$\frac{\Delta \acute{\rho}_1}{\rho_0} = \acute{\pi}_{11} \acute{X}_1 \tag{A.28}$$

The derivation of the transverse piezoresistance coefficient $\acute{\pi}_{12}$ (the current and field

are perpendicular to the stress) is analogous to that of π'_{11} and is given by [25]

$$\pi'_{12} = \pi_{12} + (\pi_{11} - \pi_{12} - \pi_{44})(l_1^2 l_2^2 + m_1^2 m_2^2 + n_1^2 n_2^2) \qquad \text{(A.29)}$$

APPENDIX B

Gauge Factor Derivation

The most useful measure of piezoresistive effect is the gauge factor (GF), which is defined as the fractional change in resistance $\frac{\Delta R}{R}$ per unit strain ϵ. The resistance R

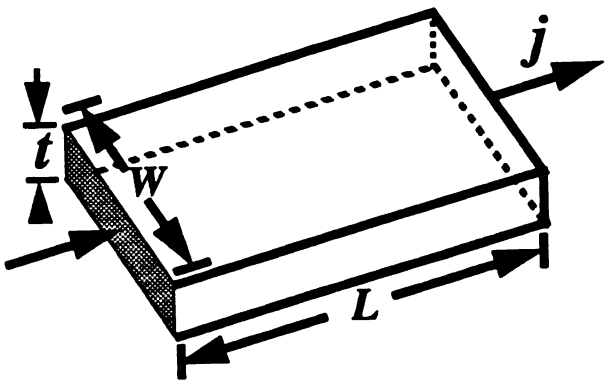

Figure B.1. Thin rectangular resistor.

of a long and thin film made from an isotropic or polycrystalline material with length

L, width w, and thickness t as shown in Fig. B.1, is given by

$$R = \rho \frac{L}{wt} \tag{B.1}$$

The fractional change in resistance can be found by differentiating the logarithm of Eq. (B.1) and the result is

$$\frac{\Delta R}{R} = \frac{\Delta \rho}{\rho} + \frac{\Delta L}{L} - \frac{\Delta w}{w} - \frac{\Delta t}{t} \tag{B.2}$$

The term $\frac{\Delta L}{L}$ is the longitudinal strain ϵ_l and the terms $\frac{\Delta w}{w}$, and $\frac{\Delta t}{t}$ are the transverse strains ϵ_t. Thus equation (B.2) can be written as

$$\frac{\Delta R}{R} = \frac{\Delta \rho}{\rho} + \epsilon_l - \epsilon_t - \epsilon_t \tag{B.3}$$

Now, from Eq. (B.3) the gauge factor in the longitudinal direction (strain parallel to the length) will be written as

$$\begin{aligned} (\mathbf{GF})_l &= (\frac{\Delta R}{R})_l \frac{1}{\epsilon_l} \\ &= (\frac{\Delta \rho}{\rho})_l \frac{1}{\epsilon_l} + 1 - 2\frac{\epsilon_t}{\epsilon_l} \\ &= (\frac{\Delta \rho}{\rho})_l \frac{1}{\epsilon_l} + (1 + 2\nu) \end{aligned} \tag{B.4}$$

where ν is the Poisson's ratio, relating to the reduction in the thickness of the film due to strain, which is defined as the ratio of the transverse strain to the longitudinal strain resulting from the simple tension. As we can see in Eq.(B.4), the change in resistance due to the strain produced by uniaxial stress consists of three terms: The first term represents the change in resistivity due to the strain while the second two terms represent the change in resistance due to dimensional changes caused by the strain.

For the transverse direction where the strain is parallel to the width of the resistor w, $\frac{\Delta w}{w}$ becomes the longitudinal strain ϵ_l and $\frac{\Delta L}{L}$ and $\frac{\Delta t}{t}$ are the transverse strains ϵ_t. Eq. (B.3) can be written as

$$\begin{aligned}(\frac{\Delta R}{R})_t &= (\frac{\Delta \rho}{\rho})_t + \epsilon_t - \epsilon_l - \epsilon_t \\ &= (\frac{\Delta \rho}{\rho})_t - \epsilon_l \end{aligned} \tag{B.5}$$

and the gauge factor in the transverse direction can be written as

$$\begin{aligned}(\mathbf{GF})_t &= (\frac{\Delta R}{R})_t \frac{1}{\epsilon_l} \\ &= (\frac{\Delta \rho}{\rho})_t \frac{1}{\epsilon_l} - 1 \end{aligned} \tag{B.6}$$

Since the Poisson's ratio ν of polycrystalline diamond is less than 0.07 [47, 48] the contribution of the dimensional term is less than 1.14. Therefore, the gauge factor of semiconductor polycrystalline diamond film depends mainly on the resistivity of the material and will be written as

$$\mathbf{GF} = \frac{\Delta \rho}{\rho} \frac{1}{\epsilon_l} \tag{B.7}$$

Now, from Hook's law and equation (A.28) the gauge factor can be written in terms of *Young's modulus* $\mathbf{Y}$ and piezoresistance coefficient π_d

$$\begin{aligned}\mathbf{GF} &= \frac{\Delta \rho}{\rho} \frac{1}{\epsilon_l} \\ &= \pi_d \mathbf{Y} \end{aligned} \tag{B.8}$$

where the subscript $d = l$ in the longitudinal direction and $d = t$ in the transverse direction.

In the general case, within an anisotropic homogeneous material, it is often desirable to define elastic modulus as is common in isotropic media [189]. For uniaxial stress $\acute{X}_1$ in the $\acute{i}$ direction, the *Young's modulus* **Y** is given by

$$\mathbf{Y} = \frac{1}{s'_{ii}} \tag{B.9}$$

and the Poisson's ratio is given by

$$\begin{aligned} \nu'_{ij} &= -\frac{s'_{ji}}{s'_{ii}} \\ &= -\frac{s'_{ij}}{s'_{ii}} \end{aligned} \tag{B.10}$$

where, s'_{ji} are the compliance coefficients.

Now, the gauge factor can be described by [44, 45]

$$\mathrm{GF} = 1 - \sum_{j=1} \frac{S'_{ij}}{S'_{ii}}(1 - \delta_{ij}) + \frac{\pi_d}{S'_{ii}} \tag{B.11}$$

In the longitudinal direction (d=l), when the current and field are both in the same direction of the stress, (e.g. $\acute{i} = \acute{1}$), the gauge factor can be shown as

$$\begin{aligned} \mathrm{GF} &= 1 - 2\frac{S'_{12}}{S'_{11}} + \frac{\pi_l}{S'_{11}} \\ &= 1 + 2\nu'_{12} + \frac{\pi_l}{S'_{11}} \end{aligned} \tag{B.12}$$

Again, in equation (B.12) the contribution of the dimensional term $1 + 2\nu'_{12}$ is approximately between 1.02 and 1.22 for monocrystalline diamond [48]. Therefore equation (B.12) can be rewritten as

$$\mathrm{GF} = \frac{\pi_l}{S'_{11}} \tag{B.13}$$

APPENDIX C

Strain Analysis

The objective of this analysis is to derive an expression for the calculation of the strain on the top surface of our specimen which is needed in the gauge factor calculations.

Figure C.1(a) shows a simple cantilever beam in bending. The beam has a fixed length l, and is deflected by a force F using a micrometer head. After loading, the axis is bent into a curve that is known as the deflection curve of the beam. Figure C.1(b) shows a cross section of the bending beam. This figure is greatly exaggerated to illustrate the analysis. It is clear that the top surface of the beam is extended (under tension) and the bottom surface is contracted (under compression). It is clear that the middle plane indicated by the dotted line in the figure is unaltered in length. This plane is known as the neutral surface.

The radius of curvature, ρ, is defined as the distance from the neutral surface to the center of curvature Figs. 5.2(b) and (c). It is known from the calculus that the curvature of a plane curve is given by

$$\frac{1}{\rho} = \frac{d^2y}{dx^2} \tag{C.1}$$

where y(x) is a function of x.

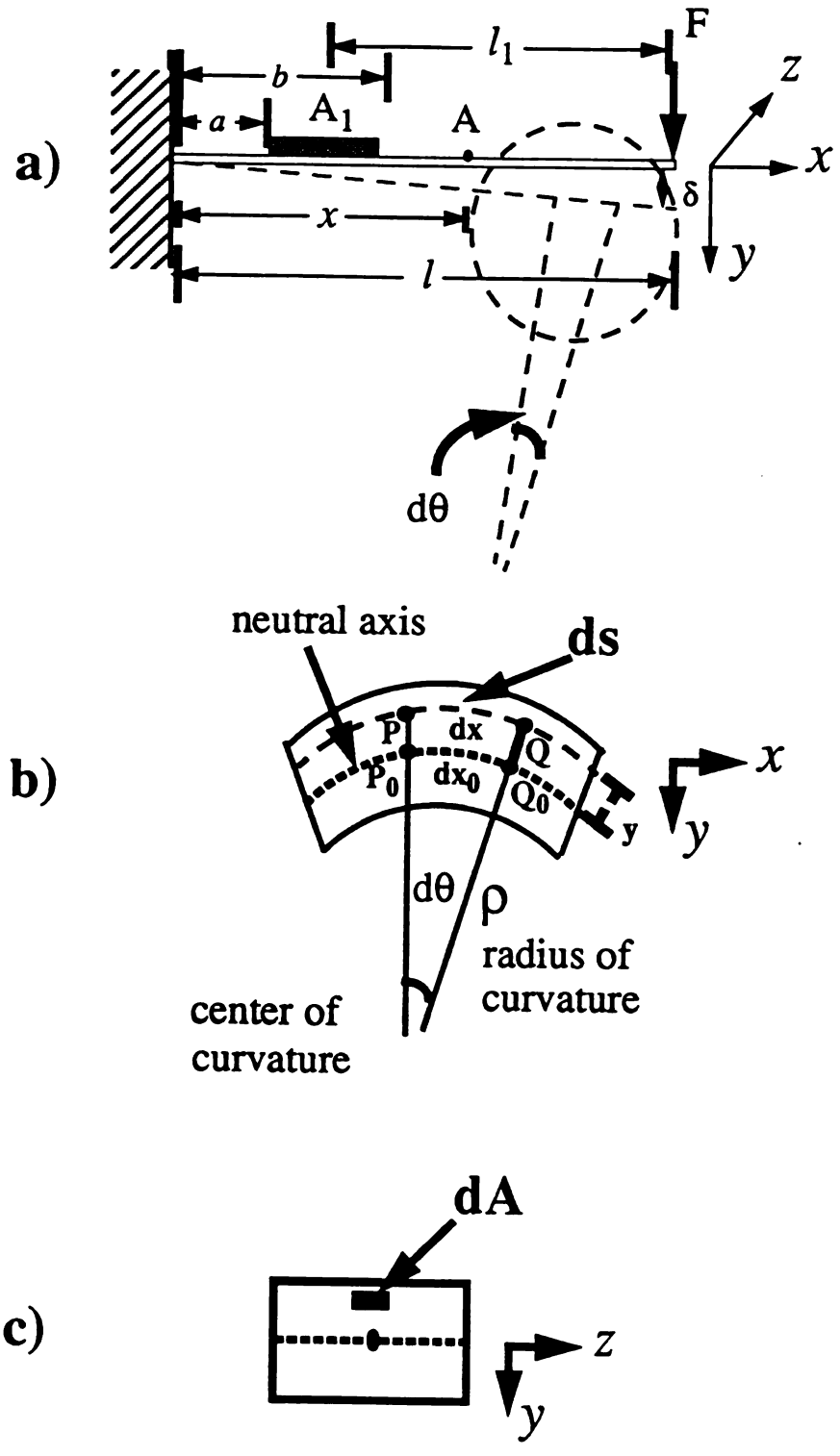

Figure C.1. Schematic diagram for strain calculation (a) Cross section view of the bending beam (b) Side view for element inside the dashed circle (c) cross-section view front section (y,z) plane.

Now, assuming small deflection, then from the geometry of the figure, we obtain

$$dx_0 = \rho d\theta \tag{C.2}$$

and

$$dx = (\rho + y)d\theta \tag{C.3}$$

where dθ is the deflection angle, dx the length of a small element (PQ) located on a surface (ds) above the neutral surface and y is the distance between this element and the neutral surface. dx_0 is the initial length of the small element.

Using geometry, and by similar triangles, the longitudinal strain on the surface ds is given by

$$\begin{aligned} \epsilon_x &= \frac{dx - dx_0}{dx_0} \\ &= \frac{y}{\rho} \end{aligned} \tag{C.4}$$

where (dx - dx_0) is the elongation.

Now, this strain can be thought to be produced by a longitudinal stress X_x, which from Hook's law can be written as

$$X_x = Y\,\epsilon_x \tag{C.5}$$

where Y is the Young's modulus.

The distribution of stress in any section perpendicular to the x direction can be given by substituting Eq. (C.4) into Eq. (C.5)

$$X_x = Y\,\frac{y}{\rho} \tag{C.6}$$

Consider an element of area dA in the cross-section (y,z) at a distance y from the

neutral axis as shown in Fig. 5.2(d). The force acting on this element is normal to the cross-section and has a magnitude X_x dA.

The moment about the z-axis is given by

$$\begin{aligned} M_z &= \int y\, X_x\, dA \\ &= \int Y \frac{y}{\rho}\, y dA \\ &= \frac{Y}{\rho} \int y^2\, dA \\ &= \frac{Y}{\rho} I_z \end{aligned} \tag{C.7}$$

where I_z is the moment of inertia of the cross-sectional area with respect to z axis, which in this case is equal to

$$I_z = \frac{bh^3}{12}. \tag{C.8}$$

where b is the width of the beam and h is its thickness. Equation (C.7) can be written as

$$\frac{1}{\rho} = \frac{M_z}{Y I_z} \tag{C.9}$$

Now, substituting Eq. (C.9) into Eq. (C.4), the strain can be written as

$$\epsilon_x = \frac{M}{YI} y \tag{C.10}$$

and the stress is written by

$$X_x = \frac{My}{I} \tag{C.11}$$

The bending moment M at a point A, a distance x from the fixed end of the beam (Fig. 5.2(b)) is given by

$$M = F\,(l - x) \tag{C.12}$$

now from (C.9) and (C.1) and (C.12) we can get

$$\begin{aligned} \frac{d^2y}{dx^2} &= \frac{M}{YI_z} \\ &= \frac{F(l-x)}{YI_z} \end{aligned} \tag{C.13}$$

Integration Eq. (C.13) gives,

$$\frac{dy}{dx} = \frac{F}{YI_z}[lx - \frac{1}{2}\, x^2 + C_1] \tag{C.14}$$

where C_1 is a constant. Considering boundary condition at the fixed end of the beam ($x = 0$), $\frac{dy}{dx} = 0$ giving $C_1 = 0$. Replacing C_1 by zero and integrating a second time produces

$$y = \frac{F}{YI_z}[\frac{1}{2}\, x^2 - \frac{1}{6}\, x^3 + C_2] \tag{C.15}$$

where C_2 is a constant. Again, considering boundary condition $y = 0$ at $x = 0$ gives $C_2 = 0$. Now, replacing C_2 by zero, results in the final equation for the deflecting beam as

$$y = \frac{F}{YI_z}[\frac{1}{2}\, x^2 - \frac{1}{6}\, x^3]. \tag{C.16}$$

The maximum deflection of the beam occurs at its free end ($x = l$) and is given by,

$$y = \frac{F}{Y}\,\frac{l^3}{3I_z} \tag{C.17}$$

Eq. (C.17) can be rewritten as,

$$\frac{F}{Y} = \frac{3I_z}{l^3}\, y \tag{C.18}$$

The bending moment M_1 at point A_1 (center of the sample), a distance x_1 from the free end is given by

$$M_1 = Fx_1 \tag{C.19}$$

Now from Eq.(C.10) and (C.19) the strain at point A_1 is given by

$$\epsilon_x = \frac{F\, x_1}{YI}\frac{h}{2} \tag{C.20}$$

Looking at Eq. (C.20), it can be seen that two variables, namely the force F and the Young's modulus Y are needed to calculate the strain. However, these two variables can be eliminated by substituting Eq. (C.18) into Eq. (C.20) and the expression for strain is given by

$$\epsilon_x = \frac{3}{2}\frac{h}{l^3} x_1\, y \tag{C.21}$$

In our experiment Fig. 5.2(a) and (b), where $x_1 = (l - \frac{1}{2}(a+b))$, the final expression for strain is

$$\epsilon_x = \frac{3}{2}\,\frac{h}{l^3}\,[l - \frac{1}{2}(a+b)]\, y \tag{C.22}$$

APPENDIX D

Sample Descriptions

Table D.1. Sample description after the deposition of the diamond films.

I.D.	Gas Flow (SCCM)			Sub. Temp.	Dep. Time
	H_2	CH_4	CO	(°C)	(hrs.)
H3ST25/DP19	100.0	0.75	12.0	825	8.5
H3ST43/PE22	100.0	0.75	12.0	890	14
H3ST69/T-2	100.0	0.75	12.0	925	8
H3ST71/T-3	100.0	0.75	12.0	925	8
H3ST74/T-2	100.0	0.75	12.0	825	9
H3ST75	100.0	0.75	12.0	825	4
H3ST77/H3ST67	100.0	0.75	12.0	825	8
H3ST20/NLO8	100.0	0.75	12.0	890	14
H3ST73/T-1	100.0	0.75	12.0	890	11
H3GF91/TS-1	100.0	0.75	12.0	825	10
H2GF80	100.0	1	12.0	825	10
H3GF92	100.0	0.75	12.0	825	12.5
H3GF93/PE20-S	50.0	0.75	12.0	890	9.5
H3GF94/PE20-S	70.0	0.75	12.0	890	8
H3GF95/PE20	40.0	0.75	12.0	890	12
H3GF96/PE20	55.0	0.75	12.0	890	12
H3GF97/PE20	50.0	0.75	12.0	890	11
H3GF98/DP16	70.0	0.75	12.0	890	13.5
H3GF99/DP16	60.0	0.75	12.0	890	12.5
H4GF00/IT1	50.0	0.75	0.0	890	16

Table D.2. Sample description after the deposition of the diamond films.

I.D.	Gas Flow (SCCM)			Sub. Temp.	Dep. Time
	H_2	CH_4	CO	(°C)	(hrs.)
H4GF01/IT1	60.0	0.75	0.0	890	13
H4GF02/IT4	70.0	0.75	0.0	890	12.5
H4GF03/T51	70.0	0.75	0.0	890	20.5
H4GF05/IT-1	100.0	0.5	0.0	890	
H280/H279	100.0	0.5	12.0	890	4.5
H281/H280	100.0	0.753	12.0	890	8
H282/2P2O-4	100.0	0.753	12.0	890	8
H283/MA16-1	100.0	0.753	12.0	890	9
H284/PE16-2	100.0	0.753	12.0	890	5
H285/ 1P3LTO-5	100.0	0.753	12.0	890	7
H286/PE14-16 PE14-16	100.0	0.753	12.0	890	6
H287/DP13	100.0	0.753	12.0	890	7
H288/I42	100.0	0.753	12.0	890	4+5
H294/H288	100.0	0.753	12.0	890	+10
H289/NLO-6	100.0	0.753	12.0	890	4.5+4.5
H302D/H289	100.0	0.753	12.0	890	+3.5
H290/LTO-12	100.0	0.753	12.0	890	8+7
H296/H290	100.0	0.753	12.0	890	+5
H291/NLO-1	100.0	0.753	12.0	890	6
H292/DP14-1	100.0	0.753	12.0	890	3.5
H297/H292	100.0	0.753	12.0	890	+5.5
H293/ 2P3LTO-8	100.0	0.753	12.0	890	7.5
H293/ 2P3LTO-8	100.0	0.753	12.0	890	7.5
H295/HS-11	100.0	0.753	12.0	890	7.5
H298/SC46-1	100.0	0.753	12.0	890	7
H299/SC47-2	100.0	0.753	12.0 ?	890	3.5
H300/SC47-3	100.0	0.753	12.0	890	8

Table D.3. Sample description after the deposition of the diamond films.

I.D.	Gas Flow (SCCM)			Sub. Temp.	Dep. Time
	H_2	CH_4	CO	(°C)	(hrs.)
H301/NLO-7	100.0	0.753	12.0	890	8
	100.0	0.753	12.0	890	+6
H303D/H282	100.0	0.753	12.0	890	4
H304D/H300	100.0	0.753	0.0	890	3
H306D/H295	100.0	0.753	12.0	890	4
H307/H299	100.0	0.753	12.0	890	5.5
H308/SC46	100.0	0.753	12.0	890	8
H310/H308	100.0	0.753	12.0	890	8
H314D/H310	100.0	0.753	12.0	890	3.5
H309/NLO1	100.0	0.753	12.0	890	12
H311/H309	100.0	0.753	12.0	890	4
H312/HS13	100.0	0.753	12.0	890	8
H317/H312	100.0	0.753	12.0	890	6
H313a/NLO5	100.0	0.753	12.0	890	8
H315/NLO5	100.0	0.753	12.0	890	7
H318/H315	100.0	0.753	12.0	890	10
H316D/H304D	100.0	0.753	12.0	890	3
H319/HS13	100.0	0.753	12.0	890	12
H320/NLO8	100.0	0.753	12.0	890	14
H321/HS14	100.0	0.753	12.0	890	9
H322/HS15	100.0	0.753	12.0	890	7.5
H323/HS14	100.0	0.753	12.0	890	4.5
H324/LTO3	100.0	0.753	12.0	890	7
H325/DP19	100.0	0.753	12.0	890	8
H328/I57	100.0	0.753	12.0	890	7
H389/H328	100.0	0.700	12.0	850	1
H329/2P2O5	100.0	0.753	12.0	890	7+3
H330/I60	100.0	0.753	12.0	890	15
H331/1P-1	100.0	0.753	12.0	890	12
H333/PNH1	100.0	0.753	12.0	890	10
H334/I57	100.0	0.753	12.0	890	12

Table D.4. Sample description after the deposition of the diamond films.

I.D.	Gas Flow (SCCM)			Sub. Temp.	Dep. Time
	H_2	CH_4	CO	(°C)	(hrs.)
H335/2P2O5	100.0	0.753	12.0	890	10
H336/I60	100.0	0.753	12.0	890	12
H336D	100.0	.7	0.0	800	+2.3
H337/1P-1	100.0	0.753	12.0	890	.5
H338/NY-1	100.0	0.753	12.0	890	.5
H341/H338	100.0	0.753	12.0	890	2.5
H339/LTO-2	100.0	0.753	12.0	890	8
H342/PE21	100.0	0.753	12.0	890	12.5
H343/PE22	100.0	0.753	12.0	890	14
H344/PE21	100.0	0.753	12.0	890	20.5
H345/HS19	100.0	0.753	12.0	890	16
H346/HS18	100.0	0.753	12.0	890	17
H347/HS19	100.0	0.753	12.0	890	13
H348/MA-1	100.0	0.753	12.0	890	12
H349/NLO-9	100.0	0.753	12.0	890	8
H350/PNH1	100.0	0.753	12.0	890	10.5
H350D	100.0	0.700	0.0	800	1.3
H351D/H322	100.0	0.753	12.0	890	3
H352D/H329	100.0	0.753	12.0	890	4.5
H354D/H342	100.0	0.753	12.0	890	3
H355D/H343	100.0	0.753	12.0	890	3.5
H356D/H346	100.0	0.753	12.0	890	4
H357D/H347	100.0	0.753	12.0	890	3.5
H359/MA1	100.0	0.5	12.0	890	10.5
H361/PNH3	100.0	0.5	12.0	890	9.5
H362/PNH3	100.0	0.7	12.0	890	10.5
H364/PNH2	100.0	0.7	12.0	890	10
H366/PNH3	100.0	0.7	12.0	890	1
H367/T-1	100.0	0.7	12.0	890	8
H368/T-1	100.0	0.7	12.0	890	8.5
H373/H368	100.0	0.7	12.0	890	3

BIBLIOGRAPHY

BIBLIOGRAPHY

[1] B. V. Spitsyn, L. L. Bouilov, and B. V. Deryagin, "Vapor growth of diamond on diamond and other surfaces ," *J. Crystal Growth*, vol. 52, pp. 219–226, 1981.

[2] S. Middelhoek and A. C. Hoogerwerf, "Smart Sensors: When and Where?," *Sensors and Actuators*, vol. 8, pp. 39–48, 1985.

[3] K. E. Petersen, "Silicon as a mechanical material," *Proc. IEEE*, vol. 70, no. 5, pp. 420–457, 1982.

[4] G. Blasquez, P. Pons, and A. Boukabache, "Capabilities and Limits of Silicon Pressure Sensors," *Sensors and Actuators*, vol. 17, pp. 387–403, 1989.

[5] M. Akbar and M. A. Shanblatt, "Temperature compensation of piezoresistive pressure sensors," *Sensors and Actuators*, vol. A 33, pp. 155–162, 1992.

[6] S. Middelhoek and S. A. Audit, *Silicon Sensors*. London: Academic Press, 1989.

[7] P. W. Bridgman, "The effect of tension on the electrical resistance of certain abnormal metals," *Proc. Amer. Acad.*, vol. 57, pp. 41–66, 1922.

[8] P. W. Bridgman, "The effect of tension on the transverse and longitudinal resistance of metals," *Proc. Amer. Acad.*, vol. 60, pp. 423–449, 1925.

[9] H. Rolnick, "Tension coefficient of resistance of metals," *Phys. Rev.*, vol. 36, pp. 506–512, Aug. 1930.

[10] M. Allen, "The effect of tension on the electrical resistance of single bismuth crystals," *Phys. Rev.*, vol. 42, pp. 848–857, Dec. 1932.

[11] M. Allen, "The effect of tension on the electrical resistance of single antimony crystals," *Phys. Rev.*, vol. 43, pp. 569–576, Apr. 1933.

[12] M. Allen, "The tension coefficients of resistance of the hexagonal crystals zinc and cadmium," *Phys. Rev.*, vol. 49, pp. 248–253, Feb. 1936.

[13] M. Allen, "The effect of tension on the electrical resistance of single tetragonal tin crystals," *Phys. Rev.*, vol. 52, pp. 1246–1249, Dec. 1937.

[14] J. W. Cookson, "Theory of the piezo-resistive effect," *Phys. Rev.*, vol. 47, pp. 194–195, 1935.

[15] H. F. Rondeau, "An introduction on the resistance wire strain gage," *ISA Proc.*, vol. 8, no. (53-7-0), pp. 86–91, 1953.

[16] G. C. Kuczynski, "Effect of elastic strain on the electrical resistance of metals," *Phys. Rev.*, vol. 94, pp. 61–64, Apr. 1954.

[17] C. S. Smith, "Piezoresistance effect in germanium and silicon," *Phys. Rev.*, vol. 94, no. 1, pp. 42–49, 1954.

[18] Y. Onuma and K. Sekiya, "Piezoresistive properties of polycrystalline silicon thin film," *Japan. J. appl. Phys.*, vol. 11, no. 1, pp. 20–23, 1972.

[19] J. Y. W. Seto, "piezoresistive properties of polycrystalline silicon," *J. Appl. Phys.*, vol. 47, pp. 4780–4783, Nov. 1976.

[20] R. W. Keyes and M. Pollak, "Effects of hydrostatic pressure on the piezoresistance of semiconductors: i-InSb, p-Ge, p-InSb, and n-GaSb," *Phys. Rev.*, vol. 118, pp. 1001–1007, May 1960.

[21] M. G. Holland and W. Paul, "Effect of pressure on the energy levels of impurities in semiconductors. I. Arseni, Indium, and Aluminum in silicon," *Phys. Rev.*, vol. 128, pp. 30–38, Oct. 1962.

[22] L. F. Bellard and J. J. Wortman, "Piezoresistance in organometallic crystals," *J. Appl. Phys.*, vol. 41, pp. 4232–4236, Sep. 1970.

[23] K. Ohe and Y. Naito, "Piezoresistance effect of graphite-papostor," *Japan. J. appl. Phys.*, vol. 10, no. 7, pp. 868–872, 1971.

[24] W. P. Mason and R. N. Thurston, "Use of piezoresistive materials in the measurement of displacement, force, and torque," *J. Acoust. Soc. Amer.*, vol. 29, pp. 1096–1101, Oct. 1957.

[25] W. G. Pfann and R. N. Thurston, "Semiconducting stress transducers utilizing the transverse and shear piezoresistance effects," *J. Appl. Phys.*, vol. 32, no. 10, pp. 2008–2019, 1961.

[26] J. C. Sanchez and W. V. Wright, "Semiconductor strain gages: What can they do?," *ISA Journal*, vol. 9, no. 5, pp. 38–40, 1962.

[27] O. N. Tufte, P. W. Chapman, and D. Long, "Silicon diffused-element piezoresistive diaphragms," *J. Appl. Phys.*, vol. 33, pp. 3322–3327, Nov. 1962.

[28] D. R. Kerr and A. G. Milnes, "Piezoresistive strain gages and transducer elements," *IEEE Trans. Instrum. Meas.*, vol. IM-12, p. 73, 1963.

[29] T. R. Kiggins and A. G. Milnes, "A solid state tunnel diode strain gage," *18th Ann. ISA Conf.*, pp. 1–9, Sep.(9-12) Chicago 1963.

[30] R. N. Thurston, "Use of semiconductor transducers in measuring strain, accelerations, and displacements," in *Physical Acoustics*, vol. 1, p. 215, New York: Academic Press 1964.

[31] I. Taher, M. Aslam, A. H. Meitzler, and G. S. Saloka, "Resistance-vs-strain nonlinearity for ion-implanted, junction isolated piezoresistors," *Proc. Sen. Expo 90*, pp. 104B1–4, 1990.

[32] J. Binder, W. Henning, E. Obermeier, H. Schaber, and D. Cutter, "Laser-recrystallized polysilicon resistors for sensing and integrated circuits applications," *Sensors and Actuators*, vol. 4, pp. 527–536, 1983.

[33] J. Detry, D. Koneval, and S. Blackstone, "A comparison of piezoresistance in polysilicon, Laser-recrystallized polysilicon and single crystal silicon," *Digest of Technical Papers, 3rd Int. Conf. on Solid-State Sensors and Actuators*, pp. 278–280, 1985.

[34] Y. Onuma, K. Kamimura, and Y. Homma, "Piezoresistive Elements of Polycrystalline Semiconductor Thin Films," *Sensors and Actuator*, vol. 13, pp. 71–77, 1988.

[35] K. Kamimura, N. Kimura, Y. Onuma, and T. Homma, "Pressure Sensor Using Polycrystalline Germanium Films Prepared by Plasma-assisted Chemical Vapour Deposition," *Sensors and Actuator*, vol. A21-A23, pp. 958–960, 1990.

[36] I. V. Rapatskaya, G. E. Rudashevskii, M. G. Kasaganova, M. I. Iglitsin, M. B. Reifman, and E. F. Fedotova, "Piezoresistance Coefficients of n-Type α-SiC," *Soviet Physics-Solid State*, vol. 9, pp. 2833–2835, June 1968.

[37] J. S. Shor, D. Goldstein, and A. D. Kurtz, "Evaluation of β-SiC for sensors," *IEEE Proceedings, Intl. Conf. on Solid-State Sensors and Actuators (Transducers'91)*., pp. 912–915, San Francisco, June 1991.

[38] Y. Onuma, F. Nagaune, and K. Kamimura, "Preparation and Properties of Polycrystalline Silicon Carbide Films Produced by Plasma Enhanced Chemical Vapor Deposition and Their Applications," *Springer Proc. in Physics, Ed. G. L. Harris and C. Y. Yang*, vol. 34, pp. 142–147, 1989.

[39] M. Prudenziati, B. Morten, and A. Taroni, "Characterization of thick-film resistor strain gauges on enamel steel," *Sensors and Actuators*, vol. 2, pp. 17–27, 1981/82.

[40] M. Prudenziati and B. Morten, "Thick- Film Sensors: An Overview," *Sensors and Actuator*, vol. 10, pp. 65–82, 1986.

[41] W. R. Langdon, W. K. Bennett, W. T. Decker, and W. E. Garland, "Radiation effects on piezoresistive accelerometers," *IEEE Trans*, vol. IECI, p. 99, 1970.

[42] W. P. Mason, "Semiconductor transducers -general considerations," in *Physical Acoustics*, vol. 1, p. 173, New York: Academic Press 1964.

[43] J. C. Erskine, "Polycrystalline silicon-on-metal strain gauge transducers," *IEEE Trans. Electron. dev.*, vol. ED-30, no. 7, pp. 796–801, 1983.

[44] P. J. French, "Piezoresistance in polysilicon," *Electron. Lett.*, vol. 24, pp. 999–1000, 1984.

[45] P. J. French and A. G. R. Evans, "Polycrystalline silicon strain sensors," *Digest of Technical Papers, 3rd Int. Conf. on Solid-State Sensors and Actuators*, pp. 281–283, 1985.

[46] H. J. McSkimin, P. Andreatch, and P. Glynn, "The elastic stiffness moduli of diamond," *J. Appl. Phys.*, vol. 43, pp. 985–987, March 1972.

[47] C. A. Klein and G. F. Cardinale, "Young's modulus and Poisson's ratio of CVD diamond," *Diamond and Related Materials*, vol. 2, pp. 918–923, 1993.

[48] M. Werner, S. Hein, and E. Obermeier, "Elastic properties of thin polycrystalline diamond films," *Diamond and Related Materials*, vol. 2, pp. 939–942, 1993.

[49] C. Herring and E. Vogt, "Transport and deformation-potential theory for many-valley semiconductors with anisotropic scattering," *Phys. Rev.*, vol. 101, pp. 944–961, Feb. 1956.

[50] J. C. Hensel and G. Feher, "Cyclotron resonance experiments in uniaxially stressed silicon: valence band inverse mass parameters and deformation potentials," *Phys. Rev.*, vol. 129, pp. 1041–1062, Feb. 1963.

[51] G. Feher, J. C. Hensel, and E. A. Gere, "Paramagnetic resonance absorption from acceptors in silicon," *Phys. Rev. Letters*, vol. 5, p. 309, Oct. 1960.

[52] J. C. Hensel and G. Feher, "Valence band parameters in silicon from cyclotron resonances in crystals subjected to uniaxial stress," *Phys. Rev. Letters*, vol. 5, p. 307, Oct. 1960.

[53] F. P. Bundy, H. T. Hall, H. M. Strong, and R. H. Wentroff, "Man-made diamond," *Nature*, vol. 176, pp. 51–54, 1955.

[54] J. F. H. Clusters, "Unusual phosphorescence of a diamond," *Physica*, vol. 18, pp. 489–496, Aug/Sep. 1952.

[55] J. E. Field, *The Properties of Diamond.* London: Academic Press, 1979.

[56] C. A. Brookes and E. J. Brookes, "Diamond in perspective: a review of mechanical properties of natural diamond," *Diamond and Related Materials*, vol. 1, pp. 13–17, 1991.

[57] J. A. Herb, M. G. Peters, S. C. Terry, and J. H. Jerman, "PECVD Diamond Films for Use in Silicon Microstructures," *Sensors and Actuator*, vol. A21-A23, pp. 982–987, 1990.

[58] R. W. Bower, "The Compatibility of PECVD Diamond in the design and Fabrication of a self-aligned Rigid Suspended Plate," *Sensors and Actuator*, vol. A21-A23, pp. 993–998, 1990.

[59] J. L. Davidson, R. Rameshan, and C. Ellis, "Synthetic diamond micromechanical membranes, cantilever beams and bridges," *J. Electrochem. Soc.*, vol. 137, pp. 3206–3210, 1990.

[60] C. E. Ellis, D. A. Jaworske, R. Ramesham, and T. Roppel, "Polycrystalline Diamond Film Flow Sensor," *J. IEEE.*, p. 132, Sep. 1990.

[61] R. Ramesham, T. Roppel, C. Ellis, and M. F. Rose, "Fabrication of Microchannels in Synthetic Polycrystalline Diamond Thin Films for Heat Sinking Applications," *J. Electrochem. Soc.*, vol. 138, p. 1706, June 1991.

[62] M. Aslam, I. Taher, A. Masood, M. A. Tamor, and T. J. Potter, "Piezoresistivity in vapor deposited diamond films," *Appl. Phys. Lett.*, vol. 60, pp. 2923–2925, 1992.

[63] S. S. Perry, J. W. Ager, and G. A. Somorjai, "Combined surface characterization and tribological (friction and wear) studies of CVD diamond films," *J. Mater. Res.*, vol. 8, pp. 2577–2586, Oct. 1992.

[64] A. Nishikawa, "Measurement of Thermal Conductivity of Diamond Films," *New Diamond*, vol. 6, pp. 70–72, 1990.

[65] M. W. Geis, H. I. Smith, A. Argoit, J. Angus, G. H. Ma, J. T. Glass, J. Butler, C. T. Robinsin, and R. Proyer, "Large area mosaic diamond films approaching single crystal quality," *MRS.*, 1991.

[66] G. A. Slack and S. F. Bartram, "Thermal expansion of some diamondlike crystals," *J. Appl. Phys.*, vol. 46, pp. 89–98, Jan. 1975.

[67] C. H. Xu, C. Z. Wang, C. T. Chan, and K. M. Ho, "Theory of the thermal expansion of Si and diamond," *Phys. Rev. B*, vol. 43, pp. 5024–5027, 1991.

[68] K. Haruna and H. Maeta, "Thermal expansion of synthetic diamond single crystals at low temperatures," *Diamond and Related Materials*, vol. 2, pp. 859–861, 1993.

[69] M. W. Geis, D. D. Rathman, D. J. Ehrlich, R. A. Murphy, and W. T. Lindley, "High Temperature Point Contact Transistors and Schottkey Diodes Formed on Synthetic Boron Doped Diamonds," *IEEE Electron Device Lett.*, vol. 8, no. 8, pp. 341–343, 1987.

[70] K. Lonsdale and H. J. Milledge, *in Physical Properties of Diamond. Ed. R. Berman.* Oxford: Clarendon Press, 1965.

[71] W. Zhu, X. H. Wang, A. R. Badzian, and R. Messier, "An investigation of the oxidation behavior of CVD diamond films," *New Diamond Sci. and Tech. @ MRS Int. Conf. Proc.*, pp. 821–826, 1991.

[72] S. Tolansky, *in Physical Properties of Diamond. Ed. R. Berman.* Oxford: Clarendon Press, 1965.

[73] J. Wei and Y. Tzeng, "Reaction of CVD diamond with molten iron film," *2nd Int. Conf. on the Appli. of Diamond Films and Related Materials. Yoshikawa et al.*, vol. 2, pp. 609–612, Tokyo, Japan 1993.

[74] V. S. Vavilov, "Diamond as a material in solid state electronics," *Mat. Res. Soc. Symp. Proc.*, vol. 242, pp. 87–95, 1992.

[75] L. S. Pan, S. Han, D. R. Kania, M. A. Plano, and M. I. Landstrass, "Electrical properties of high quality diamond films," *Diamond and Related Materials*, vol. 2, pp. 820–824, 1993.

[76] Y. Mori, H. Yagi, M. Deguchi, M. Kitabatake, K. Nishimura, A. Hatta, T. Ito, T. Hirao, T. Sasaki, and A. Hiraki, "Crystallinities and electrical properties of homoepitaxial diamond films grown from carbon monoxide," *2nd Int. Conf. on the Appli. of Diamond Films and Related Materials. Yoshikawa et al.*, vol. 2, pp. 393–398, Tokyo, Japan 1993.

[77] N. Fujimori, "Electrical applications of CVD diamond films," *New Diamond Sci. and Tech. @ MRS Int. Conf. Proc.*, pp. 901–908, 1991.

[78] M. W. Geis, "Diamond Transistor Performance and Fabrication," *Proceedinds of the IEEE*, vol. 79, pp. 669–676, May 1991.

[79] M. I. Landstrass and K. V. Ravi, "Hydrogen passivation of electrically active defects in diamond," *Appl. Phys. Lett.*, vol. 55, no. 14, pp. 1391–1393, 1989.

[80] G. Lu, "Applications of CVD Diamond in Thermal Management," *2nd Int. Conf. on the Appli. of Diamond Films and Related Materials. Eds: Yoshikawa et al.*, vol. 2, pp. 269–274, Tokyo, Japan 1993.

[81] L. M. Napolitano, D. D. Andaleon, M. R. Daily, E. Meeks, D. Miller, D. P. Norwood, D. W. Peterson, C. A. Reber, and W. Worobey, " ," *2nd Int. Conf. on the Appli. of Diamond Films and Related Materials. Eds: Yoshikawa et al.*, vol. 2, pp. 275–279, Tokyo, Japan 1993.

[82] G. Lu, K. J. Gray, E. F. Borchelt, L. K. Bigelow, and J. E. Graebner, "Free-standing white diamond for thermal and optical applications," *Diamond and Related Materials*, vol. 2, pp. 1064–1068, 1993.

[83] K. V. Ravi, "Current status of selected aerospace applications of diamond," *2nd Int. Conf. on the Appli. of Diamond Films and Related Materials. Yoshikawa et al.*, vol. 2, pp. 13–18, Tokyo, Japan 1993.

[84] G. Muller and G. Krotz, "SiC as a new sensor material," *IEEE Proceedings, Intl. Conf. on Solid-State Sensors and Actuators (Transducers'93).*, p. 948, Yokohama, Japan, June 7-10 1993.

[85] Y. Tzeng, A. Hirata, S. Takeuchi, J. Wei, and A. Joseph, "CVD diamond heat rejection with Built-in cooling channels," *2nd Int. Conf. on the Appli. of Diamond Films and Related Materials. Yoshikawa et al.*, vol. 2, pp. 669–672, Tokyo, Japan 1993.

[86] J. V. Busch, J. P. Dismukes, N. V. Nallicheri, and K. R. Walton, "Economic Assessement of HPHT Diamond Synthesis Technology," *Proc. of the 1st Int. Conf. on the Applications of Diamond Films and Related Materials.*, vol. B.V., pp. 623–633, Auburn, Alabama Aug. 17-22 1991.

[87] T. R. Anthony, *Methods of Diamond Making.* Plenum Press, New York: in Diamond and Diamond-Like Films and Coatings. Ed. by R. E. Clausing et al., 1991.

[88] J. P. Dismukes, J. V. Busch, N. V. Nallicheri, and K. R. Walton, "Economic Assessement of CVD Diamond Synthesis Technologies," *Proc. of the 1st Int. Conf. on the Applications of Diamond Films and Related Materials.*, vol. B.V., pp. 635–644, Auburn, Alabama Aug. 17-22 1991.

[89] K. Bigelow, "Progress in the commercialzation of CVD diamond," *2nd Intr. Conf. on the Appli. of Diamond Films and Related Materials*, vol. 2, pp. 5–18, 1993.

[90] W. A. Yarbrough and R. Messier, "Current Issues and Problems in the Chemical Vapor Deposition of Diamond," *Science*, vol. 247, pp. 688–695, 1990.

[91] J. C. Angus, H. A. Will, and W. S. Stanko, "Growth of Diamond Seed Crystals by Vapor Deposition," *J. Appl. Phys.*, vol. 39, p. 2915, 1968.

[92] J. C. Angus and C. C. Hayman, "Low-Pressure, Metastable Growth of Diamond and Diamond-like Phases," *Science*, vol. 241, p. 913, 1988.

[93] S. Matsumoto, Y. Sato, M. Kamo, and N. Setaka, "Growth of diamond particles from methane-hydrogen gas," *J. Materials Science*, vol. 17, pp. 3106–3122, 1982.

[94] Y. Hirose and Y. Terasawa, "Synthesis of Diamond Thin Films by Thermal CVD Using Organic Compounds," *Jpn. J. Appl. Phys.*, vol. 25, pp. L519–L521, June 1986.

[95] F. P. Doty and W. A. Jesser, "Investigation of the Role of Charged Species in Hot Filament Assisted CVD of Diamond," *J. Electron. Mat.*, vol. 20, no. 22, 1991.

[96] P. K. Bachmann, D. Leers, and H. Lydtin, "Towards a general concept of Diamond Chemical Vapor Deposition," *Diamond and Related Materials*, vol. 1, pp. 1–12, 1991.

[97] S. J. Harris and A. M. Weiner, "Effect of Oxygen on Diamond Growth," *Appl. Phys. Lett.*, vol. 55, pp. 2179–2181, Nov. 1989.

[98] J. A. Mucha, D. L. Flamm, and D. E. Ibbotson, "On the Role of Oxygen in Diamond Forming Discharges," *Appl. Phys. Lett.*, vol. 65, pp. 3448–3452, May 1989.

[99] M. Kamo, Y. Sato, S. Matsumoto, and N. Setaka, "Diamond Synthesis from Gas Phase in Microwave Plasma," *J. Crystal Growth*, vol. 62, no. 3, p. 642, 1983.

[100] A. Sawabe and T. Inuzuka, "Growth of diamond thin films by electron-assisted chemical vapor deposition," *Tin Solid Films*, vol. 137, pp. 89–99, 1986.

[101] W. Zhu, B. R. Stoner, B. E. Williams, and J. T. Glass, " Growth and Characterization of Diamond Films on Nondiamond Substrates for Electronic Applications," *Proceedinds of the IEEE*, vol. 79, pp. 621–646, May 1991.

[102] S. Matsumoto, M. Hino, and T. Kobayashi, "Synthesis of Diamond Films in rf induction Thermal Plasma.," *Appl. Phys. Lett.*, vol. 51, no. 10, p. 737, 1987.

[103] D. E. Meyer, R. O. Dillon, and J. A. Woollam, "Radio-frequency Plasma Chemical Vapor Deposition Growth of Diamond," *J. Vac. Sci. Technol.*, vol. 7, no. 3, p. 2325, 1989.

[104] K. Suzuki, A. Sawabe, H. Yasuda, and T. Inuzuka, "Growth of Diamond Thin Films by DC Plasma Chemical Vapor Deposition.," *Appl. Phys. Lett.*, vol. 50, no. 12, p. 728, 1987.

[105] K. Kurihara, K. Sasaki, M. Kawarada, and N. Koshino, "High Rate Synthesis of Diamond by DC Plasma Jet Chemical Vapor Deposition.," *Appl. Phys. Lett.*, vol. 52, no. 6, p. 437, 1988.

[106] I. Watanabe and K. Sugata, "Diamond films synthesized by microwave plasma cvd of ethyl alcohol," *Jpn. J. appl. Phys.*, vol. 27, no. 8, p. 1397, 1988.

[107] B. Huang, "Electrical properties and physical characteristics of polycrystalline diamond films deposited in a microwave plasma disk reactor," *Ph.D. Dissertation, Michigan State University*, 1992.

[108] Y. Tzang, C. Cutshaw, R. Phillip, T. Srivinyunon, A. Ibrahim, and B. H. Loo, "Growth of Diamond Films on Silicon from an Oxygen- Acetylene Flame," *Appl. Phys. Lett.*, vol. 53, pp. 1818–1819, Nov. 1988.

[109] M. Kawarada, K. Mar, and A. Kiraki, "Large area chemical vapor deposition particles and films using magnetomicrowave plasma.," *Jpn. J. Appl. Phys.*, vol. 26, pp. L1032–34, June 1988.

[110] Y. Mitsuda, T. Yoshida, and K. Akashi, "Development of a New Microwave Plasma Torch and its Application to Diamond Synthesis.," *Rev. Sci. Instrum.*, vol. 60, no. 2, p. 249, 1989.

[111] Y. Liou, A. Inspektor, R. Weimer, and R. Messier, "Low Temperature Diamond Deposition by Microwave Plasma-enhanced CVD.," *Appl. Phys. Lett.*, vol. 55, no. 7, p. 631, 1989.

[112] W. L. Hsu, D. M. Tung, E. A. Fuchs, and K. F. McCarty, "Low Temperature Diamond Growth in a Microwave Discharge.," *Appl. Phys. Lett.*, vol. 55, no. 26, p. 2739, 1989.

[113] J. Wei, H. Kawarada, J. I. Suzuki, and A. Hiraki, "Low Temperature Synthesis of Diamond Films Using Magneto- Microwave Plasma CVD.," *Jpn. J. Appl. Phys.*, vol. 29, no. 8, p. L1483, 1990.

[114] J. Asmusson and J. Root, "Characteristics of a Microwave Plasma Disk Ion Source," *Appl. Phys. Lett.*, vol. 44, p. 396, 1984.

[115] J. Zhang, "Diamond film deposition by microwave plasma assisted chemical vapor deposition," *Ph.D. Dissertation, Michigan State University*, 1990.

[116] C. P. Chang, D. L. Flamm, D. E. Ibbotson, and J. A. Mucha, " Diamond Crystal Growth by Plasma Chemical Vapor Deposition," *J. Appl. Phys.*, vol. 63, no. 5, p. 1744, 1988.

[117] H. Shiomi, K. Tanabe, Y. Nishibayashi, and N. Fujimori, "Epitaxial Growth of High Quality Diamond Film by Microwave Plasma assisted Chemical Vapor Deposition," *Jpn. J. Appl. Phys.*, vol. 29, no. 1, p. 34, 1990.

[118] J. I. Suzuki, H. Kawarada, K. S. Mar, J. Wei, Y. Yokota, and A. Hiraki, "The Synthesis of Diamond Films at Lower Pressure and Lower Temperature Using Magneto- Microwave Plasma CVD.," *Jpn. J. Appl. Phys.*, vol. 28, no. 2, p. L281, 1989.

[119] A. Masood, M. Aslam, M. A. Tamor, and T. J. Potter, "Techniques for patterning "CVD" diamond films on non-diamond substrates," *J. Electrochem. Soc.*, vol. 138, pp. L67–L68, 1991.

[120] M. Aslam, A. Masood, R. J. Fredricks, and M. A. Tamor, "Thin film diamond temperature sensor array for harsh aerospace environment," *SPIE Proc. on Sensors and Sensor systems for guidance and Navigation II, S.S. Welch, Ed.*, vol. 92, pp. 184–186, 1992.

[121] S. Iijima, Y. Aikawa, and K. Baba, "Growth of diamond particles in chemical vapor deposition," *J. Mater. Res.*, vol. 6, no. 7, p. 1491, 1991.

[122] R. Ramesham, T. Roppel, C. Ellis, D. A. Jaworske, and W. Baugh, "Selective and low temperature synthesis of polycrystalline diamond," *J. Mater. Res.*, vol. 6, p. 1278, June 1991.

[123] Y. Liou, A. Inspektor, R. Weimer, D. Knight, and R. Messier, "The effect of oxygen in diamond deposition by microwave plasma enhanced chemical vapor deposition," *J. Mater. Res.*, vol. 5, pp. 2305–2312, Nov. 1990.

[124] N. Kikuchi, Y. Ohsawa, Y. Tamou, H. Eto, and H. Yamashita, "High resolution TEM observations of CVD diamond films," *New Diamond Sci. and Tech. @ MRS Int. Conf. Proc.*, pp. 567–574, 1991.

[125] A. Masood, "Technology and electronic properties of diamond film microsensors for thermal signals," *Ph.D. Dissertation, Michigan State University*, 1992.

[126] K. Kobashi, K. Nishimura, Y. Kawate, and T. Horiuchi, "Synthesis of diamonds by use of microwave plasma chemical vapor deposition: Morphology and growth of diamond films," *Phys. Rev. B*, vol. 38, p. 4067, Aug. 1988.

[127] S. A. Solin and A. K. Ramdas, "Raman Spectrum of Diamond," *Phys. Rev.*, vol. B 1, pp. 1687–1698, 1970.

[128] M. Yoshikawa, G.Katagiri, H. Ishida, and A. Ishitani, "Resonant Raman Scattering of Diamond-like Amorphous Carbon Films," *Appl. Phys. Lett.*, vol. 52, May 1988.

[129] M. Yoshikawa, G.Katagiri, H. Ishida, A. Ishitani, and T. Akamatsu, " Raman Spectra of Diamond-like Amorphous Carbon Films," *J. Appl. Phys.*, vol. 64, p. 6464, Dec. 1988.

[130] W. A. Yarbough and R. Messier, "Current Issues and Problems in the ChemicalVapor Deposition of Diamond," *Science*, vol. 247, pp. 688–695, 1990.

[131] D. S. Knight and W. B. White, "Characterization of Diamond Films by Raman Spectroscopy," *J. Mater. Res.*, vol. 4, pp. 385–393, 1989.

[132] L. H. Robins, E. N. Farabangh, and A. Feldman, "Line Shape Analysis of Raman Spectrum of Diamond Films Grown by Hot-Filament and Microwave Chemical Vapor Depositio," *J. Mater. Res.*, vol. 5, no. 11, pp. 2456–2468, 1990.

[133] J. F. H. Custers, "Unusual phosphorescence of a diamond," *Physica*, vol. 18, pp. 489–496, Aug. 1952.

[134] V. S. Vavilov, E. A. Konorova, V. F. Sergienko, and M. I. Guseva, "Electrical conductivity of diamond containing implanted lithium ions," *Sov. Phys. Semicond.*, vol. 6, no. 1, pp. 741–746, 1972.

[135] V. S. Vavilov, M. A. Gukasyan, M. I. Guseva, E. A. Konorova, and V. F. Serienko, "Electron-hole junctions in diamond obtained by implantation of boron and phosphorus ions," *Sov. Phys. Semicond.*, vol. 16, pp. 856–859, 1972.

[136] V. S. Vavilov, M. A. Gukasyan, M. I. Guseva, and E. A. Konorova, "Conductivity of Diamond Doped by Implantation of Phosphorous Ions," *Sov. Phys. Semicond.*, vol. 9, no. 8, pp. 962–964, 1976.

[137] J. F. Prins, "Bipolar Transistor Action in Ion-Implantation Diamond," *Appl. Phys. Lett.*, vol. 41, no. 10, pp. 950–952, 1982.

[138] C. M. Huggins and P. Cannon, "Diamond containing controlable impurity concentrations," *Nature*, vol. 194, pp. 829–830, June 1962.

[139] R. H. Wentorf, "Preparation of semiconducting diamonds," *J. Chem. Phys.*, vol. 36, pp. 1987–1990, April 1962.

[140] V. K. Bazhenov, I. M. Vikulin, and A. G. Gontar, "Synthetic diamonds in electronics (review)," *Sov. Phys. Semicond.*, vol. 19, pp. 829–841, Aug. 1985.

[141] K. Okano, Y. Akiba, T. Kurosu, M. Iida, and T. Nakamura, "Synthesis of B Doped Diamond Films," *J. Crystal Growth*, vol. 99, pp. 1192–1195, 1990.

[142] K. Okano, H. Kiyota, T. Iwasaki, Y.Naksmura, Y. Akiba, T. Kurosu, M. Iida, and T. Nakamura, "Synthesis of N-Type Semiconducting Diamond Films Using Diphosphorous Pentaoxide as the Doping Source," *J. Appl. Phys.*, vol. 51, pp. 344–346, 1990.

[143] G. H. Glover, "The C-V Characteristics of Schottky Barriers on Laboratory Grown Semiconductor Diamonds," *Solid State Electron.*, vol. 16, pp. 973–983, Sep. 1973.

[144] R. Ramesham, T. Roppel, C. Ellis, and B. F. Hajek, "Characterization of Synthetic Diamond Thin Films," *J. Electrochem. Soc.*, vol. 137, no. 10, pp. 3203–3205, 1990.

[145] G. S. Gildenblat, S. A. Grot, and A. Badzian, "The Electrical Properties and Device Applications of Homoepitaxial and Polycrystalline Diamond Films," *Proceedinds of the IEEE*, vol. 79, p. 647, May 1991.

[146] G. S. Gildenblat, "High temperature schottky diodes with thin film diamond base," *IEEE Electron. Dev. Lett.*, vol. EDL-11, pp. 371–372, Sep. 1990.

[147] J. L. Davidson, C. Ellis, and R. Ramesham, "Selective Deposition of Diamond Films," *J. Electron. Mater.*, vol. 18, no. 6, pp. 711–715, 1989.

[148] K. Hirabayashi, "Selective Deposition of Diamond Crystals," *New Diamond*, vol. 6, p. 29, 1990.

[149] J. S. MA, H. Kawarada, T. Yonehara, J. Suzuki, Y. Yokota, and A. Hiraki, "Nucleation control and selective growth of diamond particles formed with plasma CVD," *J. Crystal Growth*, vol. 99, pp. 1206–1210, 1990.

[150] J. L. Valdes, J. W. Mitchel, J. A. Mucha, L. Seibles, and H. Huggins, "Selected area nucleation and patterning of diamond thin films by electrophoretic seeding," *J. Electrochem. Soc.*, vol. 138, pp. 635–636, Feb. 1991.

[151] T. J. Whetten, A. A. Armstead, T. A. Grzybowski, and A. L. Ruoff, "Etching of diamond with argon and oxygen ion beams," *J. Vac. Sci. Technol.*, vol. 2, no. 2, pp. 477–480, 1984.

[152] N. N. Efremow, M. W. Gies, D. C. Flanders, and N. P. Econmou, "Ion-beam-assisted etching of diamond," *J. Vac. Sci. Technol.*, vol. 3, no. 1, p. 416, 1985.

[153] C. P. B. Jr, B. A. Lincoln, B. Y. Lin, and S. H. Tan, "ECR Plasma Etching of Natural Type IIa and Synthetic Diamonds," *New Diamond Sci. and Tech. @ MRS Int. Conf. Proc.*, pp. 833–838, 1991.

[154] K. Tankala and T. Debroy, "Etching of HFCVD Diamond Films in Air, Nitrous Oxide and Argon," *New Diamond Sci. and Tech. @ MRS Int. Conf. Proc.*, pp. 827–831, 1991.

[155] S. Shikata, Y. Nishbayashi, T. Tomikawa, N. Toda, and N. Fujimori, "Microfabrication technique for diamond devices," *2nd Int. Conf. on the Appli. of Diamond Films and Related Materials. Yoshikawa et al.*, vol. 2, pp. 377–380, Tokyo, Japan 1993.

[156] S. A. Grot, R. A. Ditizio, G. S. Gildenblat, A. R. Badzian, and S. J. Fonash, "Electronic device fabrication using electron cyclotron resonance etching of boron doped homoepitaxial diamond films," *Symp. Proc. MRS*, vol. 242, p. 145, 1992.

[157] K. Hirabayashi and Y. Taniguchi, "Selective Deposition of Diamond Crystals by Chemical Vapor Deposition using a Tungsten-filament Method," *Appl. Phys. Lett.*, vol. 53, no. 19, 1988.

[158] J. S. Ma, H. Kawarada, T. Yonehara, J. Suzuki, J. Wei, Y. Yokota, and A. Hiraki, "Selective Nucleation and Growth of Diamond Particles by Plasma-assisted Chemical Vapor Deposition," *Appl. Phys. Lett.*, vol. 55, p. 1071, 1989.

[159] S. Koizumi, T. Murakami, T. Inuzuka, and K. Suzuki, "Epitaxial Growth of Diamond Thin Films on Cubic Boron Nitride {111} Surfaces by DC Plasma Chemical Vapor Deposition," *Appl. Phys. Lett.*, vol. 57, pp. 563–565, Aug. 1990.

[160] R. Kohl, C. Wild, N. Herres, P. Koidl, B. R. Stoner, and J. T. Glass *Appl. Phys. Lett.*, vol. 63, p. 1792, 1993.

[161] B. R. Stoner, C. T. Kao, D. M. Malta, and R. C. Glass, "Texture made of CVD Diamond Films," *Appl. Phys. Lett.*, vol. 62, no. 11, 1993.

[162] A. V. der Drift *Philips Res. Rep.*, vol. 22, p. 267, 1967.

[163] H. Shiomi, Y. Nishibayashi, and N. Fujimori, "Field-Effect Transistors using Boron-Doped Diamond Epitaxial Films," *Jpn. J. Appl. Phys.*, vol. 28, pp. L2153–L2154, Dec. 1989.

[164] C. R. Zeisse, C. A. Hewitt, R. Nguyen, J. R. Zeidler, and C. G. Wilson, "An ion-implanted diamond metal-insulator-semiconductor field-effect transistor," *IEEE Electron Device Lett.*, vol. 12, p. 602, 1991.

[165] A. J. Tessmer, L. S. Plano, and D. L. Dreifus, "High temperature operation of polycrystalline diamond field effect transistors," *IEEE Dev. Lett.*, vol. EDL-14, pp. 66–68, Feb. 1993.

[166] S. A. Grot, G. S. Gildenblat, and A. R. Badzian, "Diamond thin film recessed gate field effect transistors fabricated by electron cyclotron resonance plasma etching," *IEEE Dev. Lett.*, vol. EDL-13, pp. 462–464, sep. 1992.

[167] D. Wooldridge, A. Ahearn, and J. Burton, "Conductivity Pulses Induced in Diamond by Alpha-Particles," *Phys. Rev.*, vol. 71, p. 913, 1948.

[168] D. R. Kania, M. I. Landstrass, M. A. Plano, L. S. Pan, and S. Han, "Diamond radiation detectors," *Diamond and Related Materials*, vol. 2, pp. 1012–1019, 1993.

[169] L. F. Vereshchagin, K. K. Demidov, O. G. Revin, and V. N. Slesarev, "Thermistor made of p-type synthetic diamond," *Sov. Phys. Semicond.*, vol. 8, pp. 1581–1582, June 1975.

[170] N. Fujimori and H. Nakahata, "Thermistor made of CVD Diamond Films," *New Diamonds*, pp. 98 –101, 1990.

[171] M. Werner, V. Schlichting, and E. Obermeier, "Thermistor made of CVD Diamond Films," *Diamond and Related Mat.*, vol. 1, 1992.

[172] G. B. Rogers and F. A. Raal, "Semiconducting Diamonds as Thermistors," *Rev. Sci. Inst*, vol. 31, pp. 663–664, 1960.

[173] U. S. Patent, " 3,435,399," *25 March*, 1969.

[174] J. P. Bade, S. R. Sahaida, B. R. Stoner, J. A. von Windheim, J. T. Glass, K. Miyata, K. Nishimura, and K. Kobashi, "Fabrication of diamond thin-film thermistors for high-temperature applications," *Diamond and Related Materials*, vol. 2, pp. 816–819, 1993.

[175] V. I. Latsa and Y. M. Rotner, "Effect of axial pressure on some properties of synthetic semiconductor diamonds (original in Russian)," *Vys. Davleniya Svoita Mater.*, pp. 55–59, 1980.

[176] V. I. Latsa, I. N. Mikhailik, and G. V. Krishchuk, "Current-Voltage characteristics of synthetic diamond under pressure (original in Russian)," *Fiz. Tekh. Vys. Davlenii.*, vol. 9, pp. 62–65, 1982.

[177] B. E. Williams and J. T. Glass, "Characterization of diamond thin films : diamond phase identifications, surface morphology, and defect structures," *J. Materials Res.*, vol. 4, p. 373, 1989.

[178] S. K. Clark and K. D. Wise, "Pressure sensitivity in anisotropically etched thin-diaphragm pressure sensors," *IEEE Trans. Electron. dev.*, vol. ED-26, no. 12, pp. 1887–1896, 1979.

[179] Y. Sato, C. Hata, T. Ando, and M. Kamo, "Growth and characterization of high quality CVD diamonds," *New Diamond Sci. and Tech. @ MRS Int. Conf. Proc.*, pp. 537–548, 1991.

[180] H. Guo and M. Alam, "Residual stress in CVD diamond films," *Proc. of the 1st Int. Conf. on the Applications of Diamond Films and Related Materials.*, vol. B.V., pp. 149–154, Auburn, Alabama Aug. 17-22 1991.

[181] H. Windischmann, G. F. Epps, Y. Cong, and R. W. Collins, "Intrinsic stress in diamond films prepared by microwave plasma CVD," *J. Appl. Phys.*, vol. 69, pp. 2231–2237, Feb. 1991.

[182] O. Dorsch, K. Holzner, M. Werner, E. Obermeier, R. E. Harper, C. Johnston, P. R. Chalker, and I. M. Buckley-Golder, "Piezoresistive effect in boron doped diamond thin films," *Diamond 92 (ICNDST-3 Diamond Films 92 Heidelberg, Germany*, pp. 20.2–20.3, Sept. 1992.

[183] M. Aslam, I. Taher, M. A. Tamor, T. J. Potter, and R. C. Elder, ""CVD" diamond piezoresistive sensors," *IEEE Proceedings, Intl. Conf. on Solid-State Sensors and Actuators (Transducers'93).*, pp. 718–721, Yokohama, Japan, June 7-10 1993.

[184] D. R. Wur, J. L. Davidson, W. P. Kang, and D. Kinser, "Fabrication and Characterization of Doped Polycrystalline Diamond Film (PDF) for Strain Sensing Applications," *IEEE Proceedings, Intl. Conf. on Solid-State Sensors and Actuators (Transducers'93).*, pp. 722–725, Yokohama, Japan, June 7-10 1993.

[185] J. Y. W. Seto, "The electrical properties of polycrystalline silicon films," *J. Appl. Phys.*, vol. 46, pp. 5247–5254, Dec. 1975.

[186] C. J. Rauch, "Millimetre cyclotron resonance in diamond," *in Proc. Inter. Conf. on Semi. Phys.*, p. 276, 1962.

[187] J. F. Nye, *Physical properties of crystals.* London: Oxford Press, 1985.

[188] Y. Kanda, "A graphical representation of the piezoresistance coefficients in silicon," *IEEE Trans. Electron. dev.*, vol. ED-29, no. 1, pp. 64–70, 1982.

[189] J. J. Wortman and R. Evans, "Young's Modulus, Shear Modulus, and Poisson's Ratio in Silicon and Germanium," *J. Appl. Phys.*, vol. 36, pp. 153–156, Jan. 1965.